DEPARTMENT OF

CIVIL AND ENVIRONMENTAL ENGINEERING

POLITECNICO DI MILANO

SCHOOL OF CIVIL, ENVIRONMENTAL, AND URBAN ENGINEERING

DEPARTMENT OF CIVIL AND ENVIRONMENTAL ENGINEERING

FINAL PROJECT

Prof. Ing. Liberato Ferrara

NUMERICAL SIMULATION OF THE FRESH STATE BEHAVIOUR OF CEMENT PASTES WITH A LAGRANGIAN FINITE ELEMENT METHOD

JUAN ERAZO 842540 juanalfaro.erazo@mail.polimi.it

Academic Year 2015 – 2016

CONTENTS

LIST OF FIGURES

LIST OF TABLES

ACKNOWLEDGEMENT

During this time in the Politecnico di Milano, well-reattributed sacrifice of time, brings an amazing satisfaction. From the academic point of view, I have improved my knowledge and the way of think about my passion, Civil Engineering, thanks to all the professors that I have learned during my studies.

To Professor Liberato Ferrara who has motivated during his lectures and brought the opportunity to study this field of research. Furthermore, during this moths, the professor had a lot of patience to guide me to write this final project.

To Dr. Massimiliano Cremonesi who has helped me to understand the implementation of the Particle Finite Element code.

The past years outside my country, I have found amazing friends as Алексей, Tatyana, Vicente and Eduardo who have supported, advised me and we have stablished a grateful friendship during our studies.

To my family: Despite of the distance, they have motivated me to achieve my personal goal in one of the most prestigious universities of Europe and the most important of Italy.

To Geovanna de Palma: It is difficult to describe everything that she did during these years at Milan, I really appreciate all the words of hope that each week I listened from her.

ABSTRACT

Describing this thesis which consist on the numerical simulation of fresh cement pastes polimers/fibres materials, such as Styrene-Butadiene Rubber (SBR) latex, Styrene-butadiene Carboxylated (XSBR) and Wollastonite. The experimental results have been developed by the laboratories of Politecnico di Milano and Laboratory LabEST, Federal University of Rio de Janeiro. The main purpose of this thesis is related to the simulation of the mentioned cement pastes where the rheological material properties such as yield stress and plastic viscosity were taken into account. The numerical simulation was focused in carrying out the mini-cone slump test in 3D and 2D, using a code based the Particle Finite Element Method which was developed by a team of the Politecnico di Milano. The comparison between numerical simulation and experimental curves are presented in this document.

1

SCOPE AND OBJECTIVES

Starting from experimental data of various cementitious materials that were developed in the laboratory (LabEST- Federal University of Rio de Janeiro), to describe a model with a Lagrangian finite element method for the interaction between flexible structured pastes and free surface fluid flows.

- To correlate a Lagrangian Finite Element Code with experimental results of fresh concrete behaviour based on Bingham parameters.

2

INTRODUCTION

Currently, different cementitious composite materials are being developed for use in civil engineering construction. Industrialization requires the development of a process which performs the elaboration of concrete structural elements. One of the most relevant operations in the process is casting. Hence, it is important to know the rheological properties and the behaviour of fresh concrete. The measurement of these properties has limitations because the equipment is expensive, is not always compatible with the field of applications, and is not accessible in every laboratory. Correlations that link rheological parameters and field test measurements have been determined: for instance, the association between the yield stress and the slump flow diameter[1]. Then, the number of analysed cases is significant, so the use of a Computational Fluid Dynamics code helps to simulate the behaviour of the cement pastes[1].

Figure 1. Getto Fondazione Torre Libeskind, Abram Cone In situ[22]. (Source: Holcim, 2015)

Every day, new technologies to be implemented in the construction market are proposed. As a consequence, the rheological properties of fresh cement paste have become relevant, as have the mechanical properties of solid concrete. Other important aspects in the production process are production challenges, placement, and manufacture, in which the rheological parameters have an important role.

The introduction of SCC (self-compacting concrete) technology in the construction market has increased attention to the knowledge of rheological properties[1]. Acceptable changes in the rheological properties achieve the adequate fresh state properties[2] as well as ensuring strength [1]. One of the most important factors during casting is the formwork design[1]. Knowledge of the rheological properties provides information on the decay pressure rate. The formwork has an important role in the construction process because it is linked with the rate of casting [1]. Rheology helps the engineer to know the load on which the formwork will be working on the contact surface, so an optimal product can be designed.

Figure 2. Getto Fondazione Torre Libeskind, Casting[22]. (Source: Holcim, 2015)

Figure 3. Getto Fondazione Torre Libeskind, Pumping concrete[22]. (Source: Holcim,2015)

Most sophisticated applications of advanced cement-based materials are in high-rise buildings, underwater pumping, and other examples. Therefore, rheology is the most relevant factor that influences the flow and placement of concrete through plug-slip and shear flow mechanisms. The flow through a pipe with pressure loss and rheological properties are correlated in the Buckingham-Reiner equation [1].

The most commonly employed model for fresh cement paste is the Bingham model which needs two rheological parameters, the yield stress τ_0 and the viscous plasticity μ, in order to represent the rheological behaviour of cement suspensions[1].

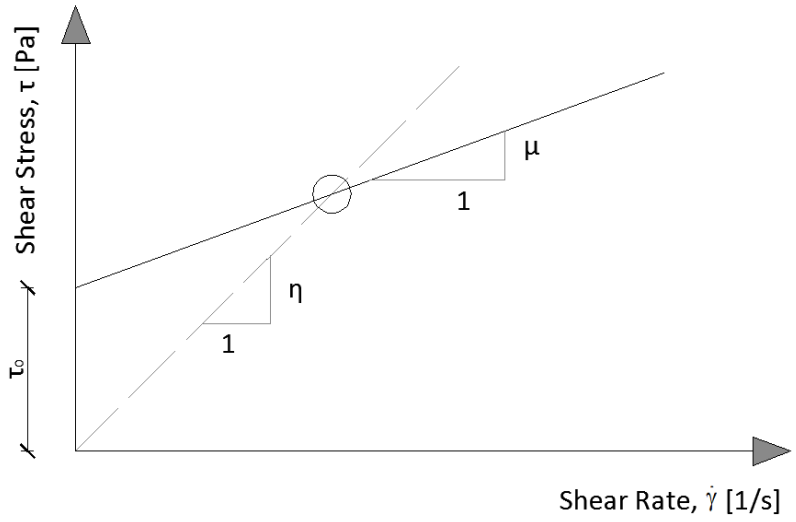

Figure 4. Bingham Rheological Model [3]. (Source: Banfill , 2000)

The Bingham mathematical model represented in the following expression[3]:

$$\eta = \mu + \frac{\tau_0}{\dot{\gamma}} \quad (1)$$

Where

η is the Viscosity of the Bingham Fluid [Pa.s]

μ is the Plastic Viscosity [Pa.s]

τ is the Yield Sher Stress [Pa]

$\dot{\gamma}$ is the Shear rate [1/s]

Then, the shear stress equation is provided by $\tau = \eta\dot{\gamma}$, where τ is the applied shear stress[3].

As consequence, the shear stress Bingham fluid equation (see equation 2) is obtained in the base of the mentioned viscosity equation as following[3]:

$$\tau = \eta\dot{\gamma} = \left(\mu + \frac{\tau_0}{\dot{\gamma}}\right)\dot{\gamma} = \mu\dot{\gamma} + \tau_0 \quad (2)$$

A wide range of commercial rheometers or custom-built rheometers has been put into practice to measure the two aforementioned properties[1]. Additionally, these instruments are able to provide information about material rheology, which includes thixotropy, temperature dependence, pressure sensitivity, rheo-magnetical measurements, and other factors. The problem arises due to the cost of the devices, which hinders their use both in precast concrete factories and at construction sites. Additionally, the varying results obtained by using different equipment are still being debated. A practical measurement method of rheological parameters, which has been widely implemented in laboratories for fresh-state concrete, is the mini-cone slump. This test provides a good correlation with the yield stress[4]. Moreover, current studies have indicated the correlation between the stop-time flow in a slump/mini-slump test and the plastic viscosity property[5]. As Roussel, Gram, and Cremonesi, described, "The value of plastic viscosity shall not pay a role on the final shape as long as it is high enough for flow inertia to stay neglectable"[6].

Figure 5. The ConTec viscometers, Version 3 and Version 4 [3]. (Source: Banfill , 2000)

The correlation between rheometer parameters obtained from rheometers and the measurements obtained from field tests has been evaluated by Computational Fluid Dynamics model[7]. This procedure ensures the validation of the results obtained in the laboratory with respect to a numerical simulation.

3

CODE BASED ON THE LAGRANGE FINITE ELEMENT METHOD

At the present time, it is important to develop a tool for computational modelling based on rheological parameters because it helps to enhance mix compositions and processing techniques for civil engineering applications. Additionally, high-performance concrete in its fresh state can take advantage of these properties, in order to optimize the design procedures during casting [8].

Concrete and mortars in their fresh states are composite materials because their mixture consists of a fluid matrix and solid particles that are in suspension[9]. Different solution strategies are implemented according to the selected hypothesis. For example, the suspension particles are considered independent or homogeneous with respect to the matrix base. In this case, due to the size of aggregates, the matrix and the particles are considered homogeneous non-Newtonian fluid. Then the fluid composite follows a non-linear constitutive law[10]. Hence, the mathematical formulation of Bingham viscous-plastic models, which are described in this chapter, fit the purpose and they provide accurate results despite of the complex phenomena[10].

Additionally, the main goal of the analysis is to simulate cementitious composites, which experience large displacements on free surfaces. In fact, the scientific community pays attention to the flow of experimental non-Newtonian fluids and numerical models in civil engineering applications[10].

As a matter of fact, analytical approaches are applied under specific circumstances only[10], so experiments on flow of thixotropic fluids are validated against theoretical results[10]. Numerical simulations must be used for this and other engineering applications. The issues of flow cessation are able to be solved as Couette or Poiseuille flow for one-dimensional cases and Bingham fluid for 2D or 3D flows. For the latter flows, the model is able to follow free surfaces that experience large displacments[10].

Using the Eulerian approach to simulate free surfaces results into a well-suited problem because material flows through a fixed mesh. Another option is the use of the Fluid Volume[11] algorithm, but its implementation is complicated. Other options for simulating non-Newtonian Fluid Flow are FEMLIP (finite element method with Lagrangian Integration points)[12] or the Lattice-Boltzmann method[13]. They can be

considered as two important families of techniques, Arbitrary Lagrangian-Eulerian (ALE) approaches and fully Lagrangian approaches[10].

ALE approaches, are accurate for large deformations and large strain problems. The general idea of this method consists of the decoupling of the mesh motion from "the material domain in such a way that it allows to smooth a distorted mesh"[10], so a complete remeshing is not needed. The ALE method has been implemented in commercial codes for solving issues related to large strain deformation in a material. On the other hand, this method has limitations in "geometries where the material flow is relatively predictable and where the surface movement is rather limited".[10]

The fully Lagrangian approaches consider that the motion of material particles is tracked, and that the free surface configuration is kept while its movement is not restricted. A non-beneficial consideration of these approaches is the severe distortion of the mesh, so they require more computational cost due to remeshing that could be required[10].

It is worth describing the Meshless Lagrangian approaches, which avoid the mesh of the domain. Smoothed Particle Hydro-dynamics (SPH)[8] can be implemented to simulate Bingham-like fluid. This has been validated with analytical benchmarks. Nevertheless, these techniques are established in the strong form of equilibrium, so these approaches are still controversial[10].

As a consequence, the latest improvements in the family of Lagrangian FEM and robust meshing algorithms are considered. With previous contributions of investigations, fully Lagrangian approaches were taken with surface tracking ability to analyse incompressible non-Newtonian fluid flows, and these contributions were established on continuous re-triangulation of the domain. This principle is called the Particle Finite Element Method (PFEM)[14]. This method is widely used to solve civil engineering problems related to free-surfaces flows, breaking waves[14], fluid-structure interactions[15], and fluid-object interactions[16]. These problems have then been correlated with experimental results in order to be validated[10].

Before describing the implementation of the mini-slump-flow model, it is worth describing one particular technique for remeshing[10]. This technique is detailed in the Particle Finite Element Method topic.

3.1 Governing Formulation

The problem is established based on the principle that the material properties are function of time, so the initial configuration of the non-Newtonian fluid is defined as Ω_0. Next, the present configuration of the non-Newtonian fluid is defined as Ω_t whose domain is at time $t \in [0, T]$. The initial location of the material is denoted as x_0 at time $t - t_0$. Hence, the current point is denoted by $\mathbf{x} = \chi(\mathbf{x}_0, t)$, where χ depicts the fluid transformation. Moreover, with Cauchy stress tensor $\boldsymbol{\sigma} - \boldsymbol{\sigma}(\boldsymbol{x}, t)$ and velocity $\boldsymbol{u} - \boldsymbol{u}(\boldsymbol{x}, t)$, the momentum and mass conservation governs the motion of a homogeneous incompressible fluid filling the domain Ω_t[10].

$$\rho \frac{D\mathbf{u}}{Dt} = div\boldsymbol{\sigma} + \rho\mathbf{b} \quad \text{in } \Omega_t \text{ x (0, T)} \tag{3}$$

$$div\mathbf{u} = 0 \quad \text{in } \Omega_t \text{ x (0, T)} \tag{4}$$

Where:

ρ(**x**) represents the fluid density,

b(**x,t**) is the external body forces,

$\frac{D}{Dt}$ is the material time derivative,

div is the divergence operator computed with respect to the actual configuration[10].

The equations (1) and (2) are computed with the initial conditions[10]:

$$\mathbf{u}(x, t = 0) = \mathbf{u}_0 \tag{5}$$

Then, the suitable boundary conditions $\Gamma t = \partial\Omega_t$ are considered as the summation between two non-overlapping subsets Γ_D and Γ_N, such that $\Gamma_D \cup \Gamma_N = \Gamma_t$ and $\Gamma_D \cap \Gamma_N = \emptyset$ are the correspondent Dirichlet and Neumann boundary conditions enforced on Γ_D and Γ_N, respectively[10];

$$\mathbf{u}(x, t) = \bar{\mathbf{u}}(x, t) \quad \text{on} \quad \Gamma_D \text{ x (0,T)} \tag{6}$$

$$\sigma(x, t)\mathbf{n} = \mathbf{h}(x, t) \quad \text{on} \quad \Gamma_N \text{ x (0,T)} \tag{7}$$

where $\bar{\mathbf{u}}(x, t)$ and $\mathbf{h}(x, t)$ are given information and **n** is the unit outward normal to the boundary Γ_t. Then, the Cauchy stress tensor can be decomposed into isotropic and deviatoric parts as usual[10].

$$\boldsymbol{\sigma} = -p\mathbf{I} + \tau \tag{8}$$

Moreover, the fluid is considered incompressible, isotropic, and following Bingham Constitutive law[10]:

$$\tau = 2\mu \in (\mathbf{u}) + \tau_0 \frac{\in (\mathbf{u})}{\| \in (\mathbf{u}) \|} \quad \text{if} \quad \| \in (\mathbf{u}) \| \neq 0 \tag{9}$$

$$\|\tau\| \le \tau_0 \quad \text{if} \quad \left\| \in (\mathbf{u}) \right\| = 0 \tag{10}$$[10]

Which can be expressed as

$$\in (\mathbf{u}) = \left(1 - \frac{\tau_0}{\|\tau\|}\right)\frac{\tau}{2\mu} \quad \text{if} \quad \|\tau\| = \tau_0 \text{ otherwise} \tag{11}$$

$$\in (\mathbf{u}) = 0 \quad \text{otherwise} \tag{12}$$

where $\in (\mathbf{u}) = 1/2(grad\boldsymbol{u} + grad\boldsymbol{u}^T)$ is the symmetric part of the velocity and $\|.\|$ is the Euclidean norm[10]:

$$\|\in (\mathbf{u})\| = \sqrt{\frac{1}{2} \in : \in} \|\tau\| = \sqrt{\frac{1}{2}\tau : \tau} \tag{13}$$

Then the constitutive law of the equation (7) is reduced to 1D as follows[10]:

$$\tau_{xy} = \mu \frac{\partial u_x}{\partial y} + \tau_0 sign\left(\frac{\partial u_x}{\partial y}\right)$$

This equation describes a flow in direction X between two infinite plates separated by a gap along the y axis. Numerical complications arise because Bingham constitutive law features as "rigid elastic" behaviour, so an "approximation based on smoothing in the equations (7) and (8) is preferred"[10].

As Cremonesi, Ferrara, Frangi, and Perego state, "In the so-called biviscosity model, the 'rigid' branch of the ideal behaviour is approximated with a very high, but bounded viscosity"[10]. This bilinear approximation can produce inconsistent predictions, so Papanastasiou´s law is considered, which is based on exponential increase of the viscosity[10].

$$\tau = \mu \in (\mathbf{u}) = \left[2\mu + \frac{\tau_0}{\|\in\|}\left(1 - e^{-m\|\in\|}\right)\right] \in (\mathbf{u}) \forall \|\tau\| \tag{14}$$

Hence, the apparent viscosity $\tilde{\mu}$ is introduced. Additionally, in the limit case of $m \to \infty$, the choice is a compensation between numerical problems and the mechanical response accuracy because the Bingham behaviour is recovered[10].

It is important to note that, even though the Bingham model is the simplest law which includes the concept of yield limit, alternative options have been presented: for instance, the Herchel-Bulkley law[10]:

$$\tau = \left(2\mu \|\in (\mathbf{u})\|^{q-1} + \frac{\tau_0}{\|\in (\mathbf{u})\|}\right) \in (\mathbf{u}) \text{ if } \|\tau\| > \tau_0 \tag{15}$$

$$\in (\mathbf{u}) = 0 \text{ if } \|\tau\| < \tau_0 \tag{16}$$

where q is a non-physical parameter. Due to the fact that there is no significant difference between these models, the formulation of the code considered the smooth Bingham law (12)[10].

3.2 Numerical Formulation

3.2.1 Space and time discretization

According to Cremonesi, Frangi, and Perego[7], the mass conservation and the momentum of the previously-cited equations (1) and (2) are written based on a fixed reference configuration[10]:

$$\rho \frac{D\mathbf{u}}{Dt} = Div\Pi + \rho_0 \mathbf{b} \quad \text{in} \quad \Omega_0 \text{ x } (0, T) \tag{17}$$

$$div(J\mathbf{F}^{-1}\mathbf{u}) = 0 \quad \text{in} \quad \Omega_0 \text{ x } (0, T) \tag{18}$$

Where

u is the material-point-velocity in $\mathbf{x}_0$ at time t=0

ρ_0 is the initial density

$\mathbf{\Pi}=J\boldsymbol{\sigma}\mathbf{F}^{-T}$ is the first Piola-Kirchhoff stress tensor

F is the deformation gradient

J is the determinant of **F**

Div is the divergence operator computed with respect to the initial coordinates $\mathbf{x}_0$.

The Galerkin isoparametric finite element discretization is introduced with the assumption that at time $t=t^n$ the state of the system is known in terms of particle position $\mathbf{X}^n=\mathbf{X}(t^n)$, velocities $\mathbf{U}^n=\mathbf{U}(t^n)$ and pressures $\mathbf{P}^n$. Then, the state at time $t=t^{n+1}$ is computed by enforcing the equations (15) and (16) at time in the essence of a backward Euler integration. Consequently, the problem can be written as fully discretized as following:

$$\mathbf{M}\frac{\mathbf{U}^{n+1}-\mathbf{U}^n}{\Delta t} + \mathbf{K}(\mathbf{X}^{n+1})\mathbf{U}^{n+1} + \mathbf{D}^T(\mathbf{X}^{n+1})\mathbf{P}^{n+1} = \mathbf{B}^{n+1} \tag{19}$$

$$\mathbf{D}(\mathbf{X}^{n+1})\mathbf{U}^{n+1} = 0 \tag{20}$$

Where

M is the mass matrix

K is the fluid stiffness matrix

D is the discretization of the divergence operator

B is the vector of external forces

3.2.2 Particle Finite Element Method

The equations (19) and (20) form a non-linear equation system that depends on the main unknown vector U^{n+1}. Some methods can be implemented in order to solve the system, such as the Newton-Raphson approach or the Picard technique. The latter is simpler and has a good convergence speed[7].

Mesh distortion is treated in the essence of the Particle Finite Element Method (PFEM), which has been tested and effective results have been obtained in the solving of fluid dynamic problems, which include free-surface flows and breaking waves[14].

Any time at which the quality of the mesh does not satisfy the element-distortion criteria, the connectivity of existing nodes is recalculated using a Delaunay triangulation[10]. Hence, this technique has some important effects.

The nodes are the only topological objects that maintain function during the time solution. Thus, in order to avoid data interpolation from the previous mesh to the new one, linear shape functions are implemented in the velocity and pressure unknowns[10]. Even so, this fully linear problem system does not fulfil the inf-sup conditions because oscillations[17] may occur in the pressure. A stabilizing technique called the Petrov-Galerkin (PSPG)[18-20] technique provides accurate results in the context of Lagrangian approaches[10].

It is helpful to note that external boundaries are taken into account when they are placed in the fictitious node whose movement is not permitted[10]. Then, the Delaunay triangulation provides the convex figure of minimum area that encloses all the points that may be not satisfy the external boundaries[10]. A potential way to figure out this problem is the α-shape method proposed by Oñate, Idelsohn, Del Pin, and Aubry[14]. The main idea consists of removing the unnecessary triangles from the mesh with a criterion based on mesh distortion. In the mesh, for each triangle *e*, the minimum distance h_e between two nodes inside the element and the radius R_e circumcircle of the element is determined. The computation of *h* is the mean value of all the h_e values, so the shape factor is computed as[10]:

$$\alpha_e = \frac{\mathrm{R_e}}{h} \geq \frac{1}{\sqrt{3}} \tag{21}$$

This is considered a distortion-element index. The condition is that the triangles which do not fulfil the following condition are discarded from the mesh, where $\bar{\alpha} \geq 1$ is considered[10].

$$\alpha_e \leq \bar{\alpha} \tag{22}$$

In order to reduce the computation cost, the mesh is regenerated only when it is globally too distorted. Based on Eq. (19), for each element a distortion factor β_e is calculated as a mesh-quality measure[10].

$$\beta_\varepsilon = \sqrt{3}\alpha_e = \sqrt{3}\frac{\mathrm{R_e}}{h_e} \geq 1 \tag{23}$$

Considering the equilateral triangle ($\alpha_e = 1/\sqrt{3}$) as the best possible element, the quality of the entire mesh is evaluated by an arithmetic mean[10]:

$$\beta = \frac{1}{N_{el}} \sum_{e=1}^{N_{el}} \beta_e \tag{24}$$

Where N_{el} is the number of elements. If $\beta > \bar{\beta}$ only the mesh is regenerated, where $\bar{\beta} > 1$ is a fixed parameter. As distortion becomes larger, the value that is accepted also becomes larger. A flowchart summarizes these steps.

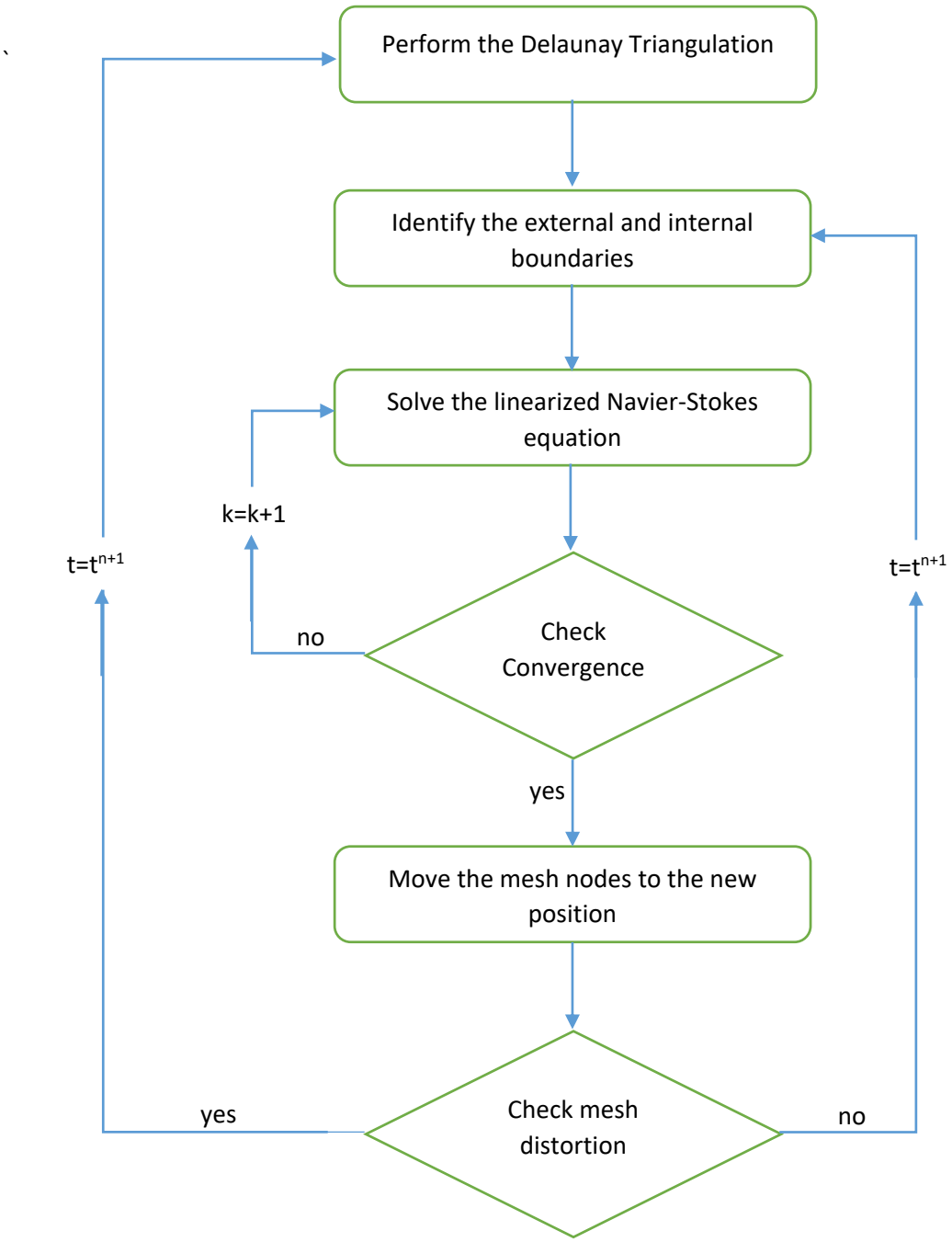

Figure 6. Flowchart of the solution scheme with checking for mesh distortion[10]. (Source: Cremonesi, 2010)

3.2.3 Adding and removing particles.

In the case of highly-viscous flows in the Lagrangian approach where particles move due to fluid flow, the distribution of particles is probably too irregular[10]. To solve this problem, substituting and adding particles is performed on the basis of two main criteria. The first is related to addressing excessive concentration and the second is rarefaction[10].

The previous checks are done if the particles are too adjacent to one another, so a circle centred on the node is created in each node of the mesh[10]. The radius of the circle γ depends on the average dimension of the mesh elements. When other nodes are inside the circle, the centre node is removed from the mesh[10]. As the value of the radius becomes smaller, the quantity of particles removed from the mesh is also lower. The parameter γ can be defined according to the average area of the elements A_m[10].

$$\gamma = \bar{\gamma}\sqrt{\frac{4A_m}{\sqrt{3}}} \tag{25}$$

Where $0 < \bar{\gamma} < 1$, when $\bar{\gamma} = 1$. The previous equation represents the average distance between two nodes in an equilateral triangle.

This criterion helps to test if a region´s nodes are too insubstantial. Each area element of the mesh is contrasted with a reference value ω[10]. This provides information about the size of the area-element. If the area-element is bigger than ω, a particle is added in the centre of the triangle. Then, the velocity at the previous time step is defined[10]. The node-velocity in the element is calculated using a linear interpolation of the velocity of the nodes where the new node is established. Starting with the average area-element A_m, the parameter is defined as[10]:

$$\omega = \bar{\omega}A_m \tag{26}$$

Where $\bar{\omega}\epsilon\mathbb{R}^+$ and $\bar{\omega} > 1$. As the value of $\bar{\omega}$ becomes greater, larger triangles are considered[10].

4

APPLICATION TO THE FLOW OF CEMENT PASTES

4.1 Introduction

The basic rheological parameters of fresh state concrete are important in the application of quality control, casting in place, and design of the cementitious mixture.

So far, the most appropriate rheometer has been under discussion. In order to obtain an appropriate correlation of the measurements, a simple test has been considered. The numerical code, developed by the Politecnico di Milano, is based on the previous theoretical background. The main purpose of the code is to validate the experimental data of the fresh state performance paste and concrete through Lagrangian Finite Element approach.

Once the basic parameters are known, the first step of this document is to reproduce the experimental procedure with the aid of a code based on the Lagrangian finite element method. In the following paragraphs, a description of the test and the assumptions are listed. The yield stress has been obtained from the slump/mini-slump-flow diameter[4] and the viscosity was obtained from the Haake Mars III rheometer[26].

4.2 Materials and Mix Design of Pastes

The relevant materials present in the cement paste design are the SBR (Styrene Butadiene Rubber), XSBR (Carboxylated Styrene Butadiene Rubber) and the Wallastonite which provides the main characteristics of each cement pastes.

SBR Latex comes from two monomers, Styrene and Butadiene and is part of the synthetic rubbers. It means that this material provides an increment in tensile strength and fracture toughness. Furthermore,

in civil engineering application is used for enhance the waterproofness, chemical resistance and freeze-thaw durability. Hence, this material reduces shrinkage and improve the flexibility[23].

Carboxylated Styrene-butadiene is an elastomeric that is used to increase the weather resistance, adhesion properties, and less permeable to gases and solvent molecules. This component is employed in oil well cementing[25].

Then, the Wallastonite is a mineral which formula is Calcium Silicate. In the industrial field has many applications and also in civil engineering where the mechanical properties of concrete have been enhanced, such as the compressive and flexural strength. Hence, the water absorption and drying shrinkage are reduced. Moreover, the improvement of alternate freezing-thawing and sulphate attack. [24]

This information was provided by the Laboratory LabEst, Federal University of Rio de Janeiro. The material properties of the cement pastes have the following mix design, according to the table 1.

Materials	P0	P2.5S	P4.4S	P5.9S	P2.5X	P4.4X	P5.9X	WO5/WN5	WO7.5/ WN7.5	WO10/ WN10
Cement (%m)	50.00	48.23	46.99	46.03	48.23	46.99	46.03	46.07	44.19	42.36
Silica Fume (%m)	16.10	15.51	15.11	14.80	15.51	15.11	14.80	14.81	14.21	13.62
Water (%m)	31.76	29.51	27.95	26.74	30.95	30.39	29.96	29.26	28.06	26.90
Superplascizer (%m)	2.15	2.07	2.02	1.98	2.07	2.02	1.98	1.98	1.90	1.82
SBR Latex (%m)		4.68	7.94	10.45	3.27	5.54	7.30			
Wallastonite (%m)								7.88	11.65	15.30

Table 1. Mix Design Cement Pastes[26]. (Source: Laboratory LabEST, Federal University of Rio de Janeiro, Rio de Janeiro-Brazil)

It could be notice in the table 1 that the initial cement paste is P0 whose mass fraction of Portland cement is 50% and the other materials as Silica Fume, water and superplasticizer based in Naphthalene. The last one was implemented in order to obtain an appropriate fluidity and it is composed of 40% of solid particles and liquid of 60%. Hence, the water that belongs to the superplasticizer was considered in the amount of total water added in the mix design whose water/cement ratio is 0.66[26].

The weight as polymer particles present in latex form are 34.5% for SBR and 49.4% for XSBR. In base of the reference paste P0, the Portland cement and silica fume were replaced in fractions of 2.53, 4.41 and 5.93% which were related to the polymer mass content in latex. Then, it is the reason of their name of the pastes. In the case of SBR modified pastes are P2.53S, P4.41S, P5.93S and for XSBR modified pastes P2.53X, P4.41X and P5.93X. It is worth to describe that the cement/water ratio of the liquid phase of the superplasticizer was consider for the total water content in order to maintain the water/cement ratio in 0.66[26].

Mixing Procedure of the Paste

In this phase, the procedure that the materials were mixed is described as following. The cement and in the case of some pastes the wallastonite, were weighted in a bowl and mixed until the components were homogeneous. In another bowl, the Silica fume was weighted. Then, each liquid material as water, superplasticizer and latex were weighted in a different bowl[26].

Once the percentage of each material were weight, the next step is to mix the water and silica fume until they were a uniform paste. In order to achieve it, two speed-bowl mixer was used. The homogenization process consisted in employment of a routine of different speed and time that the materials were homogenized. The first phase, the silica fume and the water were mixed for two minutes with a low speed which means 96 revolutions per minute (rpm). Later, during 20 minutes the maximum speed of the equipment was set that is 180 rpm. Rarely, the mixer was stopped less than 2 minutes in order to remove the material from the borders of the bowl. Then, the other materials such as, cement and wollastonite if there was the case, superplasticizer and/or polymers were spread in intervals lower than five minutes, while the mixer was working at low speed. After all materials were added in the mixture, the speed-bowl mixer at high speed homogenize the cement past for 30 minutes more. The following figure, describe the rpm set in the machine vs the time that was subjected to mix the materials[26].

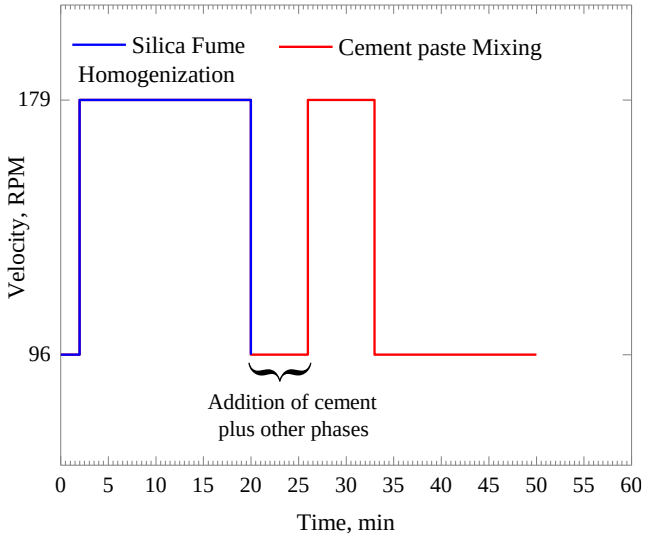

Figure 7. Mixing Process[26]. (Source: Laboratory LabEST, Federal University of Rio de Janeiro, Rio de Janeiro-Brazil)

4.3 Mini-Cone Slump Flow Test.

The slump-flow test is based on a standard test that is used to obtain the rheological properties of concrete. It consists of a conical mold with fixed dimensions with openings at the top and bottom. The concrete is placed without tamping or vibration. The mold is raised, and the concrete is allowed to

spread[21]. Physically, the fresh material flows due to the yield stress overcoming the yield strength of the material, until it arrives at equilibrium and the flow stops. The measured parameter is the diameter of the flow; that is, the average between two orthogonal measurements. The slump-flow diameter is correlated with the yield stress of the fluid cementitious material[10]. The mini-cone slump has standard measurements that were established in the numerical simulation (see Figure 8). The particular variation from the test that was developed in the laboratory is that the cone was inverted from the usual position, which means the smaller diameter in the bottom. During this procedure, a video recorder with 1080 pixel/30fps resolution was set at 500mm above the cone in order to measure the radius. Each record lasted 90 seconds. This technique had implemented in order to obtain a radius vs time evolution curves was obtained[26].

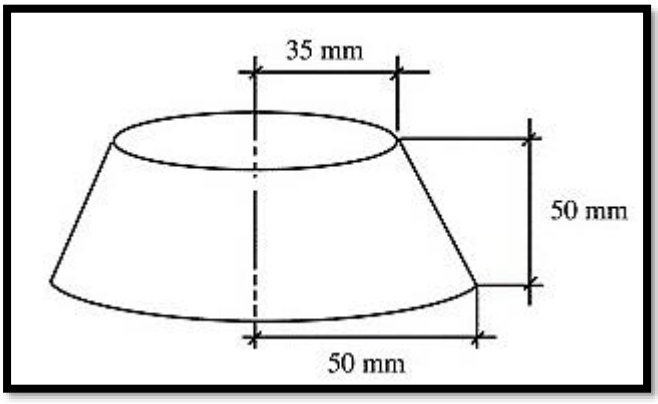

Figure 8. Mini-Cone Slump Flow Test measurements[21]. (Source: Roussel N., 2004)

4.4 Rheometer Tests.

The change of viscosity happens over a period of time; it is considered as time-dependent. In practice, there is not important to distinguish if the phenomenon is reversible and irreversible because the viscosity increases when the paste does not flow over time. Wide number of methods have been proposed in the research field in order to measure thixotropy of cement pastes. According to Ferron, the thixotropy depends on the degree of material structural build-up or breakdown[27]. In order to obtain the hysteresis loop and look for the behavior of polymer-modified cement pastes, a Haake Mars III rheometer was implemented. After the mini-cone slump test had performed, the same cement paste was used in the rheometer test. Then, the cement paste is poured into the rheometer cup until it covered the vane, (see figure 9), until the vane is covered by the cement paste. This procedure guarantees the measure of the rheological properties from the same material[26]. After that, a shear rate of 0.1 s^{-1} was applied for 60 seconds at the first time in order to ensure the same shear history for all cement pastes described in the table 1. Then, the shear rate is increased according to this set of rates: 0.1 s^{-1}, 0.3 s^{-1}, 0.6 s^{-1}, 3 s^{-1}, 6 s^{-1}, 10 s^{-1}, 20 s^{-1}, and 30 s^{-1}. Next, the shear rate is decreased with the same set of rates. This increment and

decrement of rates lasted 150 seconds. This procedure, was performed four times more, which means after, 10s, 60s, 300s, and 600s. Hence, five hysteresis curves were obtained[26].

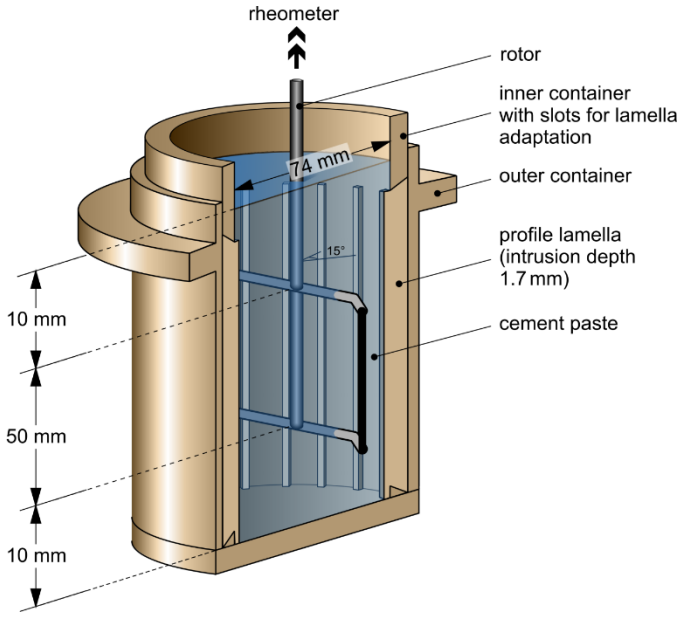

Figure 9. Scheme of the Rheometer cup with the vane implemented in the Laboratory[26]. (Source: Laboratory LabEST, Federal University of Rio de Janeiro, Rio de Janeiro-Brazil)

In order to define the rheological parameter, the Herschel-Bulkley (27) model was set up[26].

$$\tau_{\mathbf{f}} = \tau_0 + \kappa\left(\dot{\gamma}\right)^n \tag{27}$$

τ0 is the yield stress

k is the consistency index

$\dot{\gamma}$ is the shear rate

n is the index behaviour

A mathematical computation is required to get the plastic viscosity (μ_0) [26]

$$\mu_0 = \frac{3k}{n+2}\dot{\gamma}_{\max}^{\mathbf{n-1}} \tag{28}$$

The computation of thixotropy of the pastes is developed using Ferron proposal[26]. Adaptation were developed because the equilibrium loop was not developed in order to obtain the equilibrium line in the shear stress vs shear rate figure. To figured out this problem, the lower range of the first hysteresis loop (0s) was consider as a reference equilibrium line. The break down structure energy build-ups after resting time was computed considering the areas between the reference equilibrium line and ascending branch of the hysteresis loop. Singular points in the low shear rate region were avoided, and the arising error was

decrease, when only the interval between 6 s^{-1} to 20 s^{-1} was considered in the computation of the thixotropic energy (see figure 10) [26].

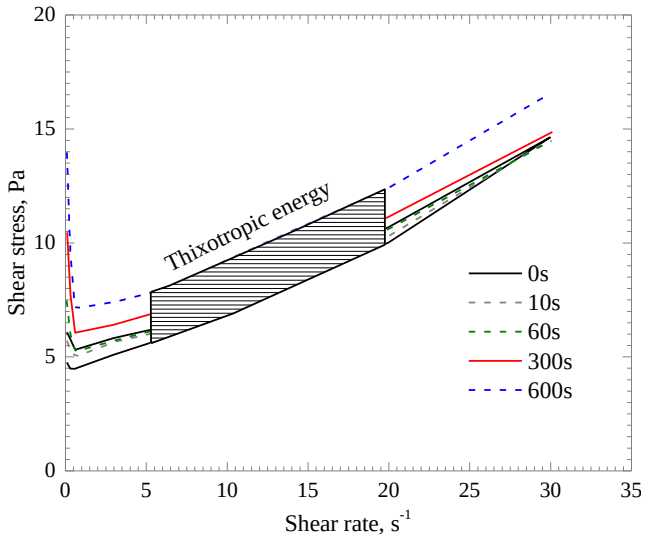

Figure 10. Considered area for thixotropic energy calculations[26]. (Source: Laboratory LabEST, Federal University of Rio de Janeiro, Rio de Janeiro-Brazil)

4.5 Data of Cementitious Pastes

This document is based on the information provided by laboratory testing. The fundamental parameters, such as shear stress, viscosity, and density, from thirteen different types of cement pastes were provided. The simulated cementitious pastes were the following: P0, P2.5S, P4.4S, P5.9S, P2.5X, P4.4X, P5.9X, WO5, WO7.5, WO10, WN5, WN7.5, and WN10. In the cases of WO5, WO7.5, WO10, WN5, WN7.5, and WN10, the value of the density was assumed as 2.0dm^3 due to the fact that this information was not provided. A refined analysis is presented in Figure 29 (page 39). The variation of this parameter does not vary the result at all compared with the variation from the shear stress and viscosity of the cementitious pastes. A summary of this information is prescribed in Tables 1 through 3.

The fundamental measurement parameter, which was used to correlate the results of the experimental and numerical models, is the measurement of the diameter as a function of time. It is worth presenting the measurement of the radius instead of the diameter because the provided data was a function of the radius. Moreover, the 2D model gives information about the radius. The information discussed is presented in the annex of this document.

The substances that contain cementitious paste are described in the table 1. Hence, only the previously-mentioned fundamental parameters were taken into account for the numerical model.

The Type A information and the Type B data was provided. The tables 1, 2 and 3 provide five experimental rest-time rheological properties for 0s, 10s, 60s, 300s and 600s; at the same time, it shows two types of experimental data A and B.

		Cementitious Pastes		**P0**	**P2.5S**	**P4.4S**	**P5.9S**	**P2.5X**
	Type	**Density**	**[g/cm^3]**	1.7500	1.7100	1.6800	1.6425	1.6950
0 s	**A**	**Yield Stress (τ_{0de})**	[Pa]	2.2794	4.0418	56.7000	46.1000	2.0932
		Viscosity (μ_{0des})	[mPa.s]	15.5260	39.8365	32.8518	62.6570	82.2938
	B	**Yield Stress (τ_{0de})**	[Pa]	2.6871	12.5000	52.2000	92.1000	3.6076
		Viscosity (μ_{0des})	[mPa.s]	13.6079	81.5409	148.8770	159.7742	237.7174
10 s	**A**	**Yield Stress (τ_{0de})**	[Pa]	2.2048	4.0517	56.0000	53.1000	1.8229
		Viscosity (μ_{0des})	[mPa.s]	16.2330	41.5758	54.0930	55.7326	81.3703
	B	**Yield Stress (τ_{0de})**	[Pa]	2.6761	13.4000	53.7000	98.2000	5.8475
		Viscosity (μ_{0des})	[mPa.s]	138.7163	74.0360	122.0066	160.7407	202.3250
60 s	**A**	**Yield Stress (τ_{0de})**	[Pa]	2.1383	4.1131	54.9000	47.5000	1.7903
		Viscosity (μ_{0des})	[mPa.s]	16.5321	46.1713	63.0440	65.7486	82.6982
	B	**Yield Stress (τ_{0de})**	[Pa]	3.2796	12.7000	56.2000	104.2000	5.0659
		Viscosity (μ_{0des})	[mPa.s]	131.8548	89.3001	141.3150	159.1870	207.8906
300 s	**A**	**Yield Stress (τ_{0de})**	[Pa]	2.7526	5.0210	58.5000	52.7000	2.0432
		Viscosity (μ_{0des})	[mPa.s]	14.6437	38.9169	70.7622	91.3906	79.1328
	B	**Yield Stress (τ_{0de})**	[Pa]	3.1430	14.3000	60.0000	115.4000	3.2664
		Viscosity (μ_{0des})	[mPa.s]	140.6548	91.8065	153.4899	153.2690	237.0583
600 s	**A**	**Yield Stress (τ_{0de})**	[Pa]	2.1708	6.1699	65.3000	64.1000	2.3608
		Viscosity (μ_{0des})	[mPa.s]	18.9071	43.8605	58.7116	55.0917	78.0679
	B	**Yield Stress (τ_{0de})**	[Pa]	4.4222	16.8000	70.2000	138.1000	5.6508
		Viscosity (μ_{0des})	[mPa.s]	140.9091	94.0070	165.0868	141.3077	215.9764

Table 2. Experimental Rheological Parameters. (Source: Laboratory LabEST, Federal University of Rio de Janeiro, Rio de Janeiro-Brazil)

		Cementitious Pastes		P4.4X	P5.9X	WO5	WO7.5	WO10
	Type	Density	[g/cm^3]	1.6633	1.6350	2.0000	2.0000	2.0000
0 s	A	Yield Stress (τ_{0de})	[Pa]	2.9882	2.6990	19.7000	5.3112	24.4000
		Viscosity (μ_{0des})	[mPa.s]	243.6591	292.3454	134.1394	264.7648	258.1350
	B	Yield Stress (τ_{0de})	[Pa]	9.6565	16.1000	15.7000	16.1000	46.9000
		Viscosity (μ_{0des})	[mPa.s]	1063.0742	4191.5577	281.2545	354.8092	497.2433
10 s	A	Yield Stress (τ_{0de})	[Pa]	3.3837	2.3776	10.5000	5.3983	25.3000
		Viscosity (μ_{0des})	[mPa.s]	217.2593	271.9523	156.9456	263.2387	254.7735
	B	Yield Stress (τ_{0de})	[Pa]	9.7846	17.6000	16.4000	17.5000	48.5000
		Viscosity (μ_{0des})	[mPa.s]	1035.5716	3818.0141	287.6152	330.0423	501.8807
60 s	A	Yield Stress (τ_{0de})	[Pa]	3.3142	2.0751	12.2000	5.9277	27.4000
		Viscosity (μ_{0des})	[mPa.s]	210.7307	286.6128	151.7439	257.2182	252.5886
	B	Yield Stress (τ_{0de})	[Pa]	9.0912	23.3000	17.7000	17.4000	50.0000
		Viscosity (μ_{0des})	[mPa.s]	1057.5202	2988.1864	268.8600	340.8226	505.1871
300 s	A	Yield Stress (τ_{0de})	[Pa]	3.4281	3.1533	16.1000	7.5696	33.2000
		Viscosity (μ_{0des})	[mPa.s]	219.5707	228.1393	135.4674	251.8754	237.6368
	B	Yield Stress (τ_{0de})	[Pa]	10.9000	23.9000	19.4000	19.6000	54.8000
		Viscosity (μ_{0des})	[mPa.s]	928.8831	3400.3674	312.4510	349.0077	520.7643
600 s	A	Yield Stress (τ_{0de})	[Pa]	4.6404	3.2283	24.3000	11.9000	45.5000
		Viscosity (μ_{0des})	[mPa.s]	195.7630	220.6722	118.5600	249.0532	236.6258
	B	Yield Stress (τ_{0de})	[Pa]	12.7000	30.7000	23.8000	22.6000	63.1000
		Viscosity (μ_{0des})	[mPa.s]	895.0871	3564.3190	311.1173	358.0263	548.3386

Table 3. Experimental Rheological Parameters. (Source: Laboratory LabEST, Federal University of Rio de Janeiro, Rio de Janeiro-Brazil)

		Cementitious Pastes		WN5	WN7.5	WN10	WN10*
	Type	Density	[g/cm^3]	2.0000	2.0000	2.0000	2.0000
0 s	A	Yield Stress (τ_{0de})	[Pa]	16.2000	33.6000	135.5000	80.8000
		Viscosity (μ_{0des})	[mPa.s]	184.7478	236.6999	316.7646	444.1309
	B	Yield Stress (τ_{0de})	[Pa]	16.1000	27.6000	88.9000	
		Viscosity (μ_{0des})	[mPa.s]	305.3824	320.3551	473.5064	
10 s	A	Yield Stress (τ_{0de})	[Pa]	17.7000	34.4000	128.4000	79.4000
		Viscosity (μ_{0des})	[mPa.s]	163.1065	253.0665	370.2741	464.8038
	B	Yield Stress (τ_{0de})	[Pa]	23.3000	28.5000	88.7000	
		Viscosity (μ_{0des})	[mPa.s]	307.5937	319.8535	482.7491	
60 s	A	Yield Stress (τ_{0de})	[Pa]	19.7000	37.1000	128.3000	81.5000
		Viscosity (μ_{0des})	[mPa.s]	162.8505	242.9251	375.9547	449.4547
	B	Yield Stress (τ_{0de})	[Pa]	18.2000	29.9000	91.9000	
		Viscosity (μ_{0des})	[mPa.s]	305.6857	324.3618	485.7913	
300 s	A	Yield Stress (τ_{0de})	[Pa]	25.4000	44.1000	138.0000	90.9000
		Viscosity (μ_{0des})	[mPa.s]	155.4822	242.5367	363.4431	438.3816
	B	Yield Stress (τ_{0de})	[Pa]	19.7000	33.3000	97.3000	
		Viscosity (μ_{0des})	[mPa.s]	302.9620	335.1477	541.6295	
600 s	A	Yield Stress (τ_{0de})	[Pa]	36.3000	57.4000	157.0000	109.3000
		Viscosity (μ_{0des})	[mPa.s]	149.1821	238.9826	361.7009	460.3774
	B	Yield Stress (τ_{0de})	[Pa]	23.5000	39.7000	106.2000	
		Viscosity (μ_{0des})	[mPa.s]	327.2747	346.8311	616.0262	

Table 4. Experimental Rheological Parameters. (Source: Laboratory LabEST, Federal University of Rio de Janeiro, Rio de Janeiro-Brazil)

4.6 Slump-flow Numerical Model

The numerical models for 3D and 2D analyses were developed by Dr. Massimiliano Cremonesi, Politecnico di Milano. The sample in the 3D model was discretized in 9000, 20000, and 34000 finite elements. The sample has the standard dimensions of the mini-cone slump flow test (Figure 8). The input of the code consists of the rheological parameters, such as yield stress and viscosity, and the physical property is the density. Due to the fact that it is a problem that operates as a function of time, the input points in the code are the initial time, final time, delta time, and frequency. The delta time is the discretization of the total time analysis. The frequency is the interval during which the code creates a report of the analysis. The following arithmetical considerations were applied in order to obtain data from the numerical code.

The number of time steps that the numerical code uses to solve the problem is:

$$N = \frac{t_f - t_i}{\Delta t} \tag{29}$$

Where:

N is the number of time steps

t_i is the initial time

t_f is the final time

Δt is delta time

The initial time was always at the beginning of the test, and the final time was established in 40 seconds due to the fact that in most cases of experimental data of cementitious pastes, the curves become constant after this time. Different delta time was established in order to create a balance between accurate results and time-consuming computation.

The number of files (reports) that are expected is obtained as following:

$$Or = \frac{N}{fq} \tag{30}$$

Where:

Or is the number of files when the code provides a report

N is the number of time steps

fq is the frequency at which the program computes an output

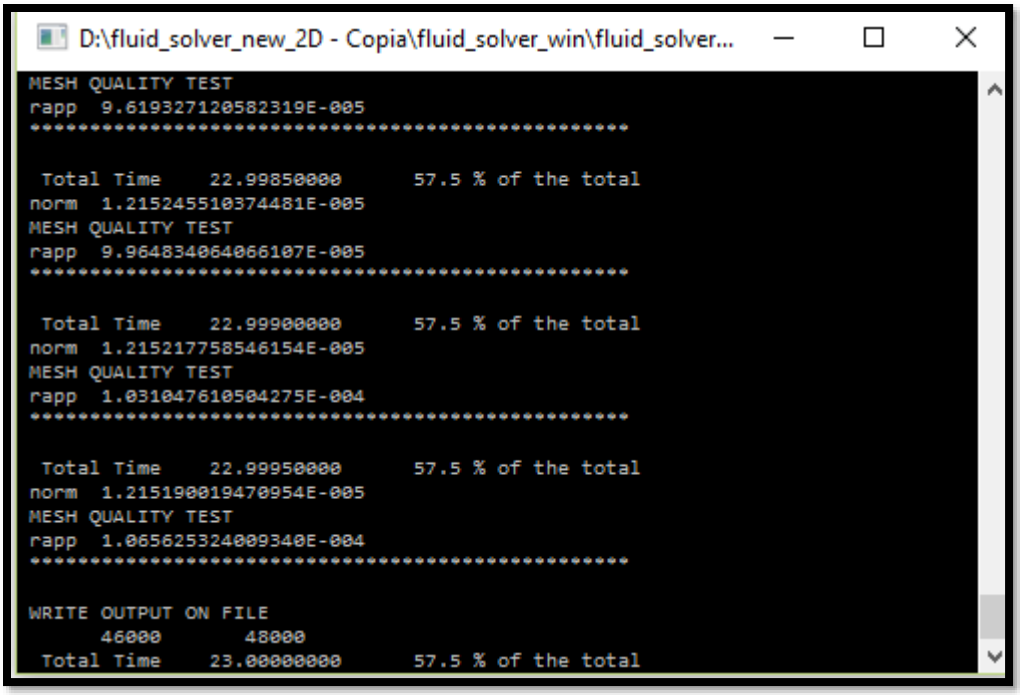

Figure 11. Code Solver. (Source: Dr. Massimiliano Cremonesi, Politecnico di Milano, 2016)

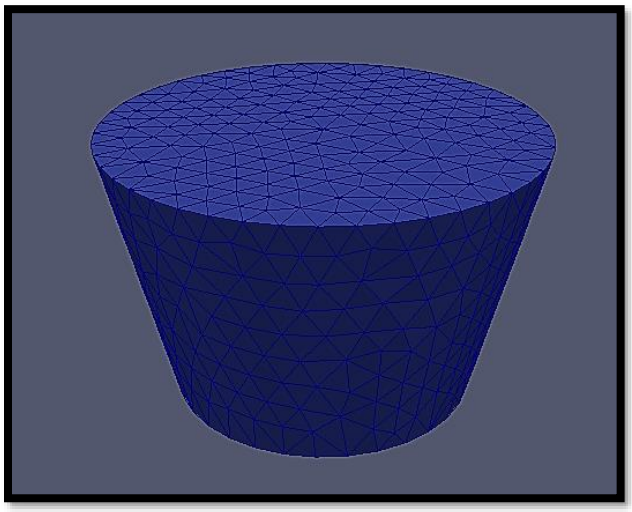

Figure 12. Mini-slumpcone 3D Numerical Model. (Source: Own design)

Once the files with extension (.vtk) were obtained, then the program Paraview 5.0.1. was used in order to visualize the modelling. The software's tool "Rule" can be used to measure the distance between finite elements. For this case, this distance measurement process was completed for each time instant and type of cementitious paste.

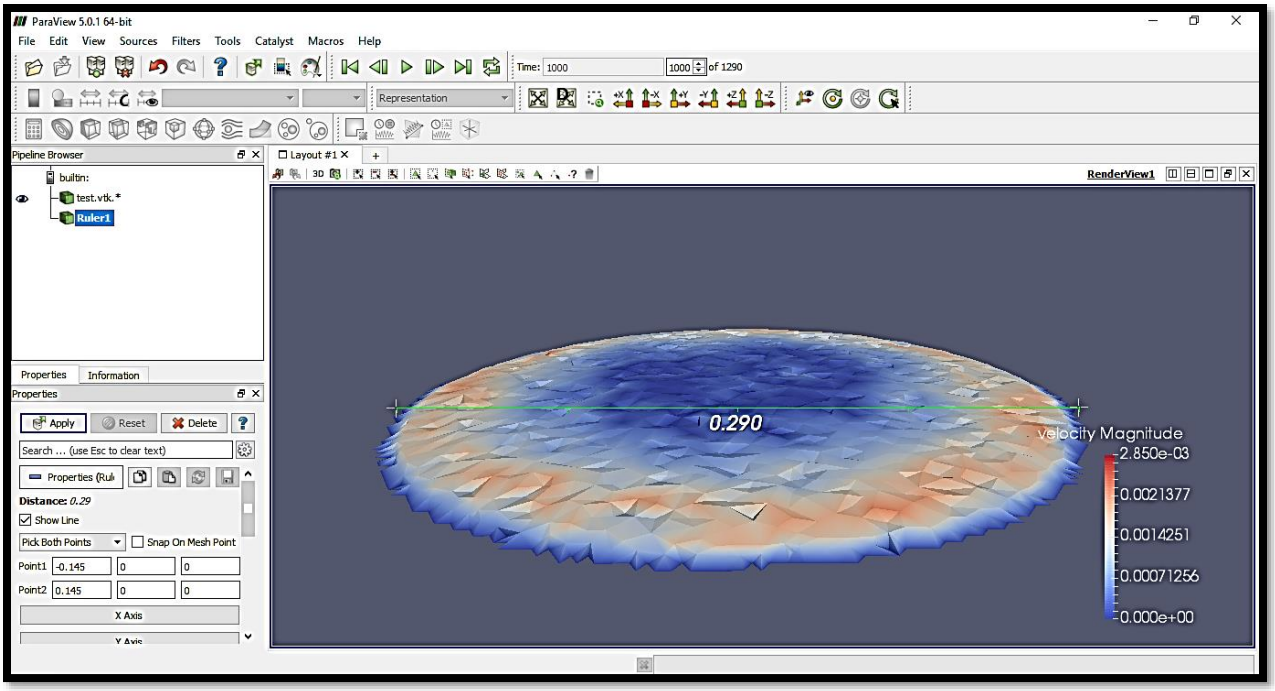

Figure 13. Paraview Viewer 3D Model. (Source: Paraview 5.0.1)

In the case of the 2D numerical model, the initial configuration was based on axisymmetric configuration in order to decrease time-consuming computations.

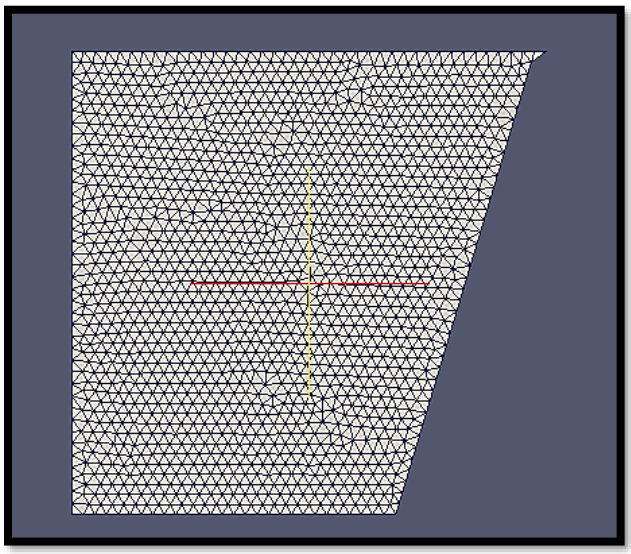

Figure 14. Mini-Cone Slump Flow Test 2D Numerical Model. (Source: Own design)

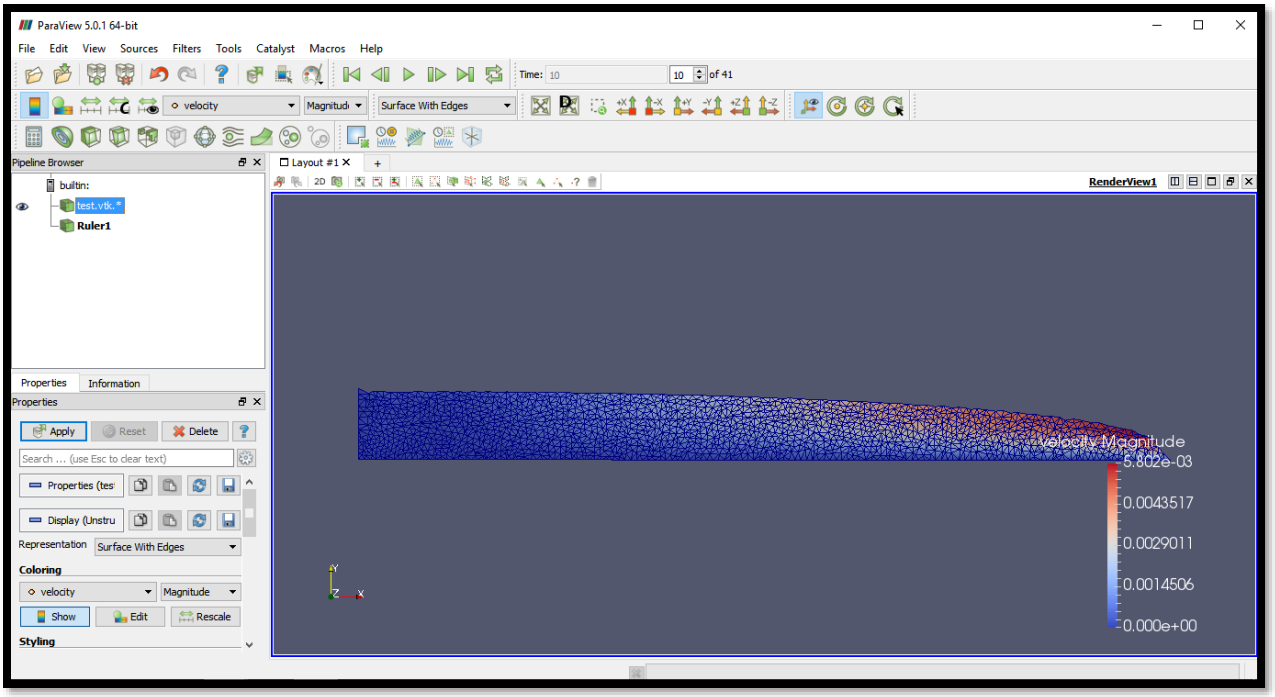

Figure 15. Paraview Viewer 2D Model. (Source: Paraview 5.0.1)

4.7 Results 3D Simulation.

First, in order to set up the analysis, the P0 cementitious paste was chosen due to it is the reference paste. The 3D analysis was implemented with different values of time steps and numbers of elements. The following table shows the results obtained.

P0 Cement Paste

Two delta times were established at 0.0005s and 0.0001s, for 9000 and 20000 finite element discretization. It can be seen in Figure 16 that the smallest delta time tends to be close to the experimental results, while the largest delta time tends to be farther from the experimental results. A better approximation is for 9000 finite element discretization with delta time 0.0001s. Hence, this criterion was adopted for the other cementitious pastes. The 34000 finite element discretization was not implemented due to it demanding excessive computation time. Moreover, when increasing the number of finite element discretization, the results are not close to the experimental results because the model provides a stiff response. Hence, large finite element discretization needs a smaller delta time and the computational cost increases such that modeling requires hours only for one second. For instance, in the case of 9000 finite elements with delta time 0.0001s it last 40 minutes to simulate 1 second of the test, helped by a computer with Core I7 processor. In the case of 9000 finite elements with a delta time

0.00005s, in order to obtain 1s of analysis, the computation last one hour and half, so for this reason the 34000 discretization was no implemented in the Particle Finite Element code.

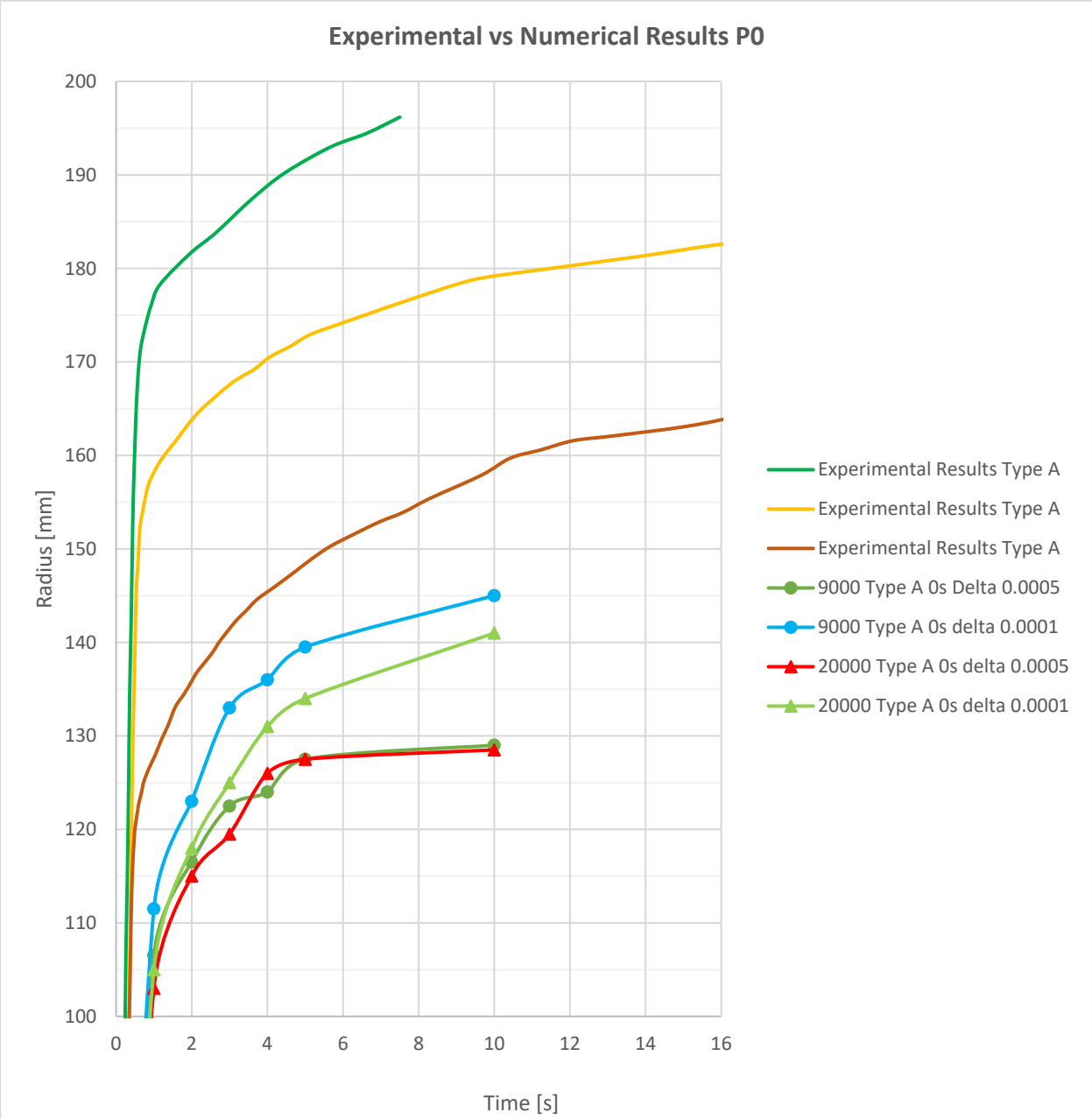

Figure 16. Experimental vs 3D Numerical Results P0. (Source: Own design)

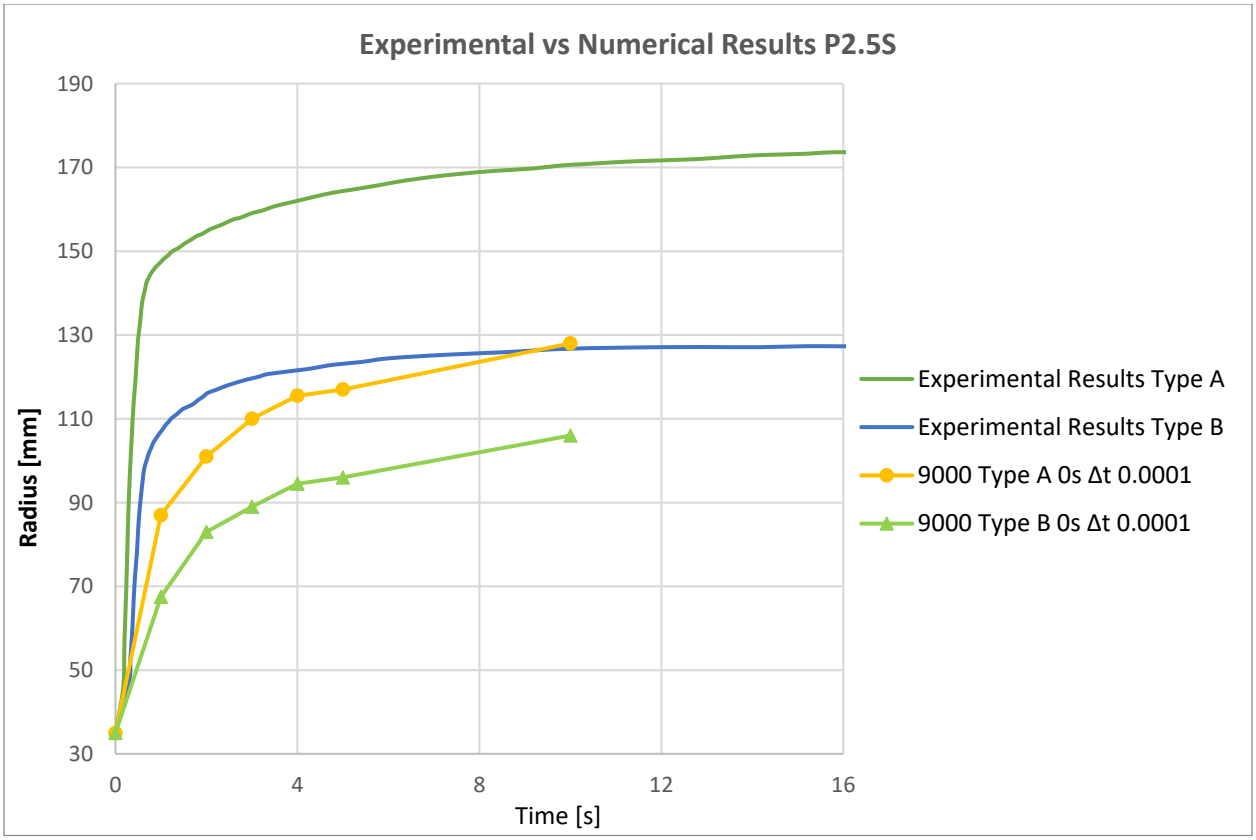

Figure 17. Experimental vs 3D Numerical Results P2.5S. (Source: Own design)

P2.5S Cement Paste

In this case, only one delta time was considered due to the high time computation. Then, the shape of the radius-time simulation curves fit with the experimental results but they are lower-bound with respect to the experimental results (see figure 17). To summarize, the 3D simulation using a code based in the Particle Finite Element method does not bring accurate information about this kind of cement paste.

P4.4S Cement Paste

To analyze the P4.4S cement paste, a 3D simulation was performed in order to obtain information about the radius-time curves, that in this case, are not inside the range of experimental curves. Moreover, the shape of the curves is not well-represented by the simulation after the five seconds due to the asymptotical behavior is not present in the simulation curves (see figure 18). In summary, 3D simulation based in a Particle Finite Element code could not be implemented for the research of this kind of cement paste.

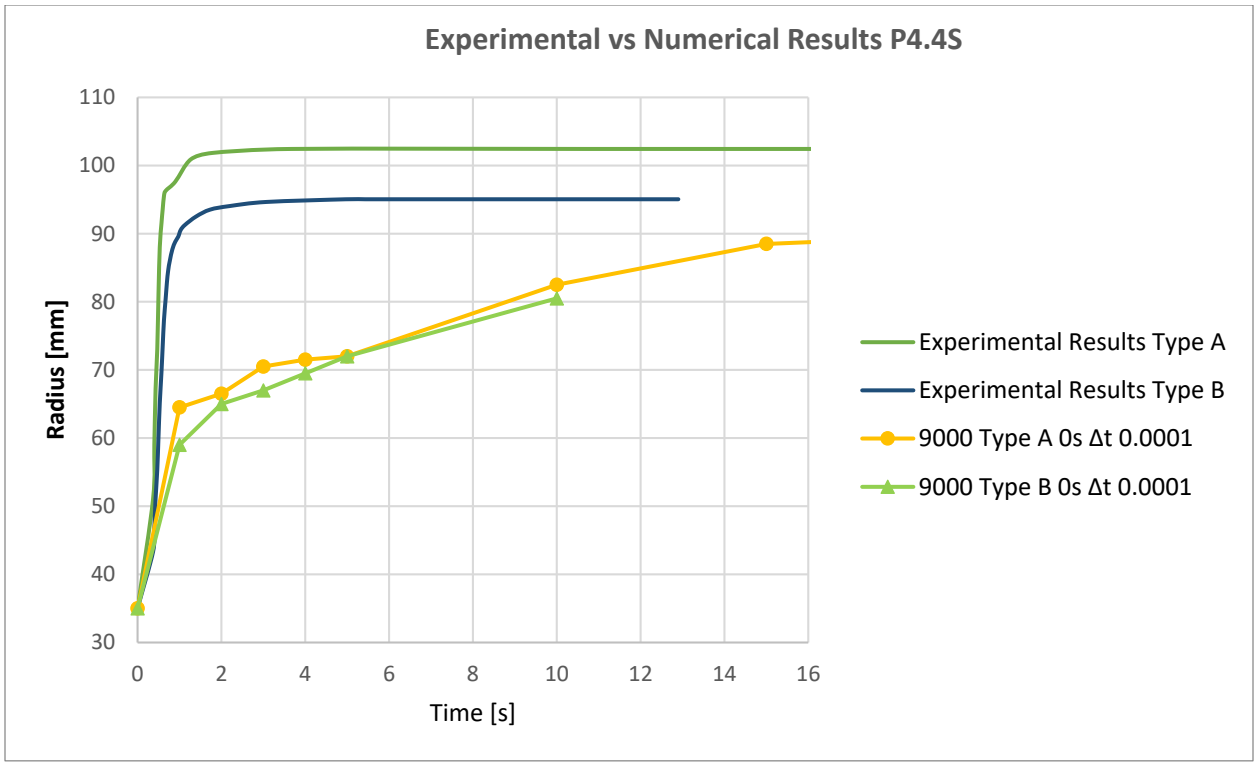

Figure 18. Experimental vs 3D Numerical Results P4.4S. (Source: Own design)

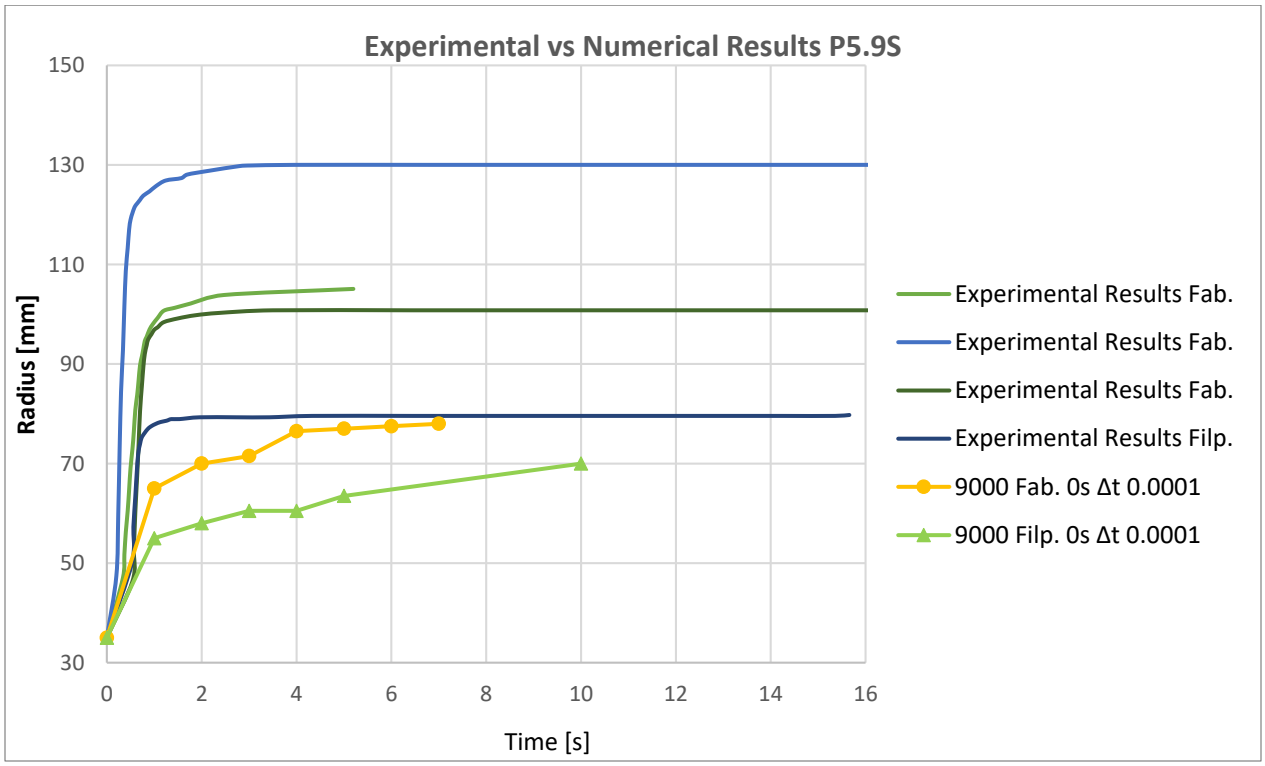

Figure 19. Experimental vs 3D Numerical Results P5.9S. (Source: Own design)

P5.9S Cement Paste

Analyzing the results of the P5.9S cement paste; the values of the radius are lower with respect to experimental results for the type A and B (see figure 19). The shape of the radius-simulation curves is similar than experimental results but only the case B tend to the convergence despite of at the starting second the simulation curve is far from experimental results. In summary, the 3D analysis developed with a Particle Finite element code does not provide approximated behavior of this kind of cement paste with the implementation of 0.0001 this delta time computation.

P2.5X Cement Paste

The figure 20 shows the comparison between experimental and numerical results of P2.5X cement paste. In this case, the shape of the radius time simulation curve fits with the experimental results but it is lower than the experimental curve. The type B simulation curve provides an approximate shape of the experimental curve, but the response goes down with compared with the experimental curve. Moreover, it could be seen that the gap between type A and B of the experimental results is larger than the distance between simulation curves. To summarize, this cement paste is not able to display a well-simulation with the use of a small delta time, in a Particle Finite Element code.

P4.4X Cement Paste

In the figure 21, the radius-time simulation curve provides an accurate representation of the shape of experimental curve. In contrast, the values of the radius in the simulation curve are lower than experimental results. In the type B, the shape is approximated, compared to the experimental curve and the values of the simulation radius are still lower. As consequence, this kind of cement paste is not well-simulated when a small delta time, in a Particle Finite Element code is implemented.

P5.9X Cement Paste

The figure 22 presents the radius-time experimental vs numerical curves of this cement paste. The type A is well-simulated, if only the shape of the curve is contrasted. In other hand, the values of the radius are lower than experimental results, so the simulation curve is not inside the range of experimental data. Then, the type B case after the first second, the simulation curve grows up with a constant slope but the simulation curve increases with a variable slope, so the shape of the curve is not well-represented. To conclude, this cement paste behavior is not keep for a Particle Finite Element code when a small delta time is implemented.

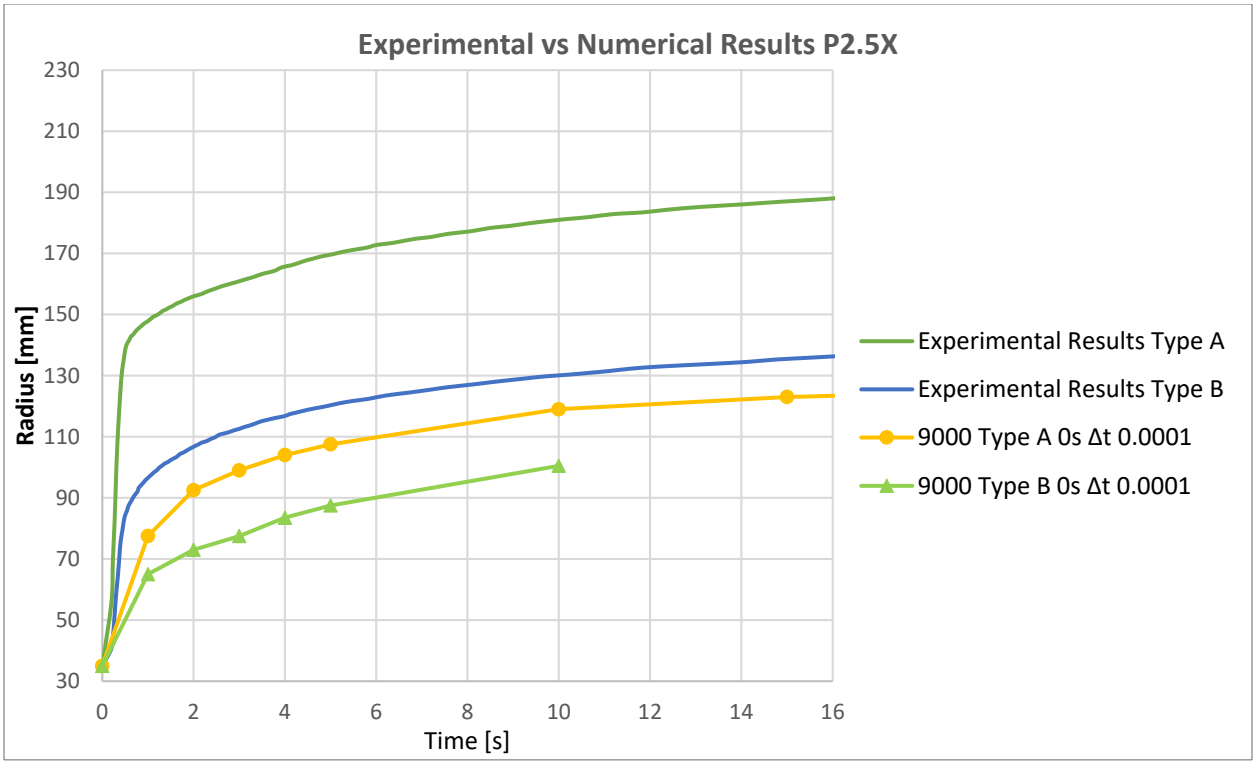

Figure 20. Experimental vs 3D Numerical Results P2.5X. (Source: Own design)

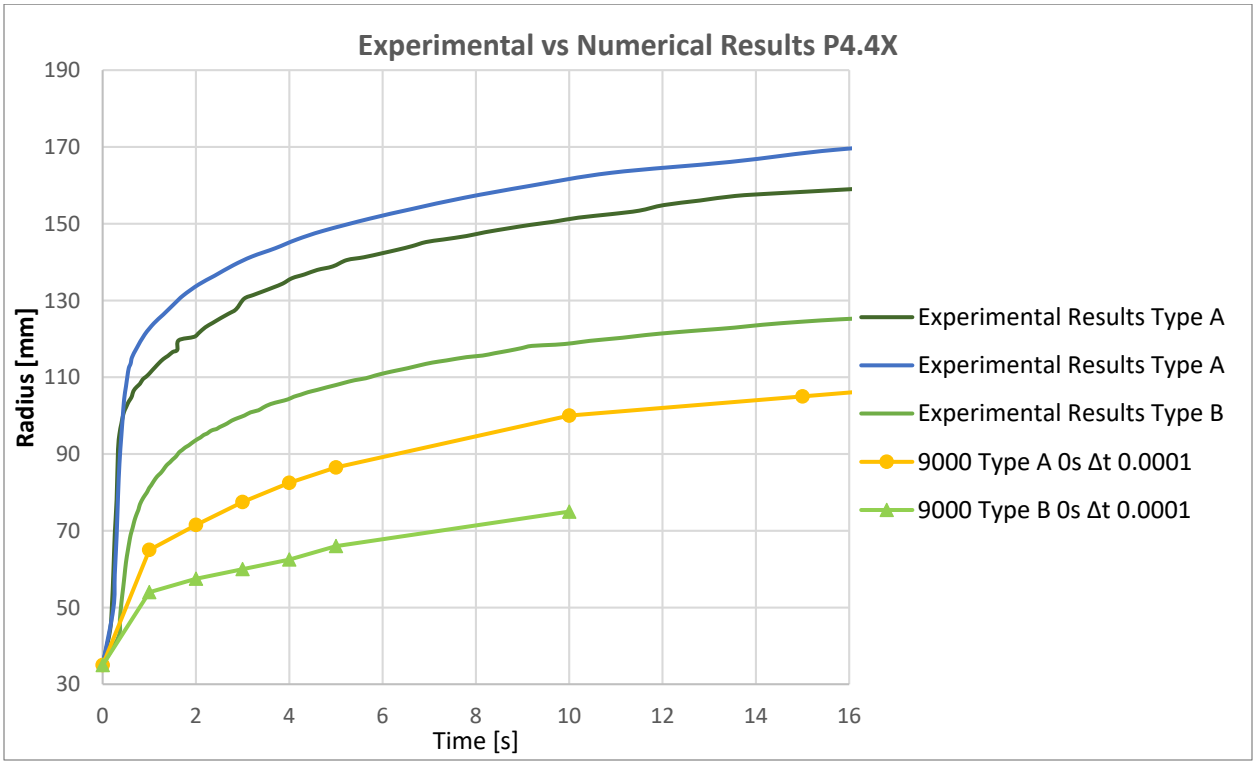

Figure 21. Experimental vs 3D Numerical Results P4.4X (Source: Own design)

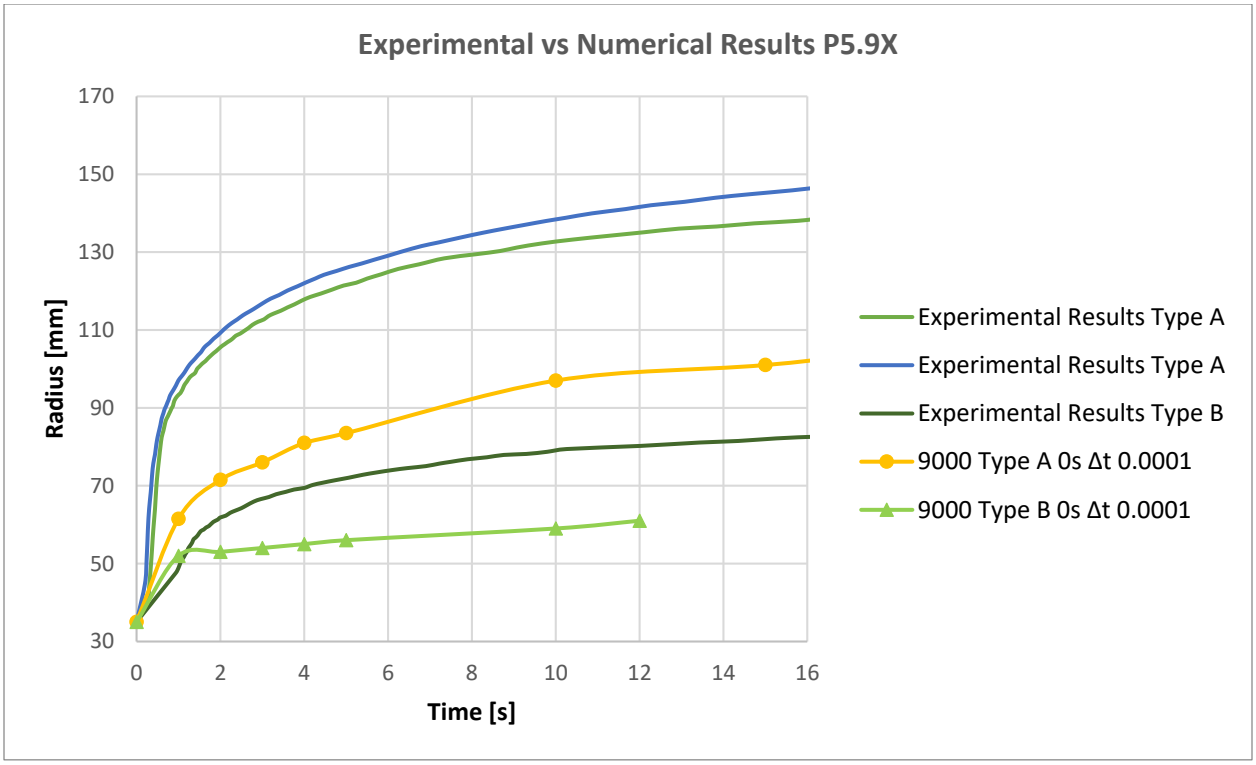

Figure 22. Experimental vs 3D Numerical Results P5.9X. (Source: Own design)

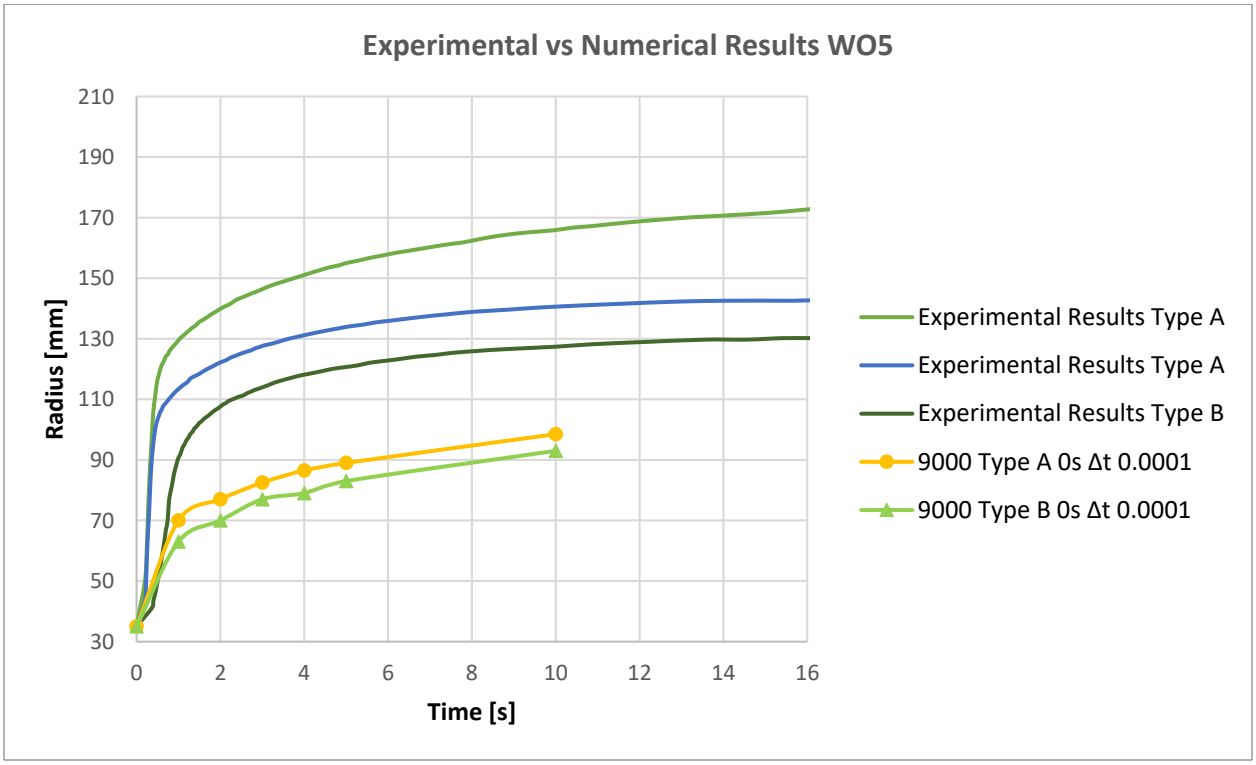

Figure 23. Experimental vs 3D Numerical Results WO5. (Source: Own design)

WO5 Cement Paste

Analyzing the results of the simulation for this cement paste, we could notice that the slope of the simulation tends to be constant in the first five seconds (see figure 23). In contrast the experimental curves have a variable change of slope. Then the gap between the type A and B is smaller for simulation curves than experimental curves. In summary, this kind of cement paste, a Particle Finite code is not useful to simulate this behaviour, so a smaller delta time is needed but computational cost increases.

WO7.5 Cement Paste

The implementation of a small delta time for the analysis depicted in the figure 24, provides an approximate shape for radius-time type A curve. Indeed, the type B is less accurate than type A and shows a tendency of constant slope. Moreover, the difference between the type A and B curves is smaller for numerical results than experimental results. As consequence, using a small delta time, in a 3D simulation with a Particle Finite element code, does not provide an adequate simulation of this cement paste.

WO10 Cement Paste

Starting from this cement paste, only the type A material property was simulated (see figure 25) because it required a lot of time-computation and all the previous cases the simulation curves, are lower than experimental curves. The particularity of this simulation curve is that the slope of the simulation curve decreases in function of time but after 4 second, it increases. This variable change of slope demonstrates that, using this discretization and small delta time, is not enough to represent a decreasing slope.

WN5 Cement Paste

Comparing the experimental and numerical radius-time curves, through the figure 26, we could notice that the shape of the simulation curve fits with the shape of the experimental curves with the use of a 3D simulation and a small delta time. In other hand, the values of the radius in the simulation data, is smaller than experimental results. As consequence, modeling the material properties of this cement paste, with a 3D Particle Finite Element code, provides a lower-bound response.

WN7.5 Cement Paste

In the simulation of this cement paste, a small delta time was set up. The data was displayed in the figure 27. The representation of the behaviour provides a simulation curve with three constant slopes which does not fit with experimental results. Furthermore, the simulation radius is smaller than experimental one. As consequence, the representation of this cement paste does not provide an approximation to the experimental data.

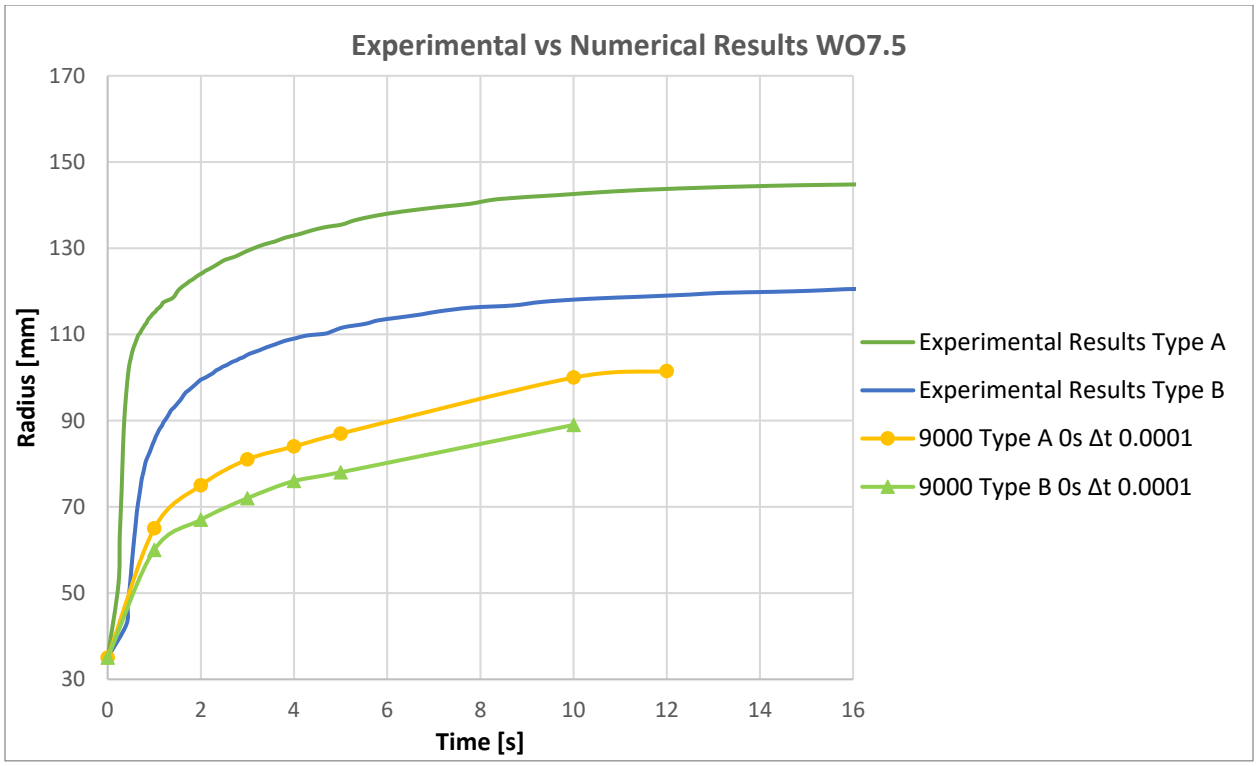

Figure 24. Experimental vs 3D Numerical Results WO7.5. (Source: Own design)

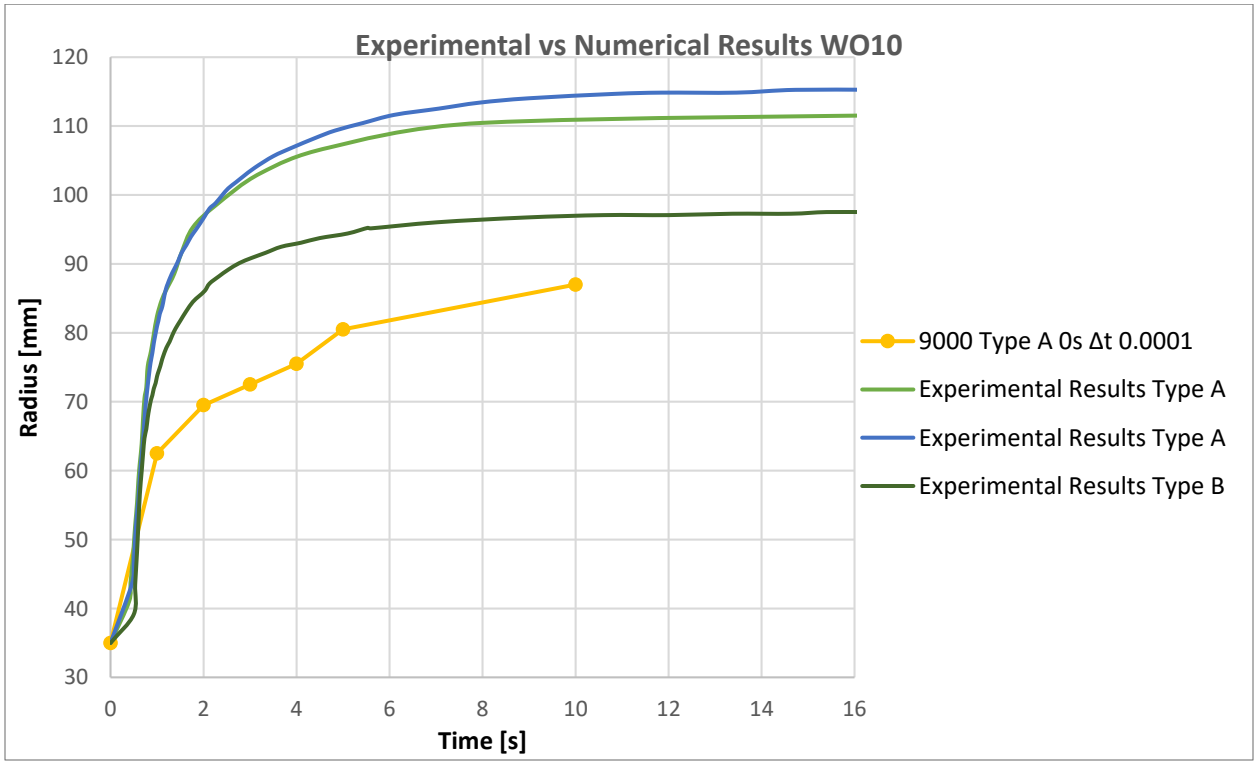

Figure 25. Experimental vs 3D Numerical Results WO10. (Source: Own design)

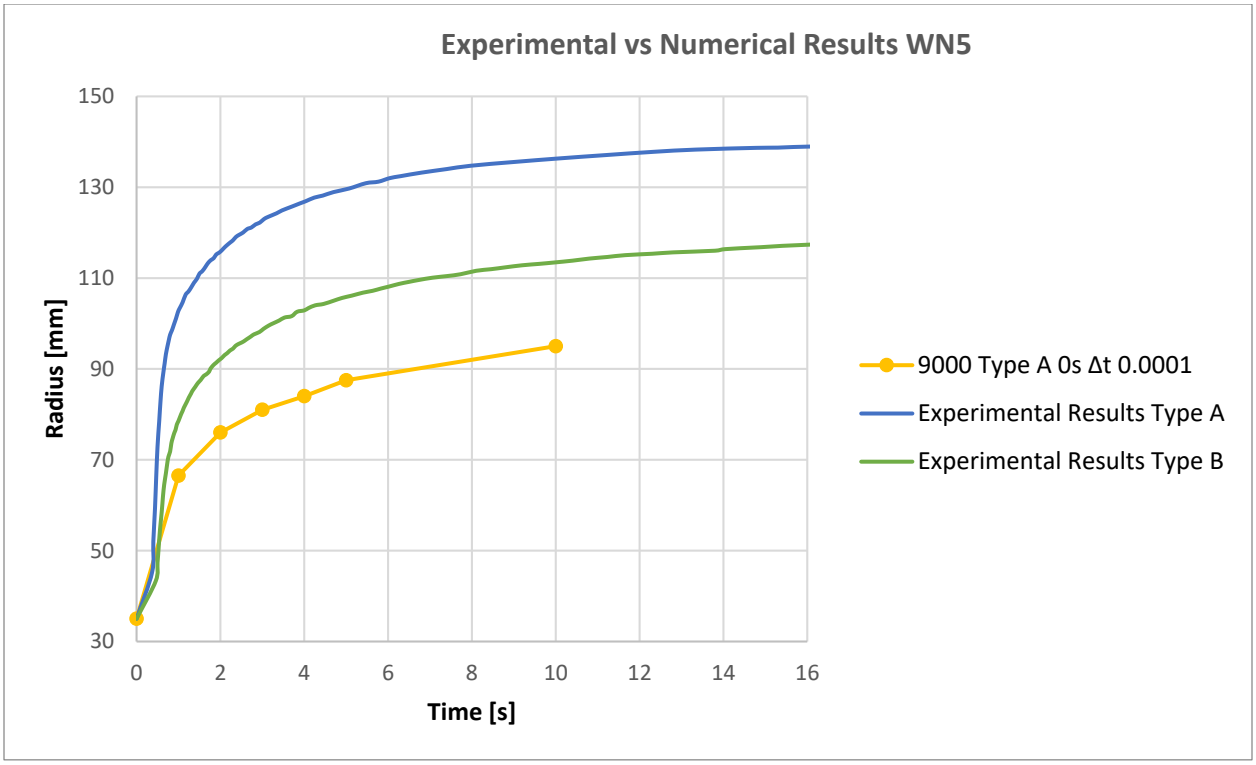

Figure 26. Experimental vs 3D Numerical Results WN5. (Source: Own design)

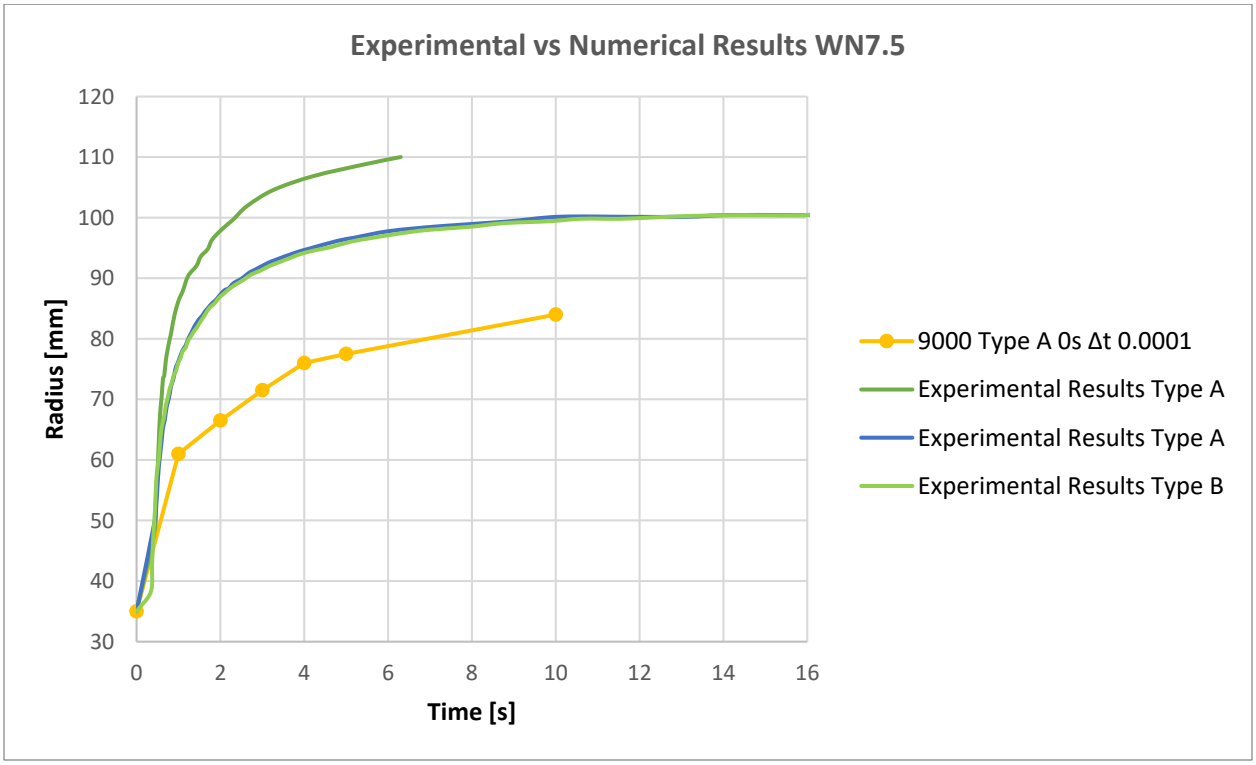

Figure 27. Experimental vs 3D Numerical Results WN7.5. (Source: Own design)

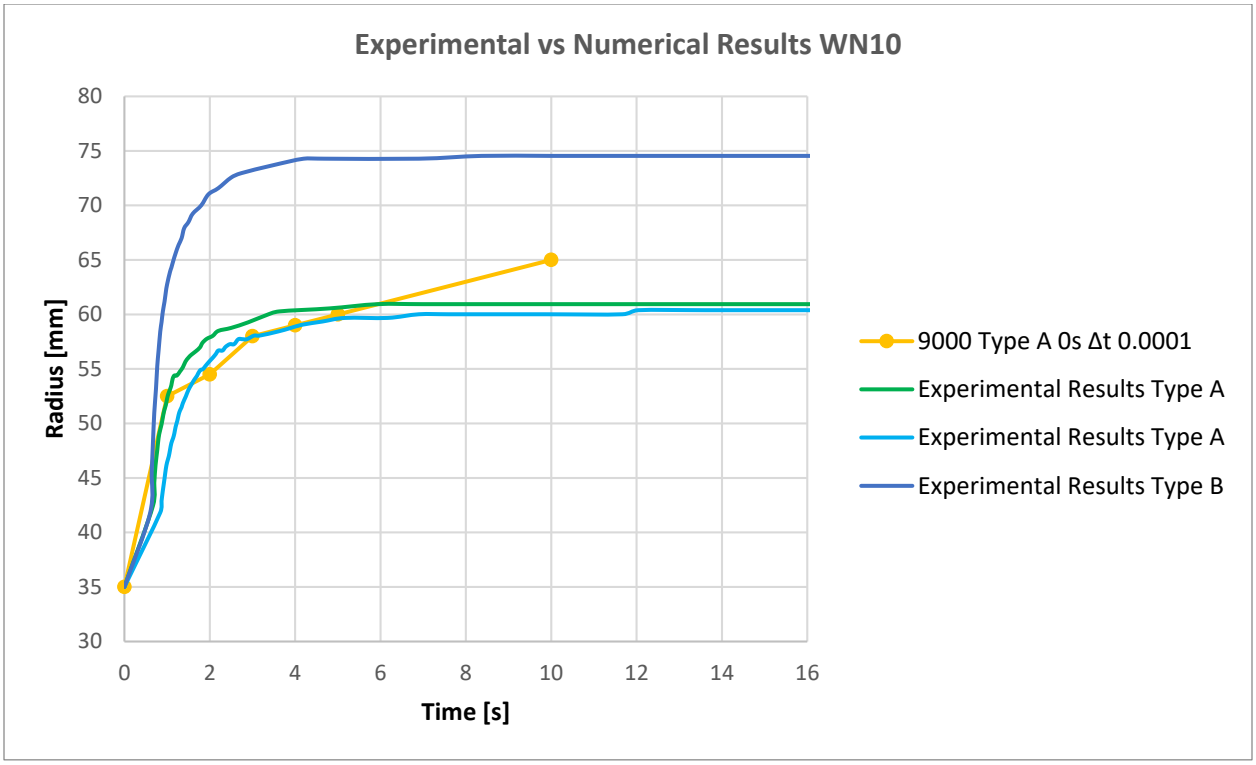

Figure 28. Experimental vs 3D Numerical Results WN10. (Source: Own design)

WN10 Cement Paste

The figure 28 shows the data of the radius that a 3D Particle Finite Element code provides and the experimental results of the mini-slump cone. It could be notice that the values of the simulation radius in the first seconds does not provide a constant slope, so the shape is not accurate compared to the experimental results. Moreover, the numerical radius values keep increasing. To conclude, the data obtained from a Particle Finite element code provides an approximation of the behaviour of this cement paste in the first seconds using a delta time 0.0001s.

In summary, the 3D simulation whose discretization is based in tetrahedron finite element, was discretized with large number of finite elements in order to obtain a better accurate response. This criterion provides a stiff response for this kind of highly fluid cement pastes, because the number of finite elements was raised, despite of the fact that the delta time computation was very small. As consequence, the time-computation increase exponentially, so a simplest 2D model was needed in order to simulate this kind of cement pastes.

4.8 Results 2D Simulation.

The 2D numerical model, based on the Particle Finite Element, was developed by Dr. Massimiliano Cremonesi, Politecnico di Milano. This model was discretized in 1800 triangular finite elements Figure 10. The sample has the standard dimensions of the mini-cone slump test (Figure 8) with the particularity that the symmetric shape was exploited. The input are the the rheological parameters, such as yield stress and viscosity, whose units are [Pa] and [mPa.s] respectively, and the physical property is the density. This simulation is in function of time, the input requirements in the code are the initial time, final time, delta time, and frequency. The delta time is the discretization had been decreased until the simulation curves converge to the experimental curves as the Figure 29 describes it. At the same time the time-computation was considered in order to simulate the slump-cone test in a reasonable time.

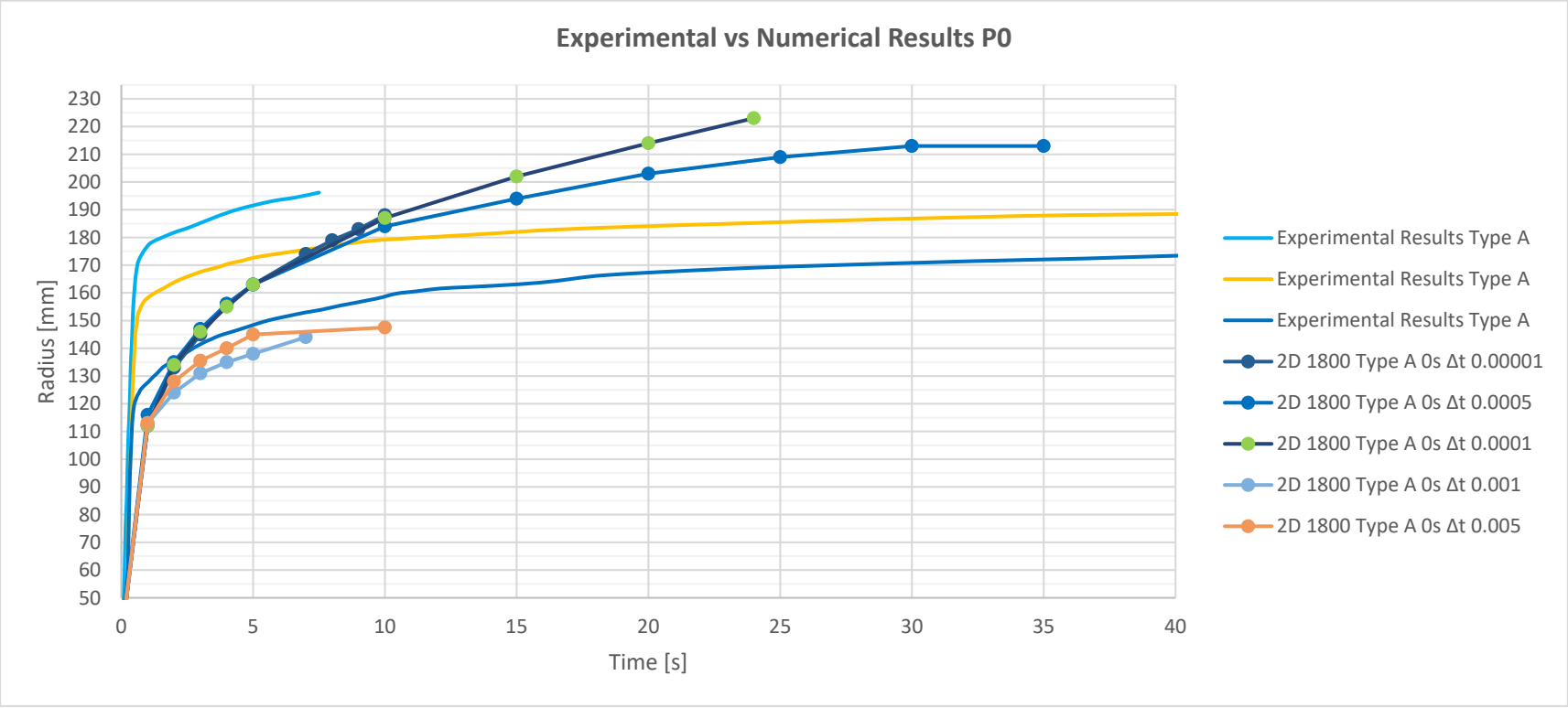

Figure 29. Experimental vs 3D and 2D Numerical Results P0. (Source: Own design)

The choice of the value 2.0 dm^3 for density in the following cementitious pastes must be justified: WO5, WO7.5, WO10, WN5, WN7.5, and WN10. Due to the numerical curves for WO7.5 having the same shape compared to the experimental results, the variation of the density was established in this material. The values of viscous plasticity and shear stress remained the same for this analysis. The values of the densities that were simulated are the following: 1.5dm^3, 1.75dm^3, 2.0dm^3, and 2.25dm^3.

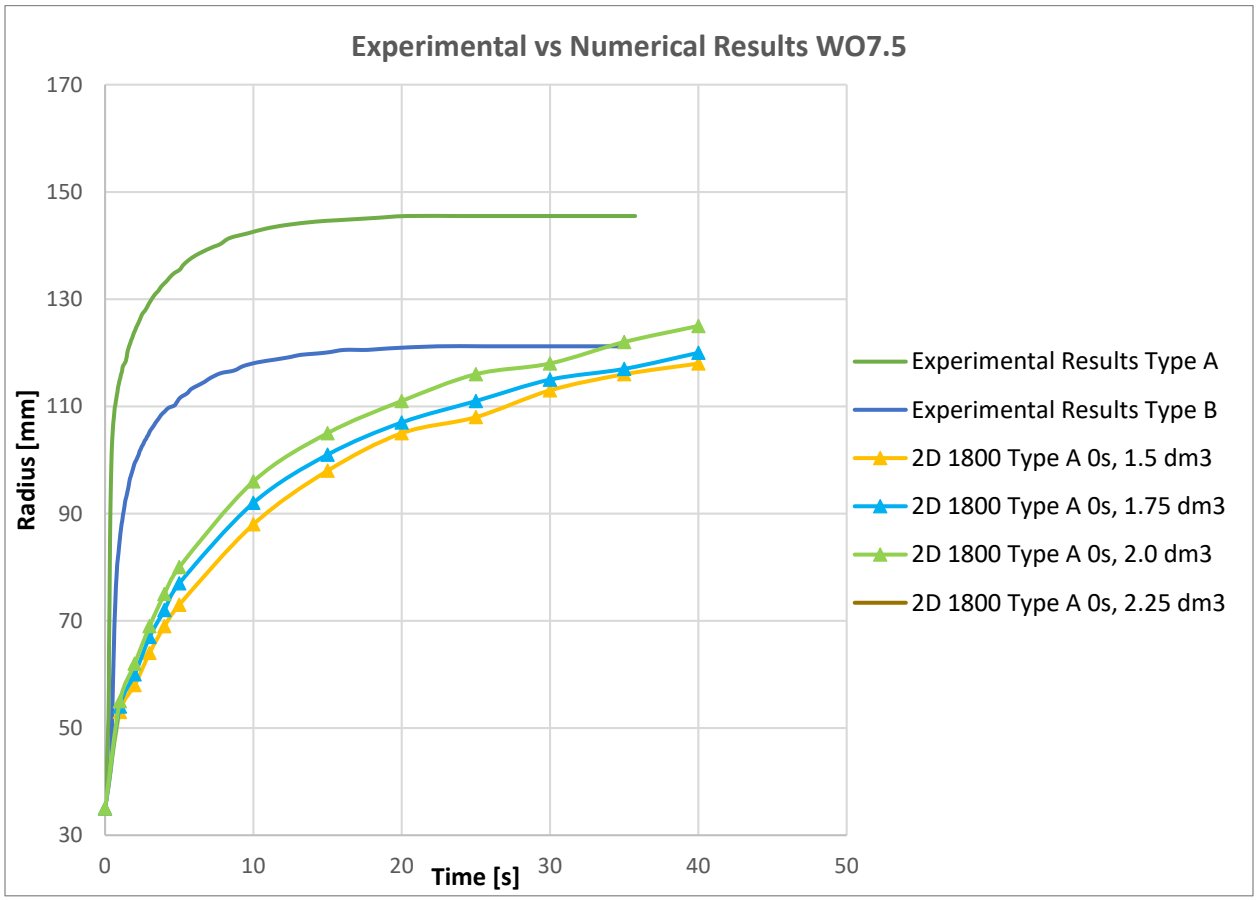

Figure 30. Experimental vs 2D Numerical Results WO7.5 with Variable density. (Source: Own design)

Figure 26 shows that the variation of the density does not provide a significant change in the tendency of the numerical simulation curves. Having higher values of density, the curves translate vertically with an average increase of 2 mm per variation of 0.25 dm^3 in the material's density. As a result, a typical value of 2.0 dm^3 was selected for the following cementitious pastes: WO5, WO7.5, WO10, WN5, WN7.5, and WN10.

Referred to the tables 1, 2 and 3 (data provided by the Laboratory Politecnico di Milano), in general, the type A is less viscous than type B, so the radius of the experimental data is larger than type B. Moreover, these tables provide data for different experimental rest-time 0s, 10s, 60s, 300s and 600s. Average values where computed in order to simplify the comparison between different rest-times 0s, 10s, 60s, 300s and 600s, per each cement paste. This computation is shown in the tables 8 and 9. All those values of the tables 1, 2 and 3 where simulated in order to find out which of them tend to the experimental results. Due to the material properties values are similar for the same cement paste, the curves are crowded with each other and they are arranged in parallel. Hence, the conclusions are only focused in the type A or B in order to simplify the analysis.

Based in the tables 1, 2 and 3, the maximum experimental and simulation radius with the correspond error were included in the following tables:

		Cementitious Pastes		P0	P2.5S	P4.4S	P5.9S	P2.5X
	Type	Density	[g/cm^3]	1.7500	1.7100	1.6800	1.6425	1.6950
0 s	A	Yield Stress (τ_{0de})	[Pa]	2.2794	4.0418	56.7000	46.1000	2.0932
		Viscosity (μ_{0des})	[mPa.s]	15.5260	39.8365	32.8518	62.6570	82.2938
		$R_{max,xp}$	[mm]	196	175	102	130	207
		$R_{max,sim}$	[mm]	213	183	188	151	160
		Error	%	9%	4%	84%	16%	23%
	B	Yield Stress (τ_{0de})	[Pa]	2.6871	12.5000	52.2000	92.1000	3.6076
		Viscosity (μ_{0des})	[mPa.s]	13.6079	81.5409	148.8770	159.7742	237.7174
		$R_{max,xp}$	[mm]	147	128	95	80	147
		$R_{max,sim}$	[mm]	231	160	136	120	120
		Error	%	57%	25%	43%	50%	18%
10 s	A	Yield Stress (τ_{0de})	[Pa]	2.2048	4.0517	56.0000	53.1000	1.8229
		Viscosity (μ_{0des})	[mPa.s]	16.2330	41.5758	54.0930	55.7326	81.3703
		$R_{max,xp}$	[mm]	196	175	102	130	207
		$R_{max,sim}$	[mm]	214	183	172	155	158
		Error	%	9%	4%	68%	54%	24%
	B	Yield Stress (τ_{0de})	[Pa]	2.6761	13.4000	53.7000	98.2000	5.8475
		Viscosity (μ_{0des})	[mPa.s]	138.7163	74.0360	122.0066	160.7407	202.3250
		$R_{max,xp}$	[mm]	147	128	95	80	147
		$R_{max,sim}$	[mm]	143	159	144	120	128
		Error	%	3%	24%	52%	50%	13%

		Cementitious Pastes		P0	P2.5S	P4.4S	P5.9S	P2.5X
60 s	A	**Yield Stress (τ_{0de})**	[Pa]	2.1383	4.1131	54.9000	47.5000	1.7903
		Viscosity (μ_{0des})	[mPa.s]	16.5321	46.1713	63.0440	65.7486	82.6982
		$R_{max,xp}$	[mm]	196	175	102	130	207
		$R_{max,sim}$	[mm]	208	181	167	139	160
		Error	%	6%	3%	63%	7%	23%
	B	**Yield Stress (τ_{0de})**	[Pa]	3.2796	12.7000	56.2000	104.2000	5.0659
		Viscosity (μ_{0des})	[mPa.s]	131.8548	89.3001	141.3150	159.1870	207.8906
		$R_{max,xp}$	[mm]	147	128	95	80	147
		$R_{max,sim}$	[mm]	145	158	139	120	129
		Error	%	1%	23%	46%	50%	12%
300 s	A	**Yield Stress (τ_{0de})**	[Pa]	2.7526	5.0210	58.5000	52.7000	2.0432
		Viscosity (μ_{0des})	[mPa.s]	14.6437	38.9169	70.7622	91.3906	79.1328
		$R_{max,xp}$	[mm]	196	175	102	130	207
		$R_{max,sim}$	[mm]	193	186	163	139	162
		Error	%	2%	6%	59%	7%	22%
	B	**Yield Stress (τ_{0de})**	[Pa]	3.1430	14.3000	60.0000	115.4000	3.2664
		Viscosity (μ_{0des})	[mPa.s]	140.6548	91.8065	153.4899	153.2690	237.0583
		$R_{max,xp}$	[mm]	147	128	95	80	147
		$R_{max,sim}$	[mm]	143	154	133	120	122
		Error	%	3%	20%	40%	50%	17%
600 s	A	**Yield Stress (τ_{0de})**	[Pa]	2.1708	6.1699	65.3000	64.1000	2.3608
		Viscosity (μ_{0des})	[mPa.s]	18.9071	43.8605	58.7116	55.0917	78.0679
		$R_{max,xp}$	[mm]	196	175	102	130	207
		$R_{max,sim}$	[mm]	205	181	170	154	163
		Error	%	4%	3%	66%	18%	21%
	B	**Yield Stress (τ_{0de})**	[Pa]	4.4222	16.8000	70.2000	138.1000	5.6508
		Viscosity (μ_{0des})	[mPa.s]	140.9091	94.0070	165.0868	141.3077	215.9764
		$R_{max,xp}$	[mm]	147	128	95	80	147
		$R_{max,sim}$	[mm]	143	157	133	125	126
		Error	%	3%	23%	40%	57%	14%

Table 5. Material Properties, Maximum Radius and Error computed for rest-times 0s, 10s, 60s, 300s and 600s. (Source: Own Design)

		Cementitious Pastes		P4.4X	P5.9X	WO5	WO7.5	WO10
	Type	Density	[g/cm^3]	1.6633	1.6350	2.0000	2.0000	2.0000
0 s	A	Yield Stress (τ_{0de})	[Pa]	2.9882	2.6990	19.7000	5.3112	24.4000
		Viscosity (μ_{0des})	[mPa.s]	243.6591	292.3454	134.1394	264.7648	258.1350
		$R_{max,xp}$	[mm]	179	163	187	146	115
		$R_{max,sim}$	[mm]	122	117	148	125	122
		Error	%	32%	24%	21%	14%	6%
	B	Yield Stress (τ_{0de})	[Pa]	9.6565	16.1000	15.7000	16.1000	46.9000
		Viscosity (μ_{0des})	[mPa.s]	1063.0742	4191.5577	281.2545	354.8092	497.2433
		$R_{max,xp}$	[mm]	136	85	131	121	98
		$R_{max,sim}$	[mm]	87	59	120	117	108
		Error	%	36%	31%	9%	3%	11%
10 s	A	Yield Stress (τ_{0de})	[Pa]	3.3837	2.3776	10.5000	5.3983	25.3000
		Viscosity (μ_{0des})	[mPa.s]	217.2593	271.9523	156.9456	263.2387	254.7735
		$R_{max,xp}$	[mm]	179	163	187	146	115
		$R_{max,sim}$	[mm]	125	120	141	125	126
		Error	%	30%	26%	15%	14%	9%
	B	Yield Stress (τ_{0de})	[Pa]	9.7846	17.6000	16.4000	17.5000	48.5000
		Viscosity (μ_{0des})	[mPa.s]	1035.5716	3818.0141	287.6152	330.0423	501.8807
		$R_{max,xp}$	[mm]	136	85	131	121	98
		$R_{max,sim}$	[mm]	87	61	121	116	109
		Error	%	36%	28%	23%	15%	9%
60 s	A	Yield Stress (τ_{0de})	[Pa]	3.3142	2.0751	12.2000	5.9277	27.4000
		Viscosity (μ_{0des})	[mPa.s]	210.7307	286.6128	151.7439	257.2182	252.5886
		$R_{max,xp}$	[mm]	179	163	187	146	115
		$R_{max,sim}$	[mm]	124	118	144	124	126
		Error	%	31%	28%	23%	15%	9%
	B	Yield Stress (τ_{0de})	[Pa]	9.0912	23.3000	17.7000	17.4000	50.0000
		Viscosity (μ_{0des})	[mPa.s]	1057.5202	2988.1864	268.8600	340.8226	505.1871
		$R_{max,xp}$	[mm]	136	85	131	121	98
		$R_{max,sim}$	[mm]	87	65	125	120	109
		Error	%	36%	24%	5%	1%	12%
300 s	A	Yield Stress (τ_{0de})	[Pa]	3.4281	3.1533	16.1000	7.5696	33.2000
		Viscosity (μ_{0des})	[mPa.s]	219.5707	228.1393	135.4674	251.8754	237.6368

		Cementitious Pastes		P4.4X	P5.9X	WO5	WO7.5	WO10
		$R_{max,xp}$	[mm]	179	163	187	146	115
		$R_{max,sim}$	[mm]	124	122	150	125	127
		Error	%	31%	25%	20%	14%	10%
	B	Yield Stress (τ_{0de})	[Pa]	10.9000	23.9000	19.4000	19.6000	54.8000
		Viscosity (μ_{0des})	[mPa.s]	928.8831	3400.3674	312.4510	349.0077	520.7643
		$R_{max,xp}$	[mm]	136	85	131	121	98
		$R_{max,sim}$	[mm]	89	63	120	119	107
		Error	%	35%	26%	9%	2%	10%
600 s	A	Yield Stress (τ_{0de})	[Pa]	4.6404	3.2283	24.3000	11.9000	45.5000
		Viscosity (μ_{0des})	[mPa.s]	195.7630	220.6722	118.5600	249.0532	236.6258
		$R_{max,xp}$	[mm]	179	163	187	146	115
		$R_{max,sim}$	[mm]	130	122	152	128	128
		Error	%	28%	25%	19%	12%	11%
	B	Yield Stress (τ_{0de})	[Pa]	12.7000	30.7000	23.8000	22.6000	63.1000
		Viscosity (μ_{0des})	[mPa.s]	895.0871	3564.3190	311.1173	358.0263	548.3386
		$R_{max,xp}$	[mm]	136	85	131	121	98
		$R_{max,sim}$	[mm]	90	61	119	117	117
		Error	%	34%	29%	10%	3%	20%

Table 6. Material Properties, Maximum Radius and Error computed for rest-times 0s, 10s, 60s, 300s and 600s. (Source: Own Design)

		Cementitious Pastes		WN5	WN7.5	WN10	WN10*
	Type	Density	[g/cm^3]	2.0000	2.0000	2.0000	2.0000
0 s	A	Yield Stress (τ_{0de})	[Pa]	16.2000	33.6000	135.5000	80.8000
		Viscosity (μ_{0des})	[mPa.s]	184.7478	236.6999	316.7646	444.1309
		$R_{max,xp}$	[mm]	139	110	60	61
		$R_{max,sim}$	[mm]	134	126	117	112
		Error	%	4%	15%	94%	84%
	B	Yield Stress (τ_{0de})	[Pa]	16.1000	27.6000	88.9000	
		Viscosity (μ_{0des})	[mPa.s]	305.3824	320.3551	473.5064	
		$R_{max,xp}$	[mm]	119	101	75	
		$R_{max,sim}$	[mm]	121	120	110	
		Error	%	2%	19%	48%	

		Cementitious Pastes		WN5	WN7.5	WN10	WN10*
10 s	A	Yield Stress (τ_{0de})	[Pa]	17.7000	34.4000	128.4000	79.4000
		Viscosity (μ_{0des})	[mPa.s]	163.1065	253.0665	370.2741	464.8038
		$R_{max,xp}$	[mm]	139	110	60	61
		$R_{max,sim}$	[mm]	142	124	116	109
		Error	%	2%	13%	92%	79%
	B	Yield Stress (τ_{0de})	[Pa]	23.3000	28.5000	88.7000	
		Viscosity (μ_{0des})	[mPa.s]	307.5937	319.8535	482.7491	
		$R_{max,xp}$	[mm]	119	101	75	
		$R_{max,sim}$	[mm]	121	119	110	
		Error	%	2%	18%	48%	
60 s	A	Yield Stress (τ_{0de})	[Pa]	19.7000	37.1000	128.3000	81.5000
		Viscosity (μ_{0des})	[mPa.s]	162.8505	242.9251	375.9547	449.4547
		$R_{max,xp}$	[mm]	139	110	60	61
		$R_{max,sim}$	[mm]	141	129	116	112
		Error	%	1%	17%	92%	84%
	B	Yield Stress (τ_{0de})	[Pa]	18.2000	29.9000	91.9000	
		Viscosity (μ_{0des})	[mPa.s]	305.6857	324.3618	485.7913	
		$R_{max,xp}$	[mm]	119	101	75	
		$R_{max,sim}$	[mm]	121	116	110	
		Error	%	2%	15%	48%	
300 s	A	Yield Stress (τ_{0de})	[Pa]	25.4000	44.1000	138.0000	90.9000
		Viscosity (μ_{0des})	[mPa.s]	155.4822	242.5367	363.4431	438.3816
		$R_{max,xp}$	[mm]	139	110	60	61
		$R_{max,sim}$	[mm]	144	127	117	111
		Error	%	3%	15%	94%	82%
	B	Yield Stress (τ_{0de})	[Pa]	19.7000	33.3000	97.3000	
		Viscosity (μ_{0des})	[mPa.s]	302.9620	335.1477	541.6295	
		$R_{max,xp}$	[mm]	119	101	75	
		$R_{max,sim}$	[mm]	119	119	107	
		Error	%	0%	18%	44%	
600 s	A	Yield Stress (τ_{0de})	[Pa]	36.3000	57.4000	157.0000	109.3000
		Viscosity (μ_{0des})	[mPa.s]	149.1821	238.9826	361.7009	460.3774
		$R_{max,xp}$	[mm]	139	110	60	61

		Cementitious Pastes		WN5	WN7.5	WN10	WN10*
		$R_{max,sim}$	[mm]	145	126	117	111
		Error	%	4%	20%	94%	82%
	B	Yield Stress (τ_{0de})	[Pa]	23.5000	39.7000	106.2000	
		Viscosity (μ_{0des})	[mPa.s]	327.2747	346.8311	616.0262	
		$R_{max,xp}$	[mm]	119	101	75	
		$R_{max,sim}$	[mm]	117	118	103	
		Error	%	2%	17%	38%	

Table 7. Material Properties, Maximum Radius and Error computed for rest-times 0s, 10s, 60s, 300s and 600s. (Source: Own Design)

	Average values		P0	P2.5S	P4.4S	P5.9S	P2.5X	P4.4X	P5.9X
A	Yield Stress (τ_{0de})	[Pa]	2.31	4.68	58.28	52.70	2.02	3.55	2.71
	Viscosity (μ_{0des})	[mPa.s]	16.37	42.07	55.89	66.12	80.71	217.40	259.94
	Error	%	6%	4%	68%	14%	22%	30%	27%
B	Yield Stress (τ_{0de})	[Pa]	3.24	13.94	58.46	109.60	4.69	10.43	22.32
	Viscosity (μ_{0des})	[mPa.s]	113.15	86.14	146.16	154.86	220.19	996.03	3592.49
	Error	%	2%	23%	44%	52%	15%	35%	28%

Table 8. Average values of 0s, 10s, 60s, 300s and 600s. (Source: Own Design)

	Average values		WO5	WO7.5	WO10	WN5	WN7.5	WN10	WN10*
A	Yield Stress (τ_{0de})	[Pa]	16.56	7.22	31.16	23.06	41.32	137.44	88.38
	Viscosity (μ_{0des})	[mPa.s]	139.37	257.23	247.95	163.07	242.84	357.63	451.43
	Error	%	21%	14%	9%	3%	15%	93%	82%
B	Yield Stress (τ_{0de})	[Pa]	18.60	18.64	52.66	20.16	31.80	94.60	
	Viscosity (μ_{0des})	[mPa.s]	292.26	346.54	514.68	309.78	329.31	519.94	
	Error	%	8%	3%	13%	1%	17%	45%	

Table 9. Average values of 0s, 10s, 60s, 300s and 600s. (Source: Own Design)

The different composition of cement paste was developed from the right to the left according to the table 1 where the mix design is shown. It could be notice that the variation of the quantities of SBR, XSBR or Wallastonite, influence in the material properties of each cement paste.

The figures 31 and 32 represent the summary of the variation of the Maximum experimental and simulation average radius, rest-time average yield Stress, rest-time average plastic viscosity, and average error, when the percentage of SBR varies in the cement paste type A and B, which means that the reference paste is P0.

P0 Cement Paste

This behaviour of the P0 cement paste is represented in the figure 33. The yield stress experimental data is between 2.14Pa to 2.75Pa whose average value is 2.31Pa for the type A. The yield stress experimental data type B has the range between 2.67Pa to 4.42Pa whose average value is 3.24Pa. Next, the type B, the simulation is approximated at the beginning of the radius-time curve but after 25s the experimental and the simulation curves converge each other.

The other rheological material property is the viscosity; the difference between type A and B is considerable large. For instance, the range of values of the viscosity for type A is among 14.64mPa.s to 18.91mPa.s whose average value is 16.37mPas. Then, the type B has a range of values between 131mPa.s to 140mPa.s whose average value is 138mPas. The value of 13mPa.s corresponds to the rest-time 0s was discarded because the difference with respect to the others rest-times is very large and it is seen that tends to the curves of the type A.

The maximum experimental radius for P0 type A is 196mm and for type B case is 147mm. Running the numerical code, simulation radius was obtained, 214mm for type A and 145mm for type B. Moreover, it can be noticed that in the maximum radius between experimental and computational results the average error is 6% and 2% for type A and B, respectively.

These values are represented in the radius-time experimental curves that became constant after 30s for the type A and 25s for type B. This behaviour is well-simulated by the Particle Finite Element Code whose post-processed data is depicted in the radius-time simulation curves. The asymptotic behaviour of the curves starts at the same time that the experimental results. The shape of the radius-time simulation curves is approximate to the experimental results for the case A and B.

The radius-time simulation curves of the type A are inside the radius-time experimental curves range, so this cement paste is well-simulated. As consequence, the simulation based in a Particle Finite Element is adequate to simulate P0 cement paste with a 0.0005s delta time computation.

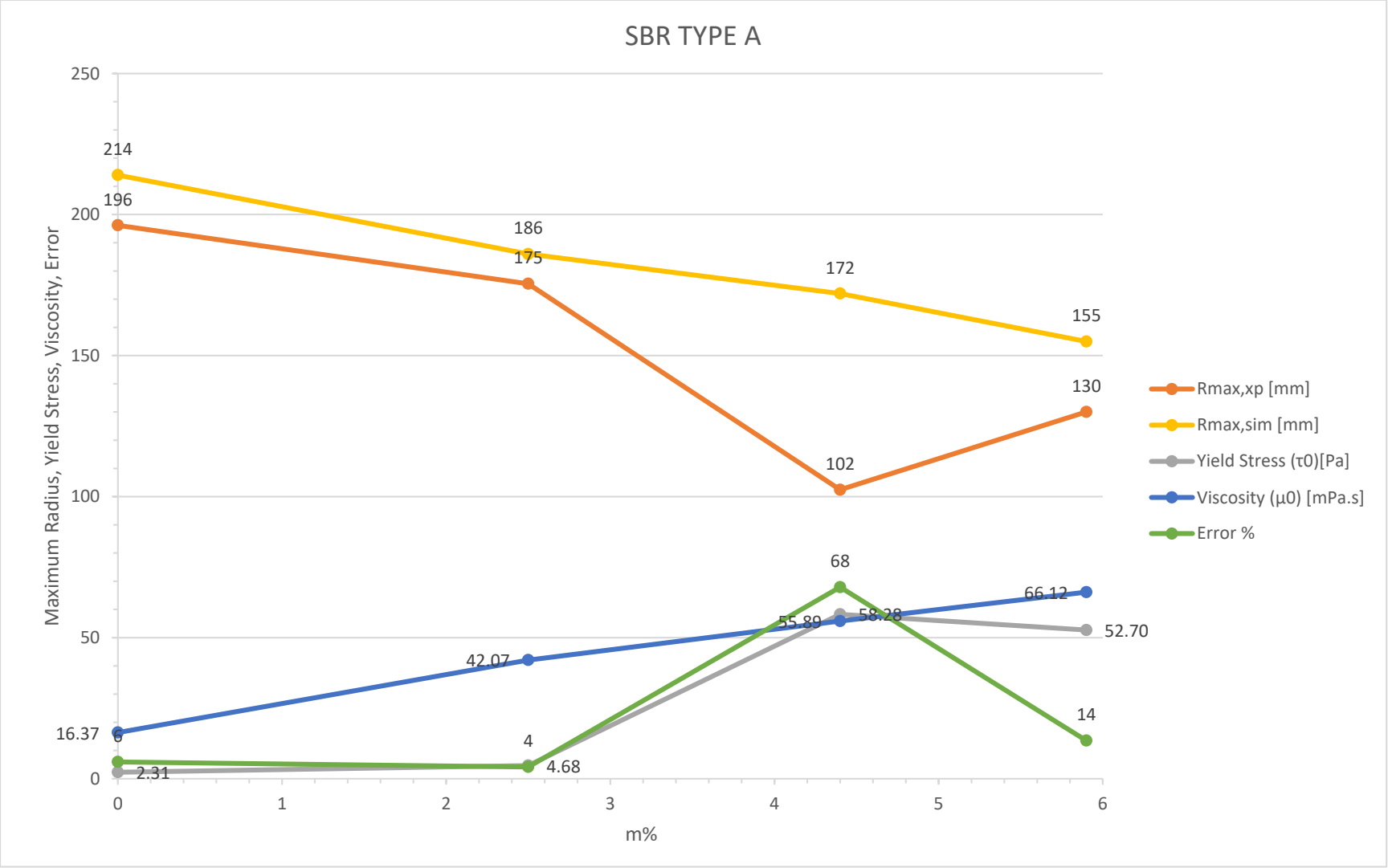

Figure 31. Summary SBR Variation Type A. (Source: Own design)

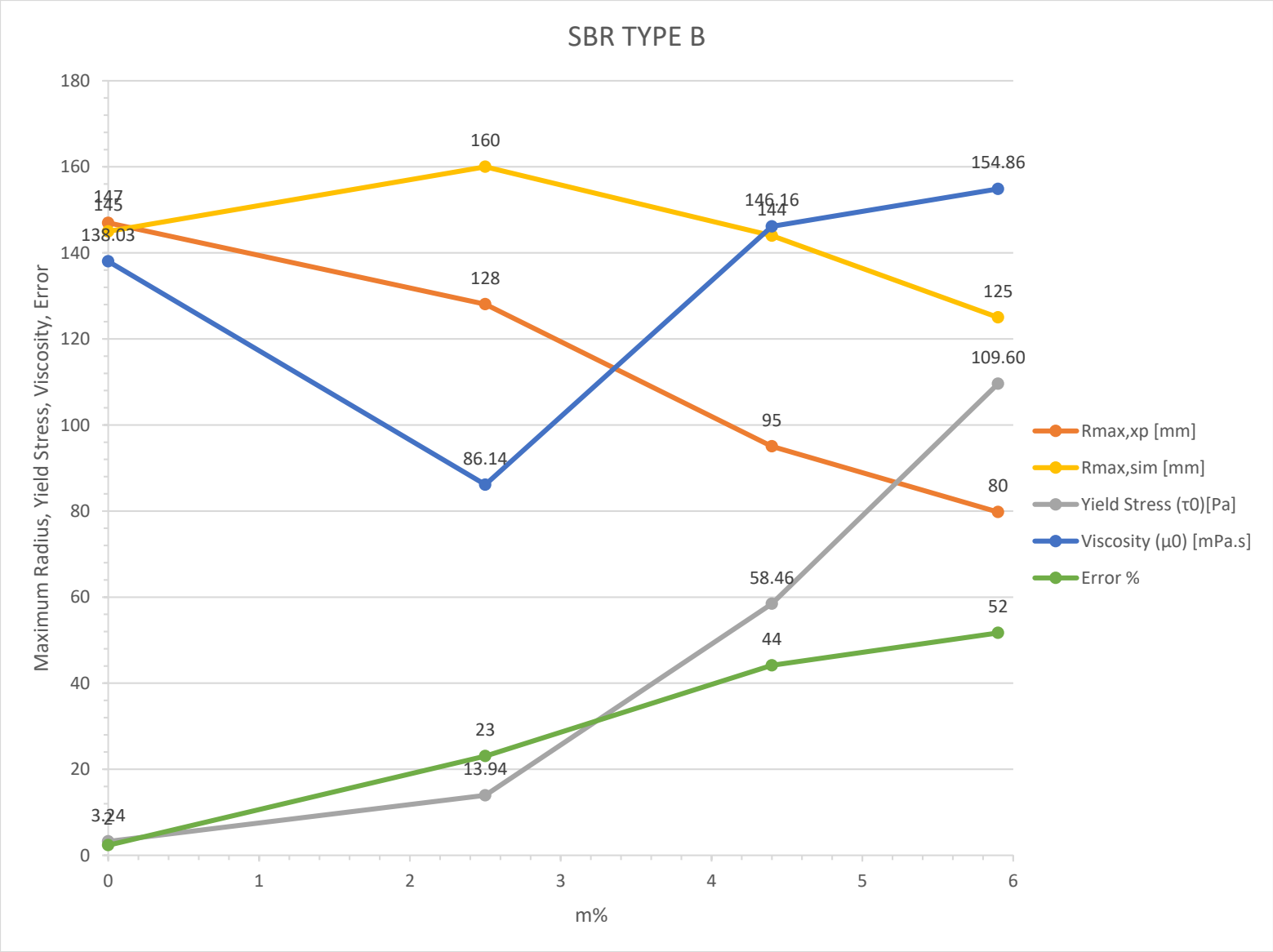

Figure 32. Summary SBR Variation Type B. (Source: Own design)

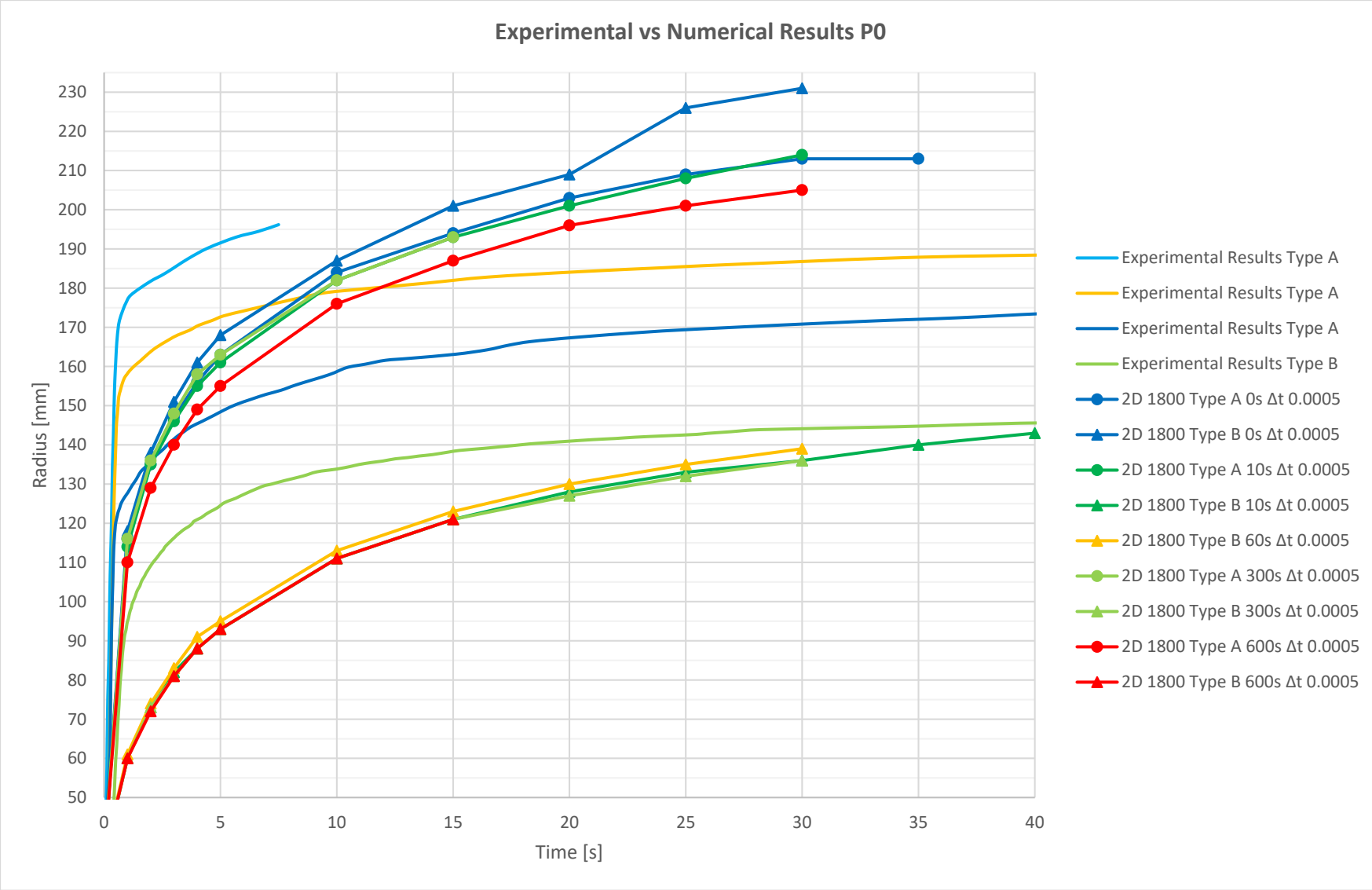

Figure 33. Experimental vs 2D Numerical Results P0. (Source: Own design)

P2.5S Cement Paste

The P2.5S behaviour is pictured in the figure 34. The yield stress experimental results of P2.5S cement paste twice the yield stress value compared to P0. The most common values of viscosity type A are 4.04Pa to 6.20Pa whose average value is 4.68Pa. The type B data are between 12.5Pa and 16.8Pa whose average value is 13.94Pa.

The other material property, the viscosity is 3 times more than P0 cement paste. The type A P2.5S cement paste has a range of viscosity values between 39.8mPa.s to 46.17mPa.s and its average value is 42.07mPa.s. For the type B, the viscosity decreases 38% with respect to the reference paste and the data are around the values 74mPa.s to 94mPa.s, and its average value is 86.14mPa.s. This variation of yield stress and plastic viscosity, is due to the presence of SBR in the cement paste.

As consequence, the maximum experimental radius diminishes from 196mm for P0 cement paste to 175mm for P2.5S type A. It means that the grow of the yield stress and plastic viscosity, slumps the radius. The type B case, the maximum experimental radius is 147mm for P0 and 128mm for P2.5S. Despite of the decrement of plastic viscosity, the experimental radius diminishes; it is due to the increment of yield stress. Hence, the plastic viscosity is not relevant in the experimental radius behaviour. Then, running the code, the maximum simulation radius for type A were obtained: 214mm for P0 and for P2.5S, 186mm. The maximum simulation radius diminishes for the increment of yield stress and plastic viscosity. In another hand, In the type B case, maximum simulation radius raises from 145mm for P0 to 160mm for P2.5s. Despite of the viscosity diminishes; the increment of the yield stress does not help to decrease the value of the simulation radius, so that the viscosity is more relevant in the radius simulation than in the mini-cone slump test. Then, the average radius error between experimental and simulation results is 4% for type A which provides an accurate behaviour but the type B has 23% error. Hence, the increment of the yield stress diminishes the radius.

Then, the P0 cement paste has a constant radius value after 30s for type A and 25s for type B. The experimental radius-time curves for P2.5S cement paste are asymptotic after 20s and 15s for the types A and B, respectively. Hence, the type A simulation curves are close to experimental data curve after 20s. It means that the increment of yield stress enlarges the asymptotic behaviour of the radius-time experimental curves.

The P2.5S simulation curves have different shape respect to the experimental curves. As consequence, the Particle Finite Element code is recommendable to simulate with a 0.0005s delta time computation.

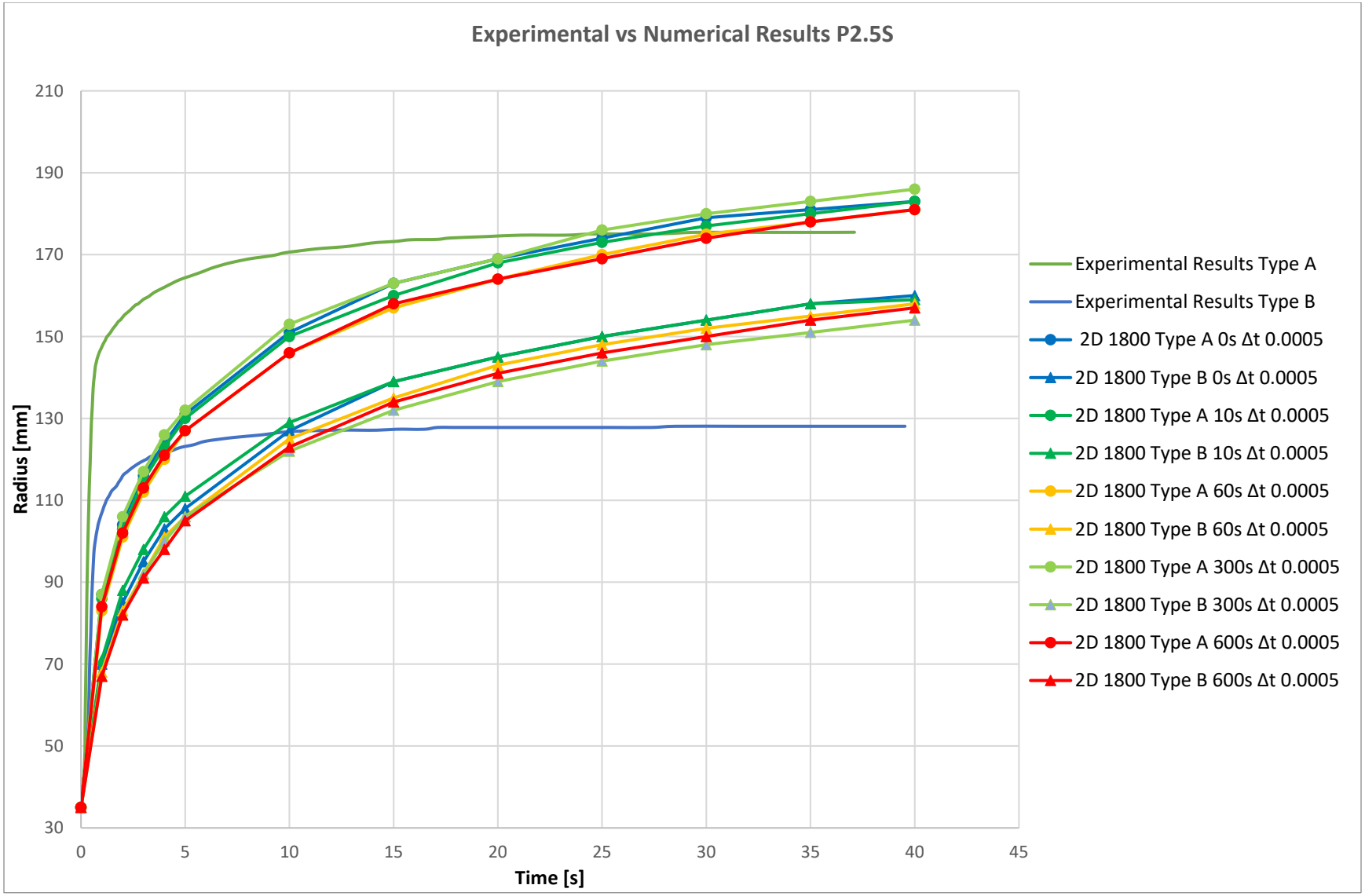

Figure 34. Experimental vs 2D Numerical Results P2.5S. (Source: Own design)

P4.4S Cement Paste

The figure 35 shows the behaviour of the P4.4S cement paste. In this case the P4.4S yield stress is twelve times higher than P2.5S for type A and four times higher than P2.5S in the case of type B. The experimental values of type A yield stress are between 54Pa to 65Pa and the average value is 58.28Pa. The type B data are inside the range 52Pa to 70Pa whose average value is 58.46Pa

The second part is related to the analysis of the viscosity which variation grow up 33% in the type A case and 70% more than P2.5S for type B case. The range of values is between 32mPa.s and 70mPa.s whose average value is 55.89mPa.s for the type A case. In the case of type B, the values of viscosity are around 122mPa.s and 165mPa.s and the average value is 146mPa.s. This variation of yield stress and plastic viscosity, is due to the increment of SBR in the cement paste.

Hence, the radius is influenced for these increments. The maximum value of experimental radius for P2.5S type A is 175mm and drop off to 102mm. The type B case for P2.5S is 128mm goes down to 95mm. After running the code, it is notice that the maximum simulation radius for type A decreases from 186mm for P2.5S and 172mm for P4.4S. The rest time 0s was not considered due to this curve varies with respect to the other rest-time simulation curves. In the type B case, the maximum simulation radius goes down from 160mm for P0 to 144mm for P2.5s. It means the grow of the yield stress and plastic viscosity, slumps the simulation radius. It could be noticed in the radius error between experimental and simulation results whose values are 68% and 44% for the type A and B, respectively. As consequence, the increment of the yield stress decreases the radius.

These data are represented in the radius-time experimental curves, in which, the increment of yield stress results into constant values of radius at 2s for type A and 3s for type B. Comparing to the P2.5S the constant value of radius starts at 20s and 15s for type A and B. The increment of yield stress, diminishes the time where the experimental radius becomes constant. This abrupt change is not kept for the Particle Finite Element code with a 0.0005s delta time computation.

The shape of the radius-time experimental curves does not match with the radius-time simulation curves; the first ones have a platform after few seconds but the simulation curves are continues increasing in the time. In conclusion, the Particle Finite Element implementation does not provide adequate simulation of this kind of cement paste with a 0.0005s delta time computation.

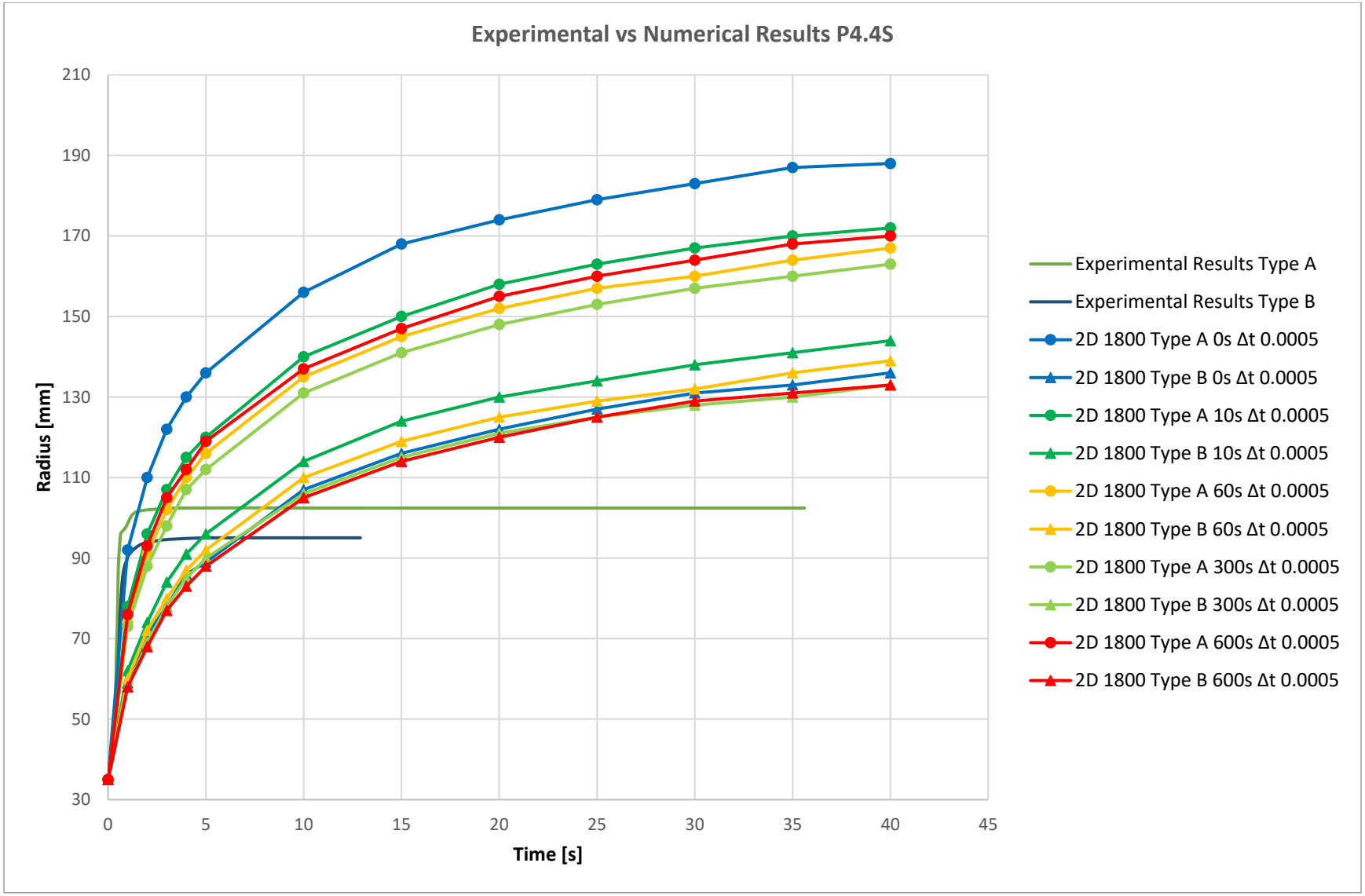

Figure 35. Experimental vs 2D Numerical Results P4.4S. (Source: Own design)

P5.9S Cement Paste

The behaviour of P5.9S is sketched in the figure 36. In comparison between experimental and simulation data of P4.4S and P5.9S cement pastes, the type A yield stress goes down 10%; the common values are 46Pa to 64Pa and the average value 52Pa. The type B, the yield stress grows 87%; the typical values are around 92Pa to 138Pa and the average value is 109Pa.

Then, related with the viscosity, the type A develop an increment of 18%; the range of values is 55Pa to 91Pa and the average value is 66Pa. The type B is 6% higher than P4.4S, the range of values is 141mPa.s to 160mPa.s and the average value is 154mPa.s. This variation of yield stress and plastic viscosity, is due to the increment of SBR in the cement paste.

The maximum value of the experimental radius for P4.4S type A is 102mm and grows to 130mm due to the decrement of yield stress. The type B case for P4.4S is 95mm goes down to 80mm due to the increment of yield stress and plastic viscosity. Running the code, it is notice that the maximum simulation radius for type A decreases, from 172mm for P4.4S to 155mm for P5.9S. Despite of the decrement of yield stress, the increment of plastic viscosity does not help to grow up the value of the simulation radius, so the code is not able to simulate this behaviour. The type B case, the maximum simulation radius diminishes from 144mm for P4.4S to 125mm for P5.9S, so the decrement of yield stress is less influent than the increment of viscosity in the simulation radius. Furthermore, the high average error between simulation and experimental radius, which are 14% for type A and 52% for type B.

It results that the radius-time experimental curves its asymptotic behaviour starts at 2s for P4.4S and 2.8s for P5.9S for type A, so the decrement of yield stress, increases the time where the radius is constant. The type B, the radius-time experimental curves, the constant value of radius starts at 3s P4.4S and 1 s for P5.9S. As consequence, when the yield stress raises, the time where the radius remains constant during the time goes down.

Moreover, the shape of the curves is not similar because the radius-time experimental curves remain constant after 2.8 seconds due to the high values of viscosity, while the radius of the simulation curves continue increasing.

The type A has an upper curve which fit in a wide range of experimental values. In the case of type B, the simulation does not match with radius-time experimental curves. It shows that this cement paste is not well-simulated by the Particle Finite Element code with a 0.0005s delta time computation. As consequence, the simulation is not recommendable to use for this kind of cement paste.

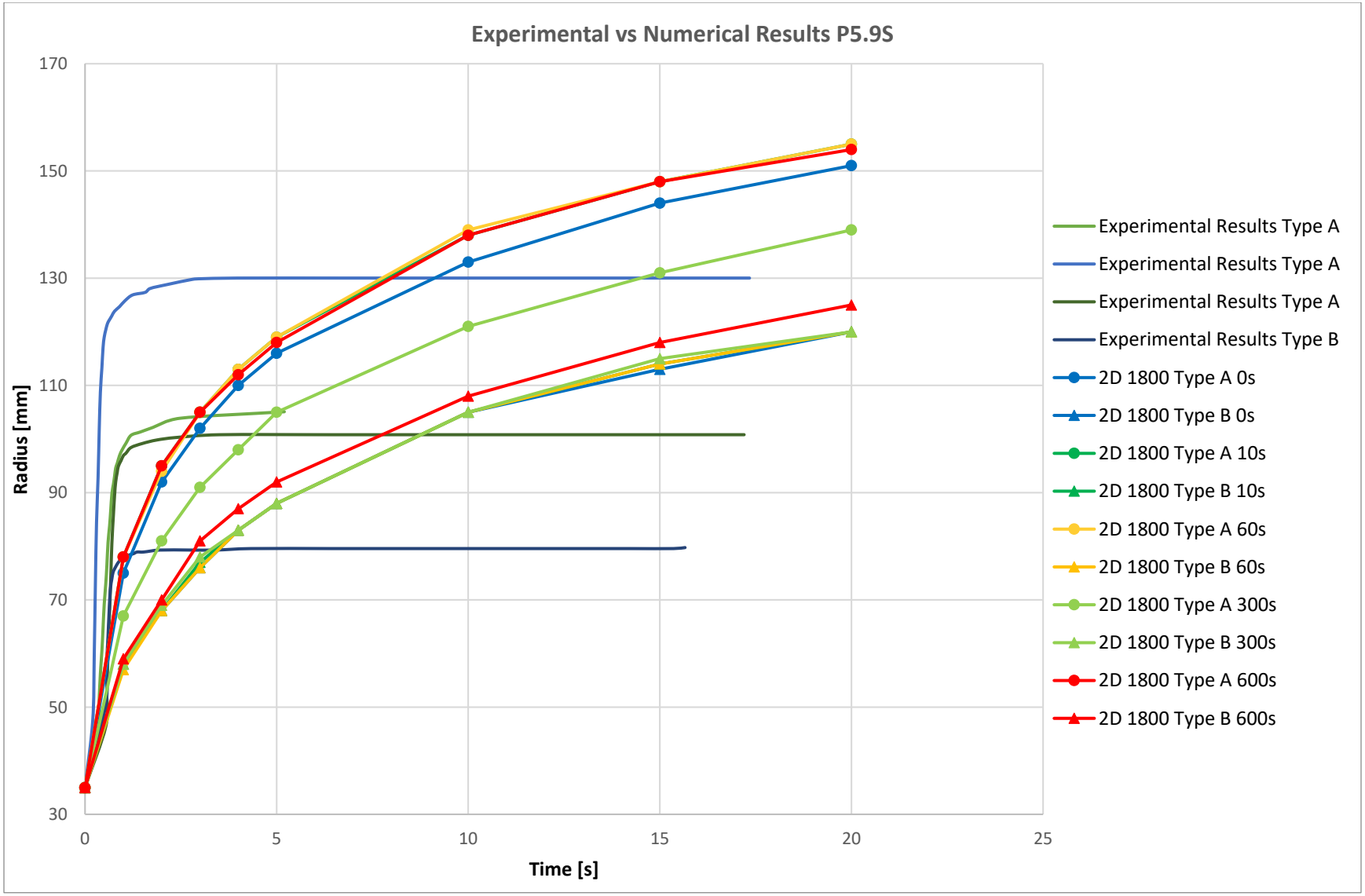

Figure 36. Experimental vs 2D Numerical Results P5.9S. (Source: Own design)

The figures 37 and 38 represent the summary of the variation of the Maximum experimental and simulation average radius, rest-time average yield Stress, rest-time average plastic viscosity, and average error, when the percentage of XSBR varies in the cement paste type A and B, which means that the reference paste is P0.

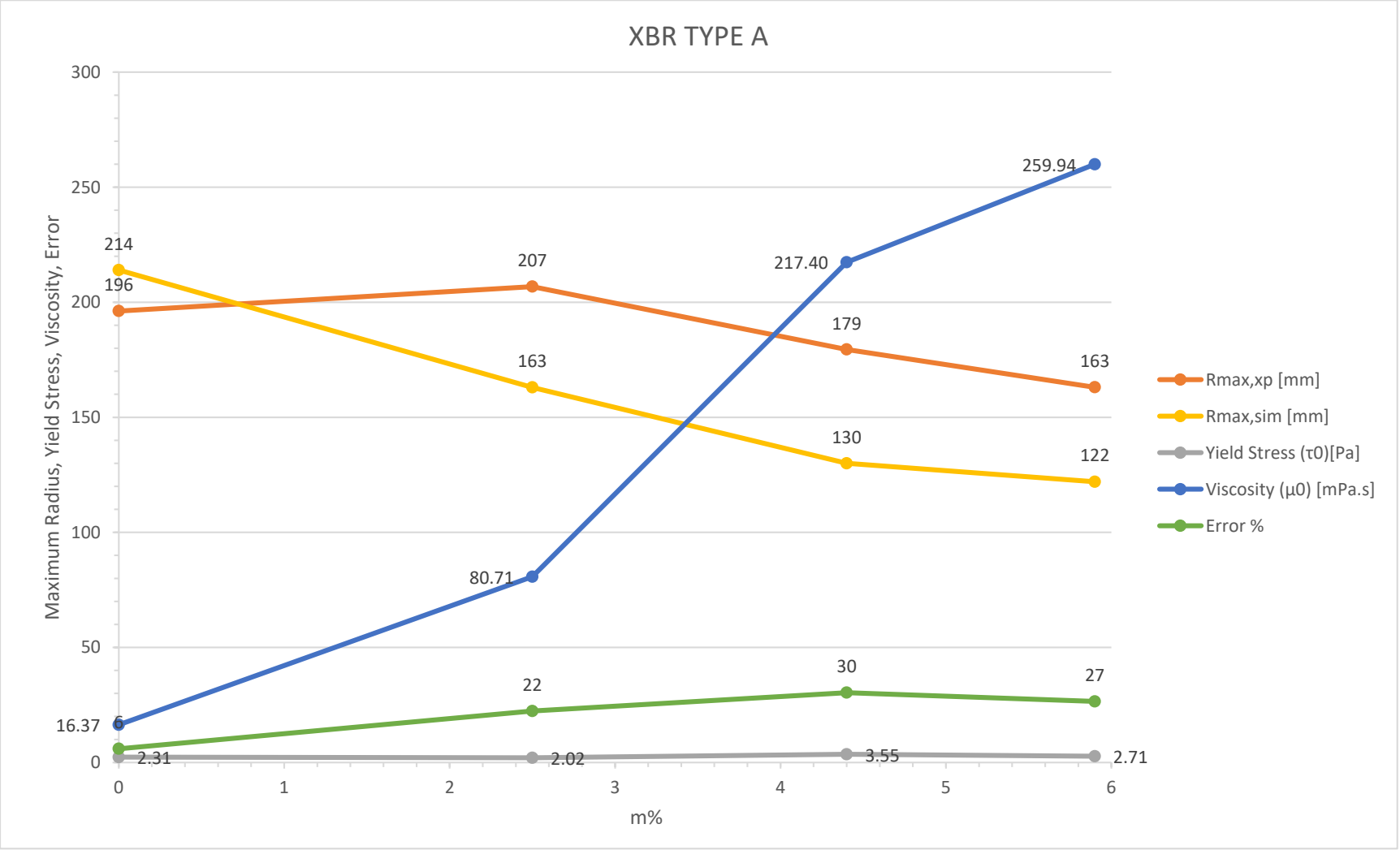

Figure 37. Summary XSBR Variation Type A. (Source: Own design)

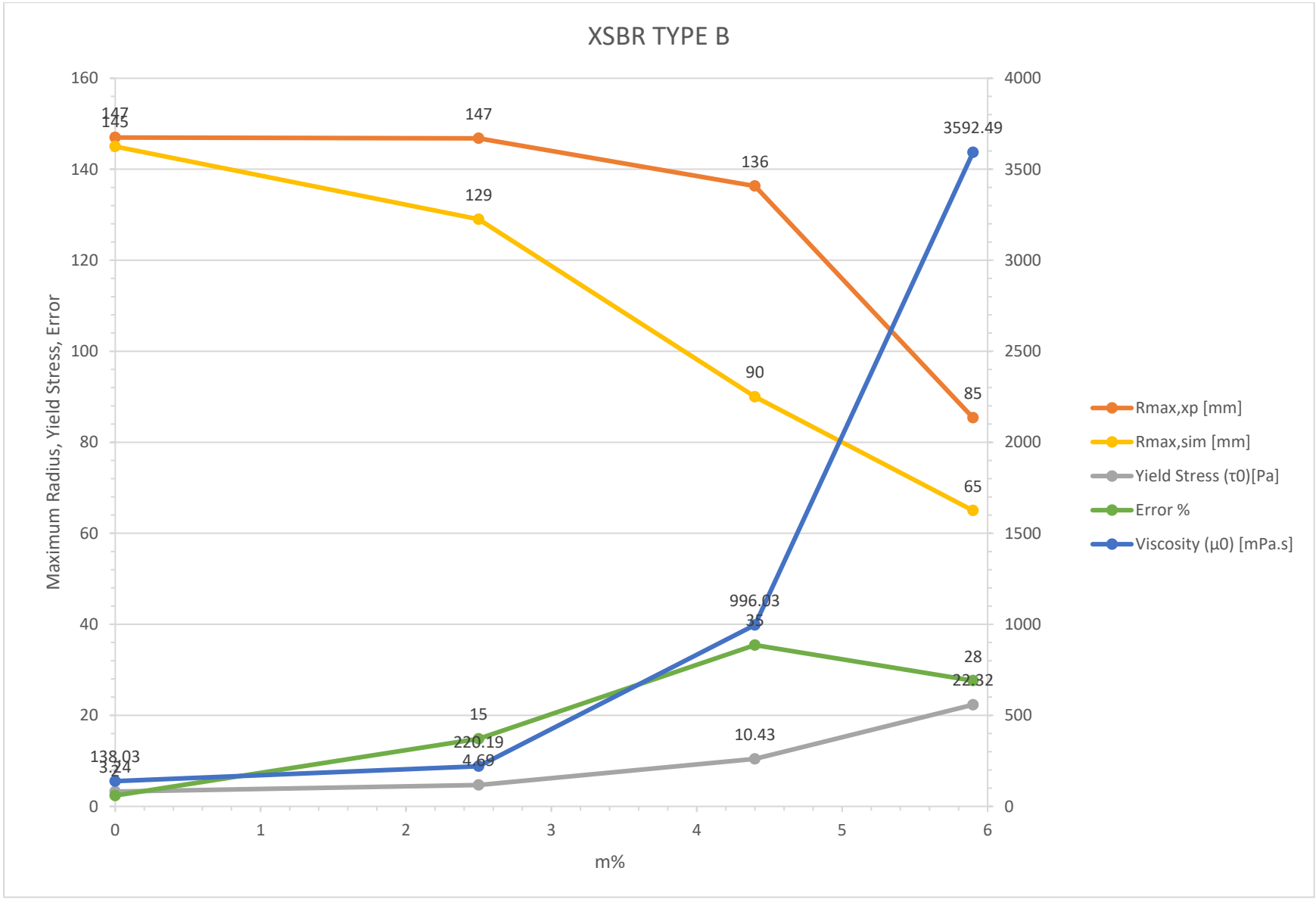

Figure 38. Summary XSBR Variation Type B. (Source: Own design)

P2.5X Cement Paste

The P2.5X behaviour is reported in the figure 39. The comparison between the yield stress of P0 and P2.5X, experimental data go down around 12% for types A and raises 45% for the type B. The common values of yield stress type A are between 1.79Pa to 2.36Pa whose average value is 2.02Pa. The type B yield stress is around 3.26Pa to 5.85Pa whose average is 4.69Pa.

Then, the other material property to analyse is the viscosity; it raises five times with respect to P0 for type A and 60% for type B. The range of data of type A is 78mPa.s to 82mPa.s whose average value is 80mPa.s. The type B has the range from 202mPa.s to 237mPa.s and the average value is 220mPas. This variation of yield stress and plastic viscosity, is due to the presence of XSBR in the cement paste.

Hence, in the type A, the viscosity increase, so this decrement of the yield stress governs the raise of the maximum experimental radius that goes from 196mm (P0) to 207mm (P2.5X). It means that the drop off the the yield stress is more influent than the raise of the viscosity, in the experimental radius. In the type B case, the maximum experimental radius for P0 is 147mm, and for P2.5X is the same 147mm. It means that, despite of the fact that the values of yield stress and plastic viscosity in the type B increases with respect to P0, the experimental radius are the same. It means that the experimental values are approximated. Running the code, it is seen that the maximum simulation radius for type A decreases from 214mm for P0 to 163mm for P2.5X. In this case, despite of the decrement is of yield stress with respect to P0, the increment of the plastic viscosity diminishes the simulation radius. The type B, the maximum simulation radius decreases from 145mm (P0) to 129mm(P2.5X). It is due to the raises of yield stress and plastic viscosity. Furthermore, the average error of the radius between experimental and simulation results are 22% for the type A and 15% for the type B.

Another changes produce in the radius-time experimental curves, the asymptotic behaviour starts at 40s (P2.5X) instead of 30s (P0) for case A and for case B, 35s (P2.5X) instead of 25s (P0). In summary, the type A, the decrement of yield stress, increase the time where the radius becomes constant. In another hand, the type B, the increment of yield stress raises the time where the experimental radius is constant.

As consequence, the shape of radius-time experimental curves is close than simulation curves but the experimental curves have higher values of radius than simulation curves. It is noticed that the lower values of experimental yield stress represent as a continues increasing of the radius-time curve. Finally, the simulation does not fit the experimental results with the simulation based in a Particle Finite Element code with a 0.0005s delta time computation.

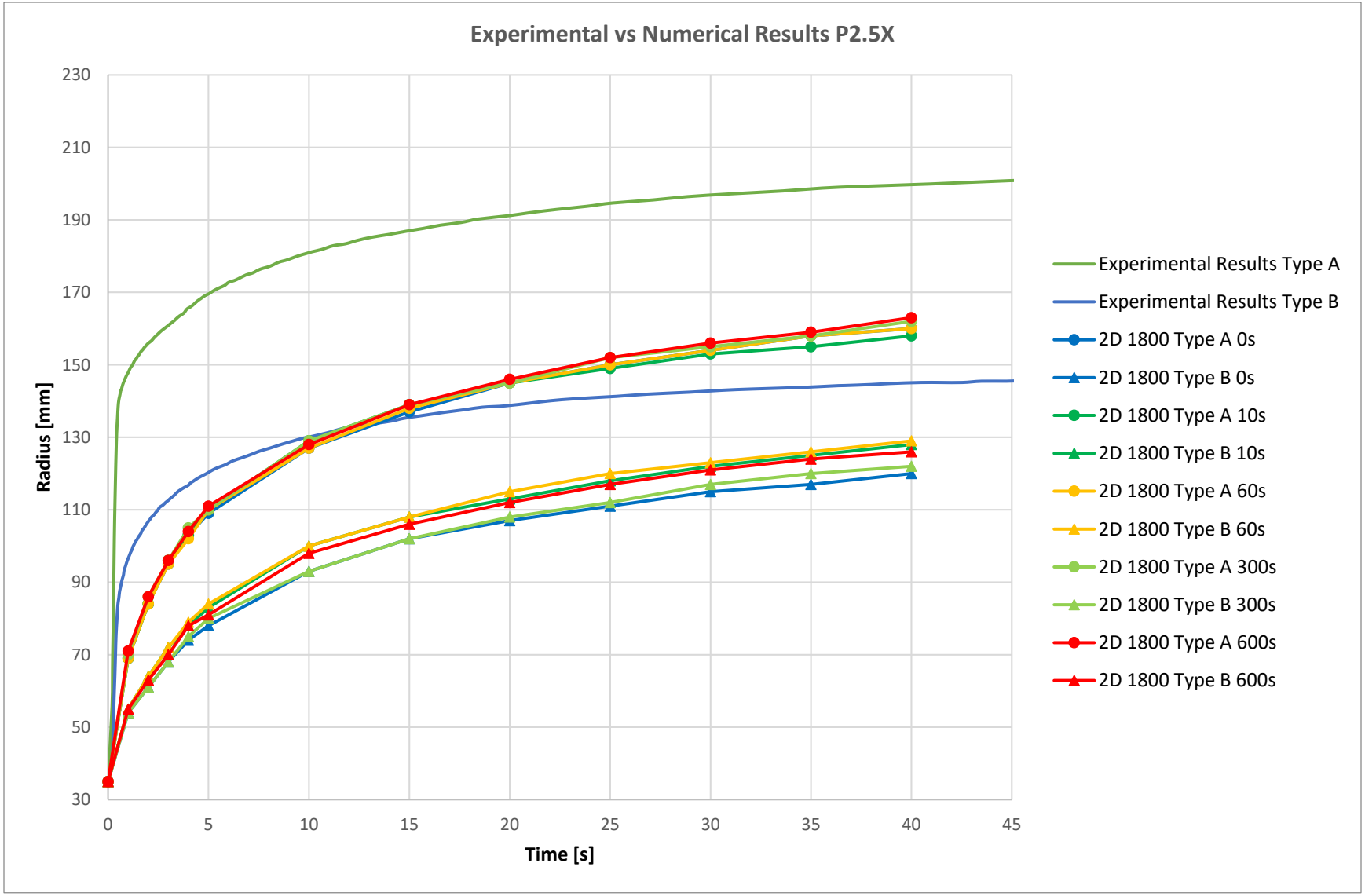

Figure 39. Experimental vs 2D Numerical Results P2.5X. (Source: Own design)

P4.4X Cement Paste

The figure 40 demonstrate the behaviour of P4.4X cement paste whose yield stress experimental data grow 76% in comparison to P2.5X for the type A. The range of values of yield stress type A is 2.98Pa to 4.64Pa whose average value is 3.55Pa. The type B yield stress twice the value, the range is between 9.09Pa to 12.7Pa and the average value is 10.43Pa. This variation happens due to the increment of XSBR.

This behaviour happens due to the variation of the viscosity where for type A is three times the value with respect to P2.5X. The P4.4X plastic viscosity values are between 195mPa.s to 243mPas and the average value is 217mPas. In the case of type B, the range of plastic viscosity values for P4.4X is 895mPas to 1063mPas and the average value 996mPas. It means that the P4.4X viscosity is five time more than P2.5X. This variation of yield stress and plastic viscosity, is due to the increment of XSBR in the cement paste.

As consequence, the maximum experimental radius drops off from 207mm(P2.5X) to 179mm (P4.4X) for type A and reduces the radius from 147mm(P2.5X) to 136mm(P4.4X) for type B. Then, the radius of experimental data decreases due to the increment of yield stress and plastic viscosity. After, running the code, the maximum simulation radius for type A decreases from 163mm (P2.5X) to 130mm (P4.4X). The type B, the maximum simulation radius decreases from 129mm (P2.5X) to 90mm(P4.4X). It happens due to the increment of yield stress and plastic viscosity. Moreover, the high average error of the maximum radius, which are 30% and 35% for type A and B respectively. It could be denoted that this cement paste is not well-represented.

The consequence of the increment of the yield stress is represented in the radius-time experimental curves where the constant radius starts, the time is 25s (P4.4X) instead of 40s (P2.5X) for the type A and the type B case, 40s (P4.4X) instead of 35s (P2.5X). To summarize, the type A, the increment of yield stress, decrease the time where the radius becomes constant. In another hand, the type B, the increment of yield stress raises the time where the experimental radius is constant.

The type A case simulates the same shape of experimental results but the higher values of viscosity in the type B, they show a change of shape in the simulation curves. Moreover, the radius-time simulation curves are lower than radius-time experimental curves. In summary, the Particle Finite Element code with a 0.0005s delta time computation does not provide an adequate simulation for this kind of cement paste.

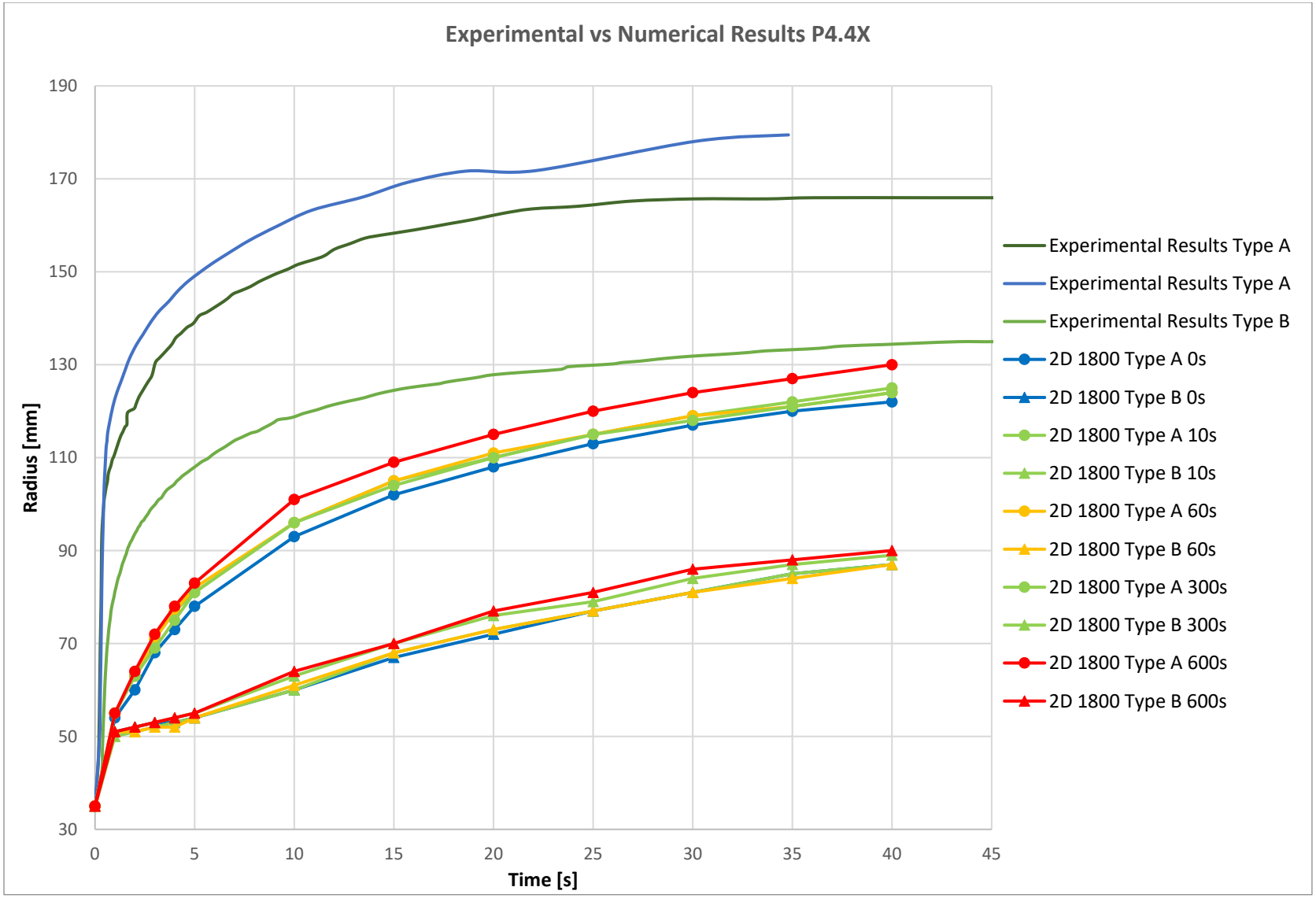

Figure 40. Experimental vs 2D Numerical Results P4.4X (Source: Own design)

P5.9X Cement Paste

The the behaviour of P5.9X cement paste is pictured in the figure 41. Comparing P4.4X and P5.9X, the yield stress decrease 24% for type A and grow twice the value for type B. The typical values of type A yield stress is 2.02Pa to 3.22Pa whose average value is 2.71Pa; the type B is 16.1Pa to 30.7Pa and the average value is 22Pa.

Then, the viscosity analysis; the type A raise 20% whose values are around 220mPa.s to 292mPa.s and the average value is 259mPa.s. The type B the viscosity jumps four times compared to P4.4X and the typical values are between 2988mPa.s to 4191mPa.s and the average value is 3592mPas. This variation of yield stress and plastic viscosity, is due to the increment of XSBR in the cement paste.

The maximum experimental radius decrements their values of the radius from 179mm (P4.4X) to 155mm (P5.9X) for type A. Despite of the decrement of yield stress, the radius decreases, so the increment of plastic viscosity influence in the maximum experimental radius. The type B case, the experimental radius is reduced from 136mm (P4.4X) to 85mm (P5.9X). Hence, the increment of yield stress and plastic viscosity diminishes the experimental radius. Then, running the numerical code, the values of simulation radius were obtained. The type A, the maximum simulation radius diminishes from 130mm (P4.4S) to 122mm (P5.9X). Despite of the decrement of yield stress type A, the radius decreases, so the increment of plastic viscosity diminishes the maximum simulation radius. The type B, goes from 90mm (P4.4X) to 65mm (P5.9X). Despite of the decrement of yield stress, the increment of plastic viscosity, slump the radius. Furthermore, the average error radius is 23% for type A and 28% for type B, which means that is not well-simulated by the code.

The results of this data is drawn in the radius-time experimental curves where the constant value of the radius type A starts at 35s (P5.9X) instead of 25s (P4.4X). Hence, the reduction of yield stress increases the time where the radius becomes. Then, the type B the tendency of a constant radius for P5.9X is 20s (P5.9X) and 40s (P4.4X). Hence, increment of viscosity decreases the time where the radius remains constant.

The case of type A curves, the shape is similar than experimental results but the simulation curves are still lower. The same analysis applies for the type B, but the shape of radius-time experimental curves does not match with the shape of the simulation curves due to the high values of viscosity. In summary the Particle Finite Element with a 0.0005s delta time computation is not recommendable to use to simulate this type of cement paste.

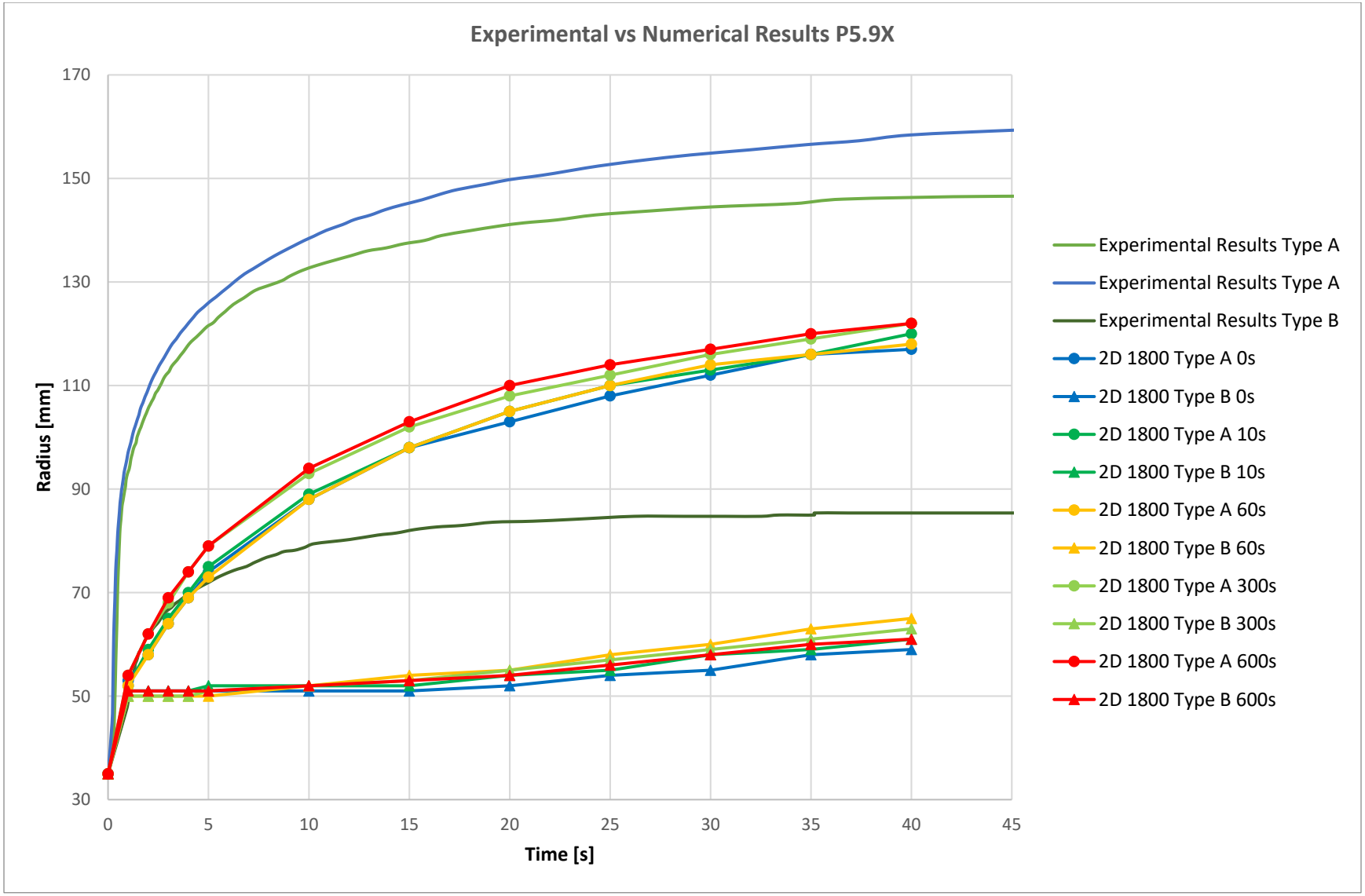

Figure 41. Experimental vs 2D Numerical Results P5.9X. (Source: Own design)

The figures 42 and 43 represent the summary of the variation of the Maximum experimental and simulation average radius, rest-time average yield Stress, rest-time average plastic viscosity, and average error, when the percentage of Wallastonite varies in the cement paste type A and B, which means that the reference paste is P0.

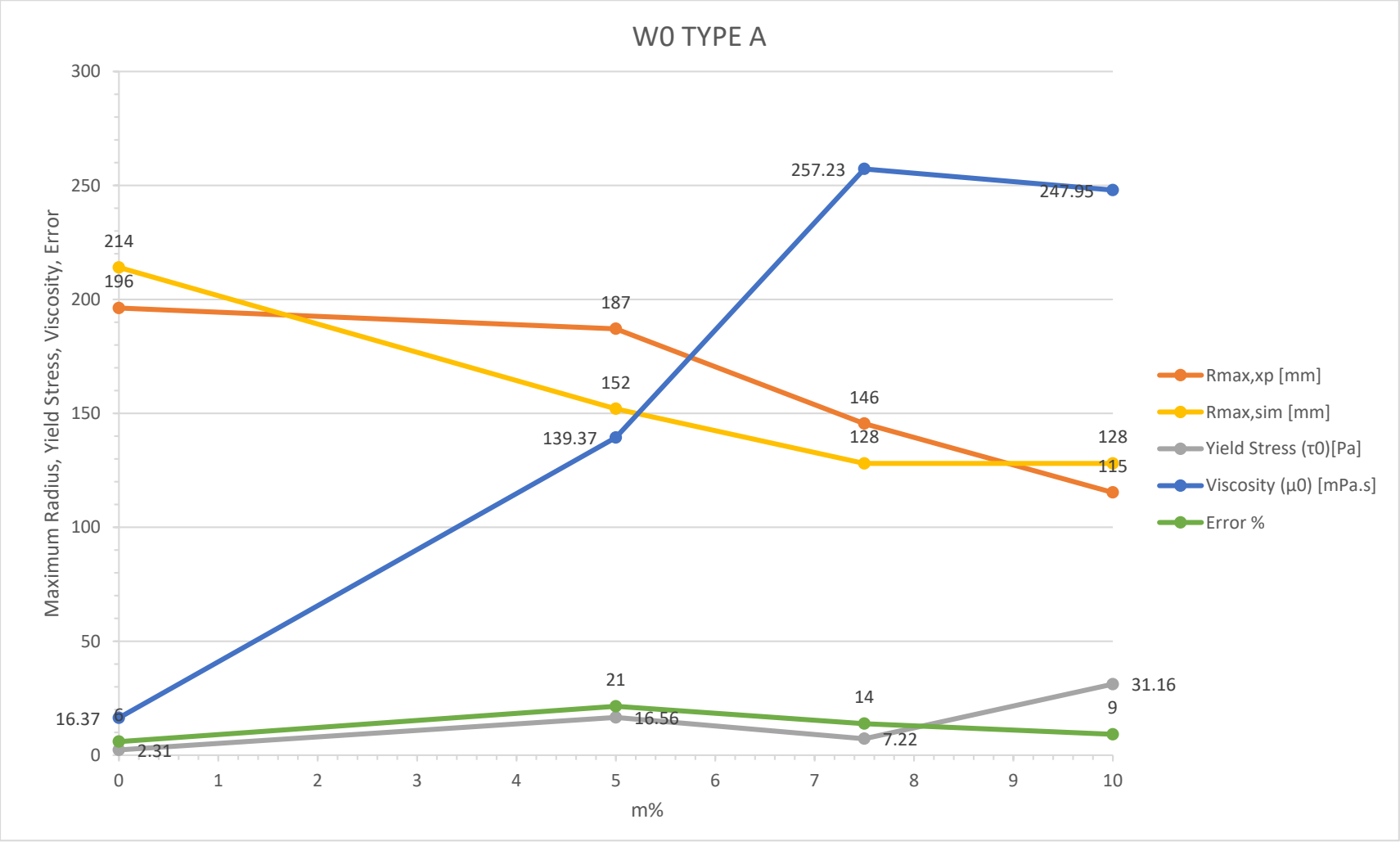

Figure 42. Summary Wallastonite Variation Type A. (Source: Own design)

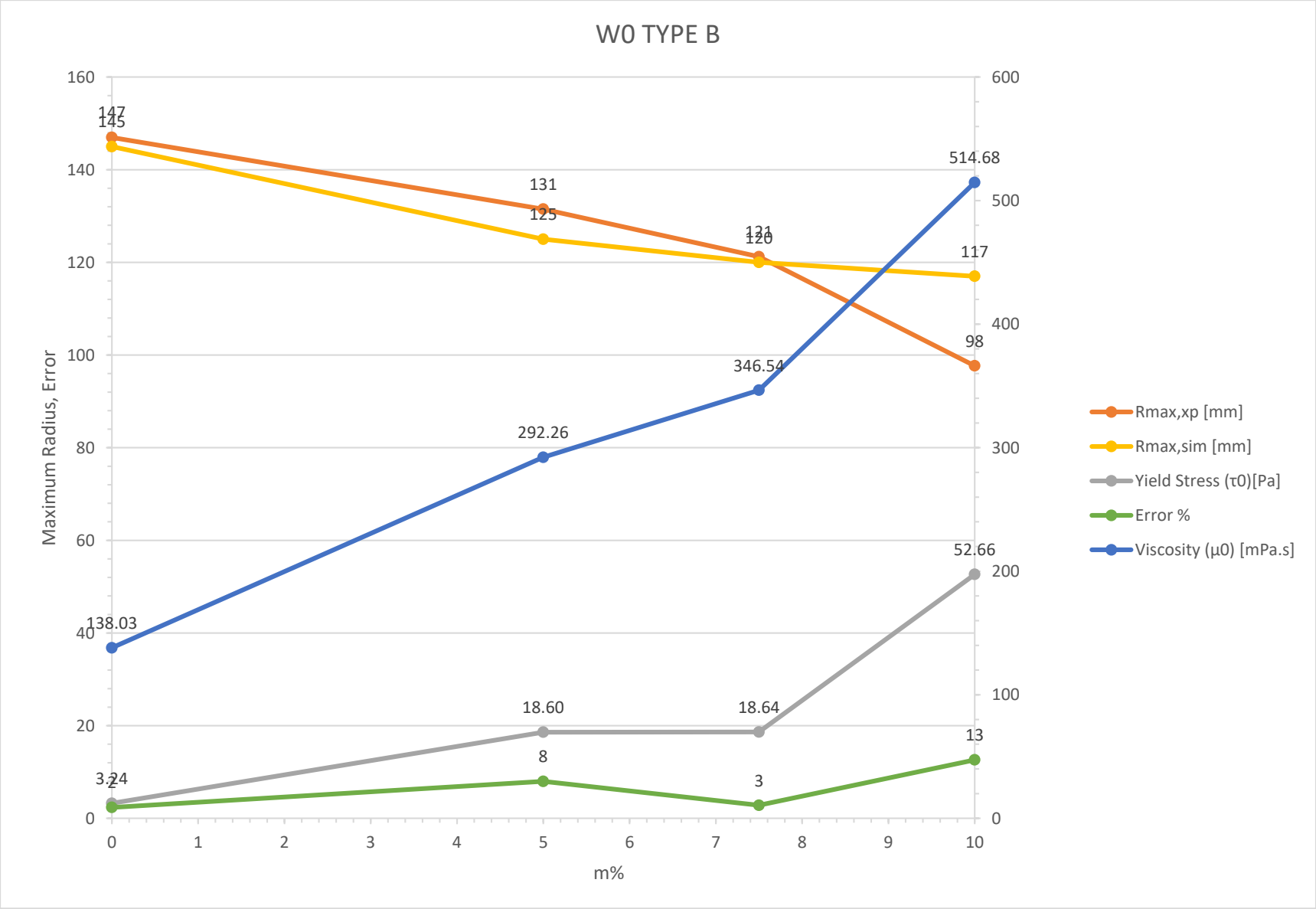

Figure 43. Summary Wallastonite Variation Type B. (Source: Own design)

WO5 Cement Paste

The WO5 cement paste behaviour is drawn in the figure 44. In this cement paste case, the yield stress is 7 times higher than P0; the range of values are around 10Pa to 24Pa for the type A. The average value is around 16Pa. Then, the yield stress is six times higher than P0, the typical values are around 15Pa to 23Pa for type B, and the average value is 18.6Pa.

Moreover, the viscosity for type A is nine time higher than P0, the viscosity is 118mPa.s to 156mPa.s whose average value is 139mPa.s. For the type B, the viscosity increases twice, the values are between 268mPa.s to 312mPa.s whose average value is 292mPa.s. This variation of yield stress and plastic viscosity, is due to the presence of Wallastonite in the cement paste.

The type A maximum experimental radius, decreases from 196mm (P5.9X) to 187mm(WO5). The type B, the radius of experimental results goes down from 147mm (P0) to 131mm (WO5). As consequence, the raise of the yield stress and viscosity diminishes the experimental radius of the cement paste. Running the numerical code, the values of simulation radius were obtained. The type A, the maximum simulation radius slumps from 214mm (P0) to 152mm (WO5). The type B, goes from 145mm (P0) to 125mm (WO5). The increment of yield stress and viscosity, decreases the simulation radius. Then, average error between experimental and simulation radius are 11% for type A and 8% for type B.

Hence, the asymptotic behaviour of the WO5 radius-time experimental curves starts at 20s (WO5) instead of 30S (P0) for the type A and 15s (WO5) instead of 25s (P0) for the type B. Hence, the increment of yield stress reduces the time where the radius becomes constant.

The simulation with a Lagrangian Finite Element code is approximated at the end part of the curves, in the type A. Due to the type B is more viscous than type A, the shape at the starting part of the experimental curves does not fit with the simulation curves but at the end tend to the convergence. It means that the code provides approximated response for this kind of cement paste. In conclusion this type of cement paste could be simulated by the Particle Finite Element with a 0.0005s delta time computation, considered as an approximate response.

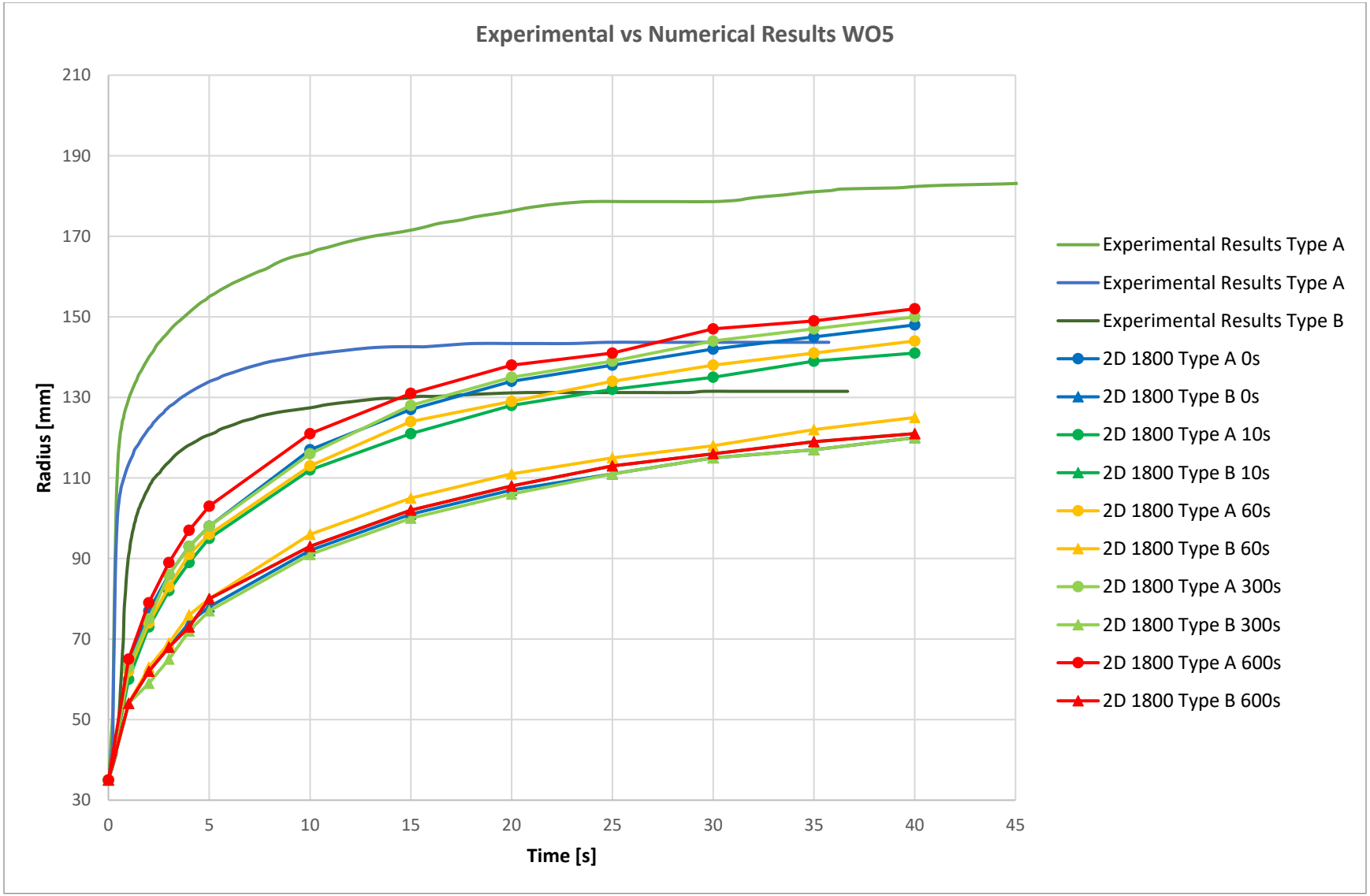

Figure 44. Experimental vs 2D Numerical Results WO5. (Source: Own design)

WO7.5 Cement Paste

The figure 45 represents the behaviour of WO7.5 cement paste. Comparing the yield stress value between WO5 and WO7.5 for type A, the second one decreases 56% compared to WO5. The range of values of type A yield stress is inside the values 5Pa to11Pa and me average value is 7Pa. Then, for type B, the yield stress does not change at all, the range of values is inside the range 16Pa to 22Pa and the average value is 18.64Pa.

In the type A, the viscosity grows up 85% with respect to the WO5 and the range of viscosity values is 249mPa.s to 265mPa.s and the average value is 257mPa.s. Next, the type B case, the viscosity increases 19% whose value range is between 330mPa.s to 358mPa.s and the average value is 346mPa.s. This variation of yield stress and plastic viscosity, is due to the increment of Wallastonite in the cement paste.

As consequence, the maximum experimental radius falls off from 187mm (WO5) to 146mm (WO7.5) in the type A. Despite of the decrement of yield stress, the raise of the viscosity diminishes the experimental radius. For the type B case, the radius-time experimental curves go down form 131mm (WO5) to 121mm(WO7.5). The increment of plastic viscosity, increases the experimental radius because the yield stress does not change with respect to WO5. Running the numerical code, the values of simulation radius were obtained. The type A, the maximum simulation radius slumps from 152mm (WO5) to 128mm (WO7.5). Despite of the decrement of type A yield stress, the radius decreases, so the increment of plastic viscosity diminishes simulation radius. Then, the type B, goes from 125mm (WO5) to 120mm (WO7.5). Despite of the yield stress does not change; the increment of plastic viscosity diminishes the simulation radius. Moreover, the average error of the experimental and simulation radius is 14% and 3% for type A and B, respectively.

Hence, the radius-time experimental curves type A tend to be constant at 15s (WO7.5) instead of 25s (WO5) cement paste. Despite of the yield stress decrement, the increment of plastic viscosity diminishes the time where the experimental radius is constant. The radius for the type B remain constant after 20s instead of 15s (WO5). The type B, the increment of yield stress raises the time where the radius becomes constant.

Then, the shape of the radius-time simulation curves does not match with WO7.5 experimental curve, but the curves of the type B at the end of the curve after 20s, they tend to converge. Due to the fact that the value of yield stress type B is almost the same compared to WO5 and only the viscosity increases, so the radius decreases; it means that the viscosity influences in the behaviour of the cement paste. As consequence, the Implementation of a Particle Finite Element code, with a 0.0005s delta time computation, for this cement paste is not recommended for yield stress and viscosity for type A but it is possible to simulate for type B, if these material properties are considered.

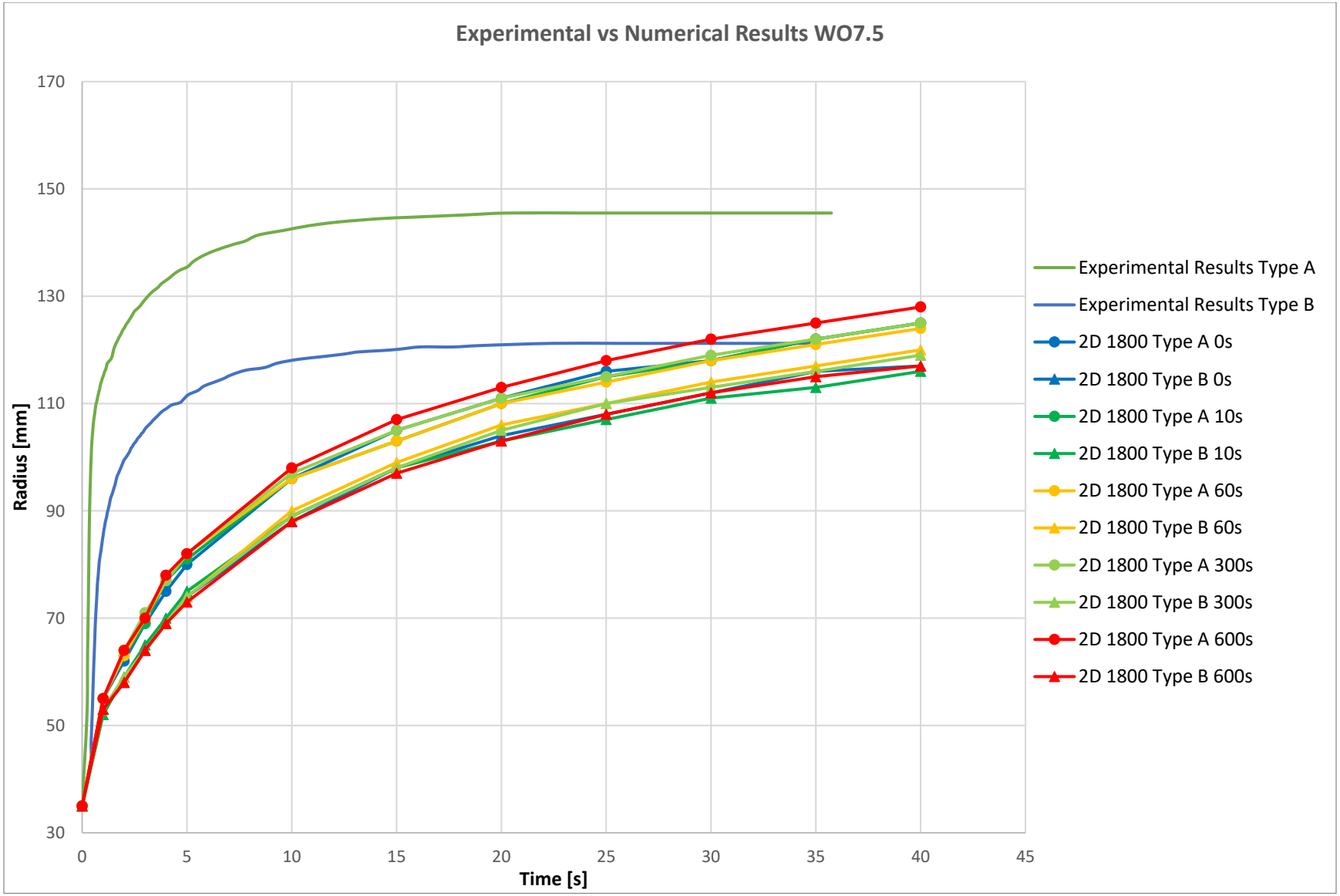

Figure 45. Experimental vs 2D Numerical Results WO7.5. (Source: Own design)

WO10 Cement Paste

The behaviour of WO10 cement paste is sketched in the figure 46. In this case, the yield stress is around 4 times higher than WO7.5 and the range of values are around 24Pa to 45Pa for the type A and the average value is 31Pa. Then the yield stress is 3 times higher than WO7.5, the typical values of WO10 type B are around 46Pa to 63Pa whose average value is 53Pa.

Related with the viscosity, the type A decrease around 4%. The values are between 236mPa.s to 258mPa.s, compared to WO7.5 whose average value is 247mPa.s, Then, the type B the viscosity increase 49% in contrast to WO7.5, the range of values are between 497mPa.s to 549mPa.s whose average value is 514mPa.s. The comparison of radius-time simulation curves of WO7.5 and WO10, the curves are similar, so the the variation of the yield stress does not change the behaviour in the simulation curves. This variation of yield stress and plastic viscosity, is due to the presence of Wallastonite in the cement paste.

Type A, experimental radius decrease from 146mm (WO7.5) to 115mm (WO10), it means that the large variation of the yield stress affects the experimental radius of the cement paste due to the viscosity decreases 4% only. The type B, the experimental radius diminishes from 121mm (WO7.5) to 98mm (WO10). Hence, the increment of yield stress and plastic viscosity decreases the experimental radius. Running the numerical code, the values of simulation radius were obtained. The type A, the maximum simulation radius is the same 128mm for W7.5 and WO10. Despite of the increment of type A yield stress, the simulation radius is the same, so the small decrement of plastic viscosity is most influent in the simulation curve. Then, the type B, goes from 120mm (W7.5) to 117mm (WO10). Hence, the increment of yield stress and plastic viscosity diminishes the simulation radius. Furthermore, the average error radius between experimental and simulation values are 11% for type A and 13% for type B; it means that this cement paste is approximated simulated by the code.

Hence, the curves tend to remain constant after 10s (WO10) for the case A instead of 15s (WO7.5) and 8s (WO10) instead of 20s(WO7.5) for the case B. As consequence, increment of yield stress decreases the time where the radius remains constant. Then, the radius-time simulation curves do not fit the experimental curves shape despite of they are inside the range after 20s.

The radius-time simulation curves are inside the range of the experimental curves after 20s but the shape of the curves is not the same. In summary, this kind of cement paste, it is possible to implement the Particle Finite Element Code with a 0.0005s delta time computation, taking into account that at first seconds the behaviour is not well-represented.

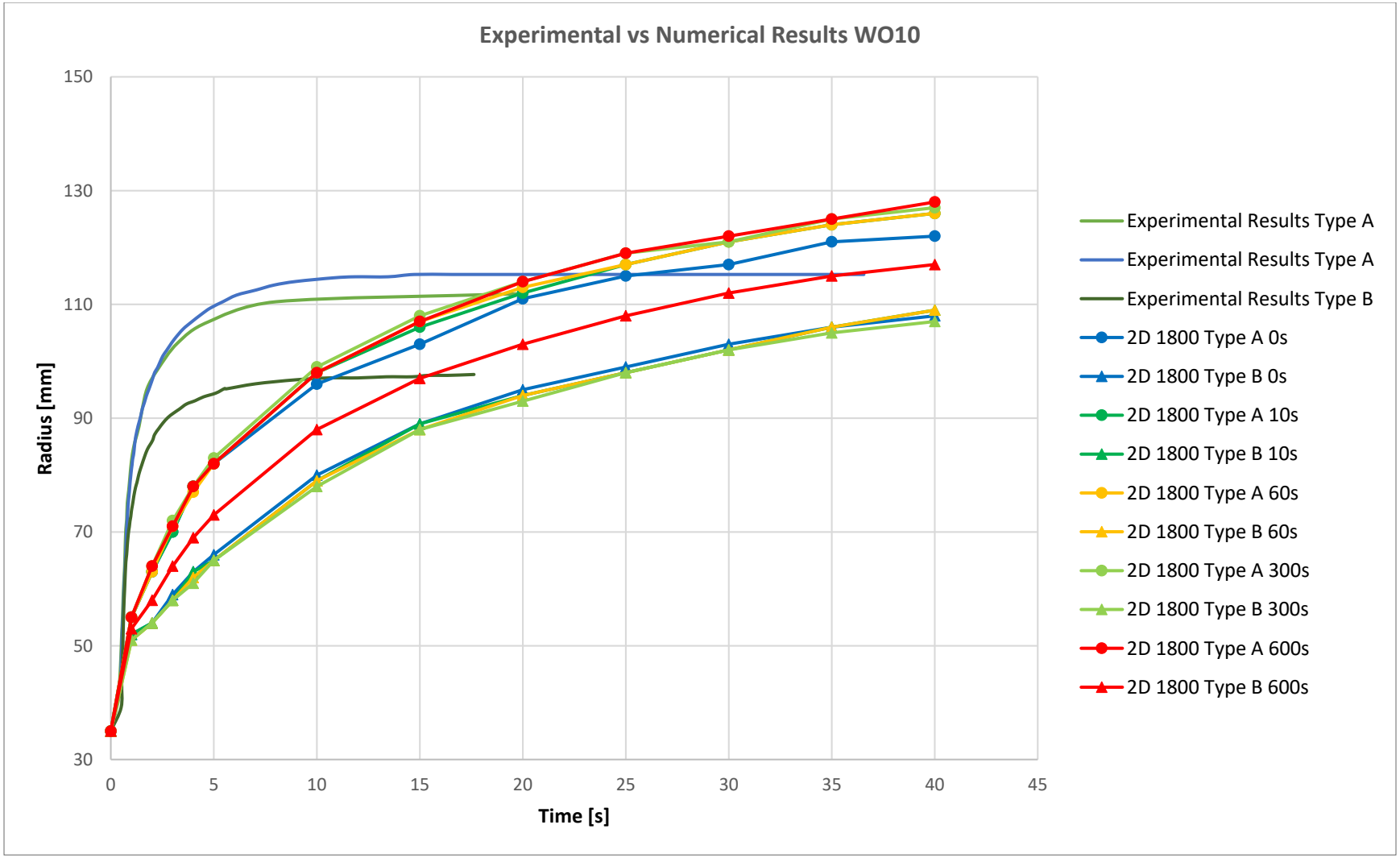

Figure 46. Experimental vs 2D Numerical Results WO10. (Source: Own design)

The figures 47 and 48 represent the summary of the variation of the Maximum experimental and simulation average radius, rest-time average yield Stress, rest-time average plastic viscosity, and average error, when the percentage of Wallastonite varies in the cement paste type A and B, which means that the reference paste is P0.

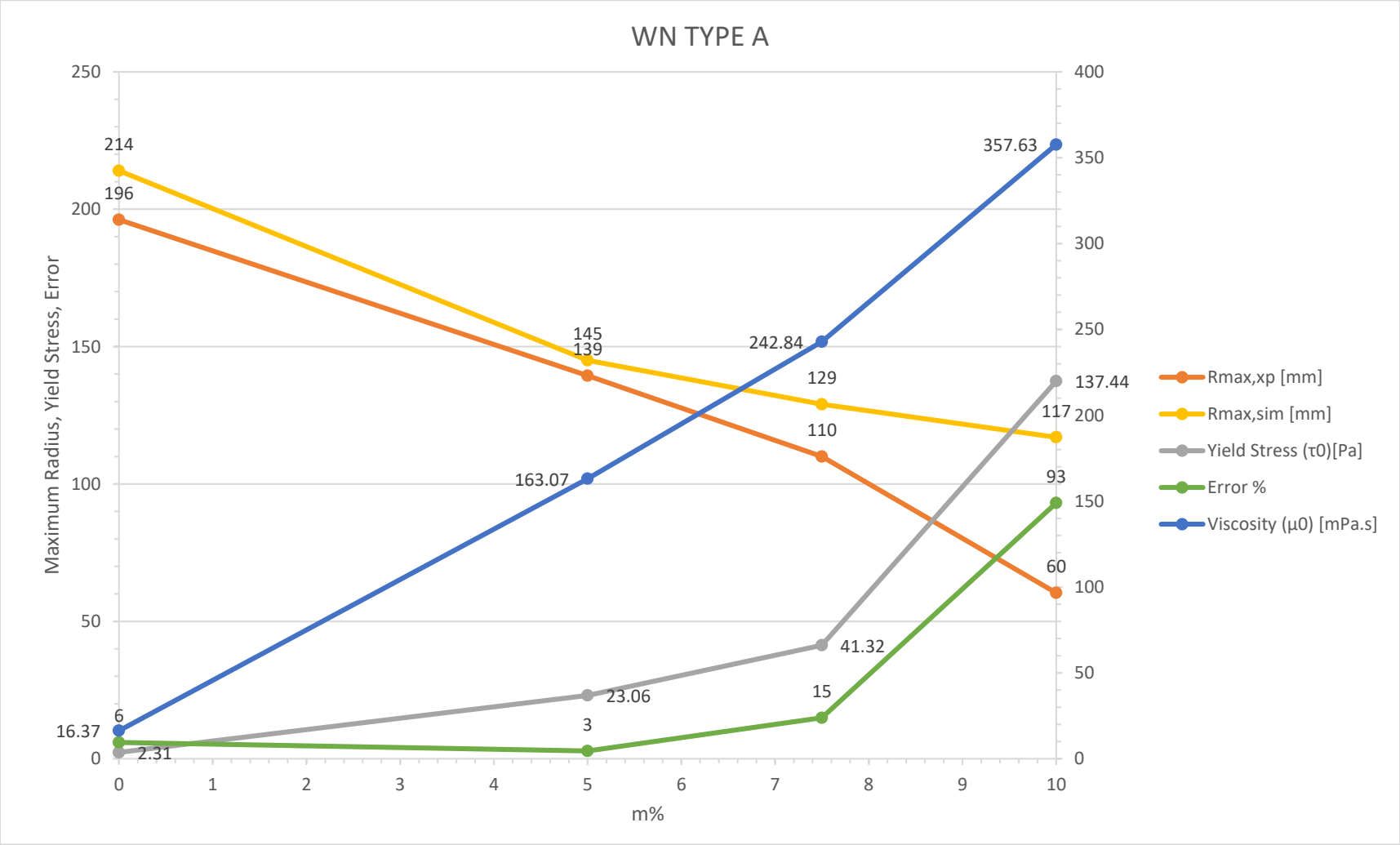

Figure 47. Summary Wallastonite Variation Type A. (Source: Own design)

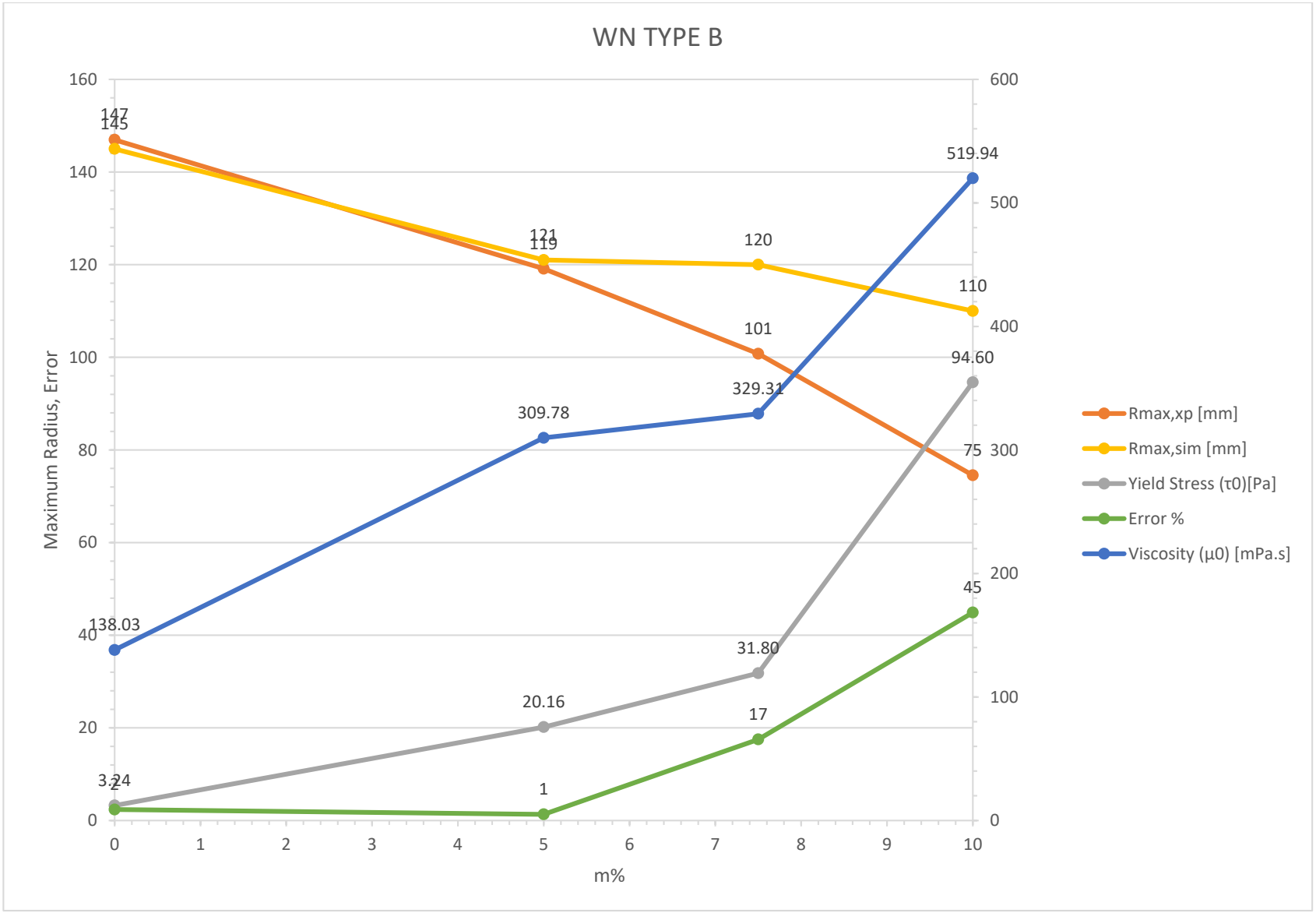

Figure 48. Summary Wallastonite Variation Type B. (Source: Own design)

WN5 Cement Paste

The figure 49 describes the behaviour of WN5 cement paste. The yield stress increases ten times compared to P0; the average value is around 23Pa and the range of values is around 16Pa to 36Pa, for the type A. The yield stress is six times higher than P0, the typical values type B are around 16Pa to 23Pa whose average value is 20Pa.

Related with the viscosity, the type A increase ten times compared to P0, the range of values is between 149mPa.s to 184mPa.s. whose average value is 163mPas. The type B, the value of viscosity increase six times, the values are between 302mPa.s to 327mPa.s whose average value is 309mPas. Hence, the large variation of the viscosity and yield stress affect the radius of the cement paste. This variation of yield stress and plastic viscosity, is due to the increment of Wallastonite in the cement paste.

The maximum experimental radius decrease from 196mm (P0) to 139mm (WN5), for type A. The type B the experimental radius diminishes from 147mm (P0) to 119mm. Hence, the increment of yield stress and plastic viscosity, slump the experimental radius. Running the numerical code, the values of simulation radius were obtained. The type A, the maximum simulation radius is 214mm (P0) and 152mm for (WN5) Then, the type B, goes from 145mm (P0) to 121mm (WN5). Hence, the increment of yield stress and plastic viscosity diminishes the simulation radius. Moreover, the average error radius between simulation and experimental results is small because the values are 3% for type A and 1% for type B.

Hence the curves tend to remain constant after 15s (WN5) for the case A instead of 30s for P0 cement paste. The case B, the radius is constant after 20s (WN5) instead of 25s for P0. It means that the yield stress goes down and the time where the radius remains constant. Hence, the radius-time simulation curves do not fit the experimental curves shape despite of they are inside the range after 20s.

Related to the type A case, the radius-time simulation curves are inside the range of the experimental curves after 25s but the shape of the curves does not coincide. The type B case, the radius-time simulation curves tend to converge after 25s but the path is not close to the experimental result. Moreover, the radius time simulation curves tend to the asymptotic behaviour after 40s.

In conclusion, this kind of cement paste, it is possible to implement the Particle Finite Element Code with a 0.0005s delta time computation, with the condition that at first seconds the behaviour is not well-represented.

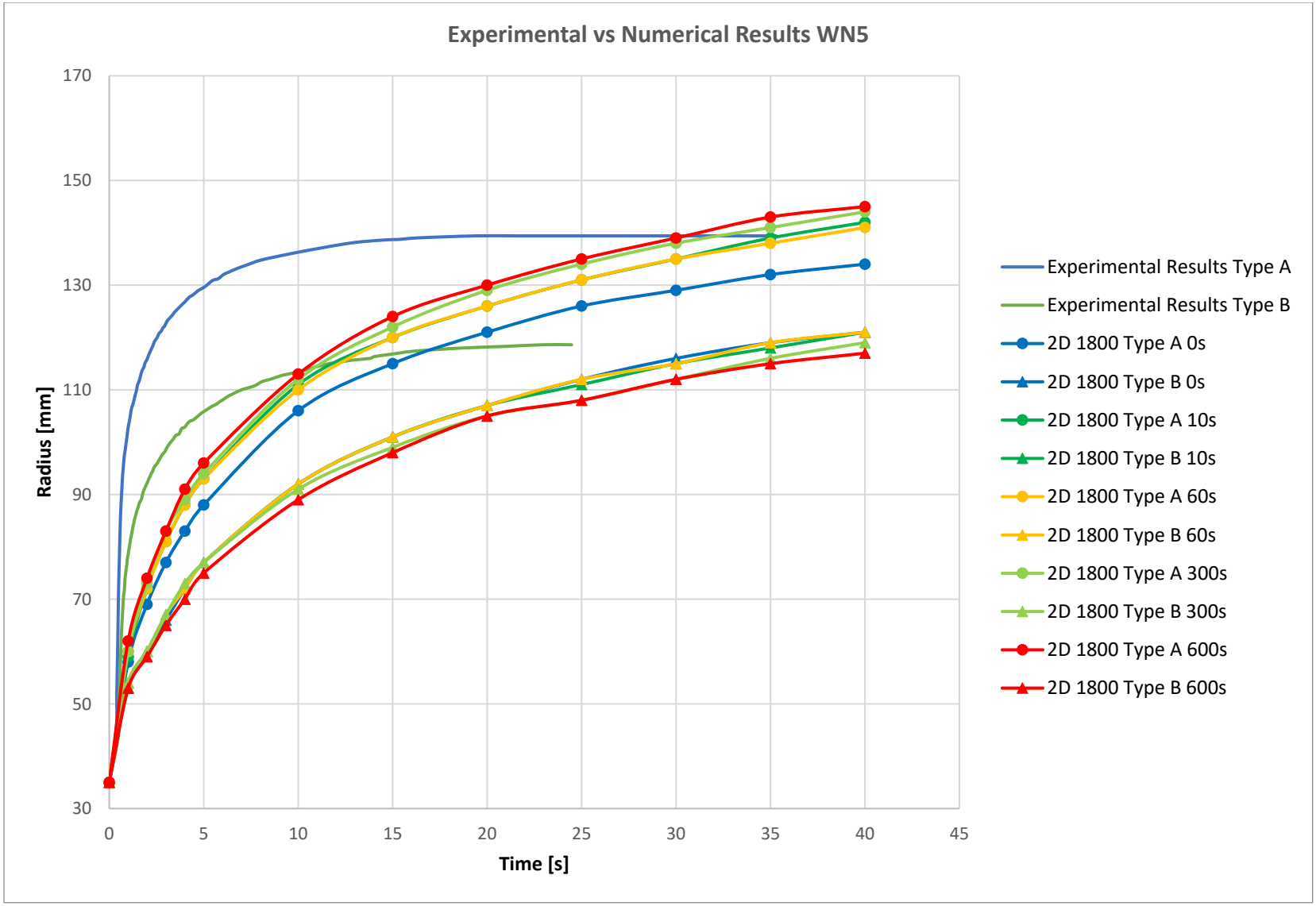

Figure 49. Experimental vs 2D Numerical Results WN5. (Source: Own design)

WN7.5 Cement Paste

The WN7.5 cement paste behaviour is associated with the figure 50. In reference to this case A, the yield stress increase 79% with respect to WN5 and the range of values are around 33Pa to 57Pa whose average value is 41Pa. The type B, the yield stress is 58% higher than WN5, the typical values of WN7.5 are around 27Pa to 39Pa whose average value is 31Pa

Then, the type A viscosity increase 49% compared to WN5, the values are between 236mPa.s to 253mPa.s and the average value of the viscosity is 242mPa.s. The type B, the viscosity increase 6% that differ from WN5 and the range of values are between 319mPa.s to 346mPa.s whose average value is 329mPa.s. This variation of yield stress and plastic viscosity, is due to the increment of Wallastonite in the cement paste.

Hence, the type A, the experimental radius decrease from 139mm (WN5) to 110mm (WN7.5). Type B, the radius decrease from 119mm (WN5) to 101mm (WN7.5). Hence, the increment of the yield stress and plastic viscosity diminishes the radius of the cement paste. Running the numerical code, the values of simulation radius were obtained. The type A, the maximum simulation radius is 145mm (WN5) and 129mm for (WN7.5). Then, the type B, goes from 121mm (WN5) to 120mm (WN7.5). Hence, the increment of yield stress and plastic viscosity diminishes the simulation radius. Then, the average error between simulation and experimental results are 20% and 17% for type A and B, respectively.

The result of the experimental data shows that the curves tend to remain constant after 10s (WN7.5) instead of 15s (WN5) in the case A and 10s(WN7.5) instead of 20s (WN5) for the case B. In summary, the increment of yield stress, decreases the time where the radius becomes constant. As consequence, the radius-time simulation curves do not fit the experimental curves shape. Then, the radius time simulation curves tend to the asymptotic behaviour after 40s.

The radius-time simulation curves are not inside the range of the experimental curves, and the shape of the curves is not the same. In summary, this kind of cement paste, it is not possible to be represented by the Particle Finite Element Code, with a 0.0005s delta time computation.

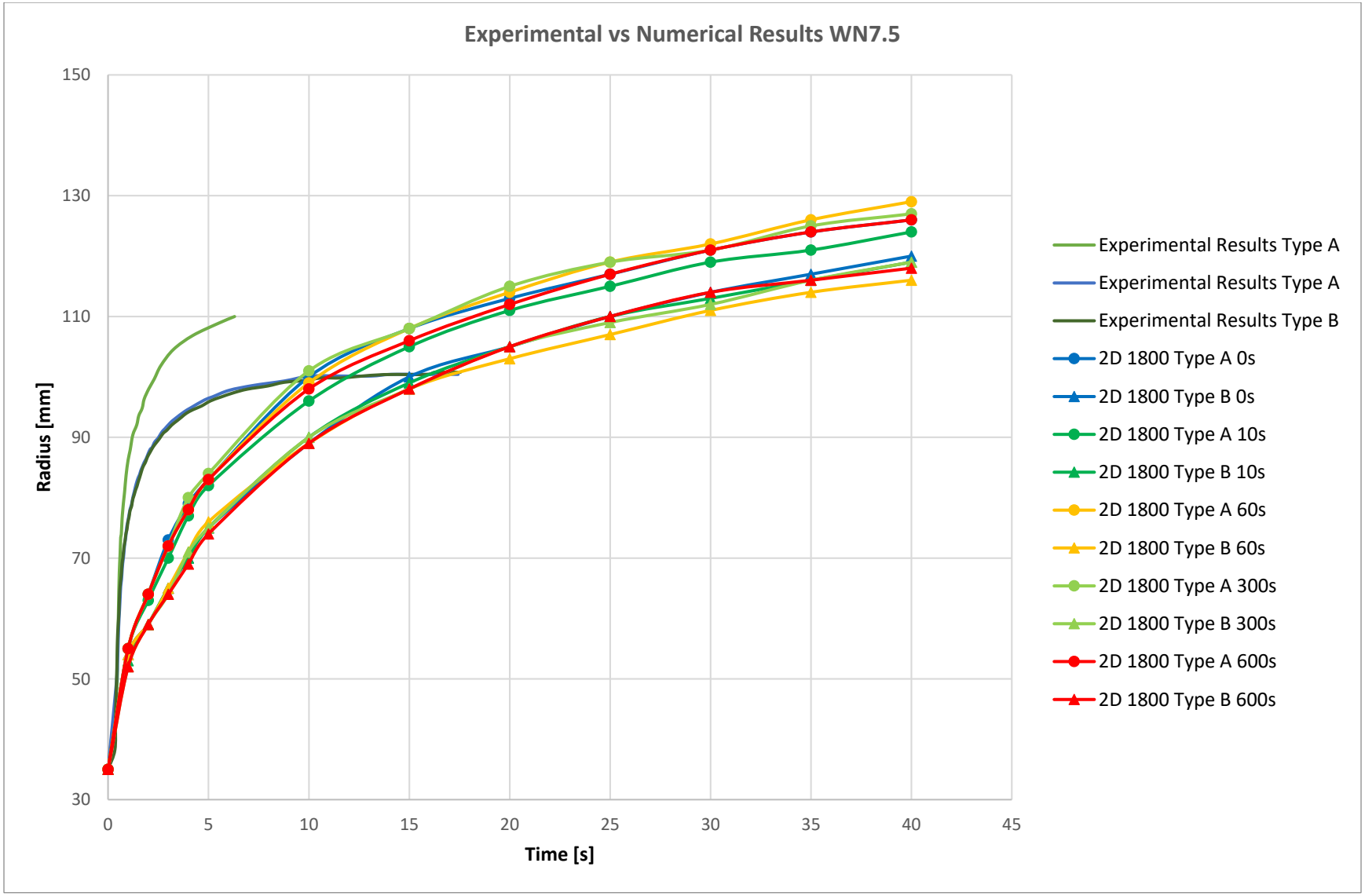

Figure 50. Experimental vs 2D Numerical Results WN7.5. (Source: Own design)

WN10 Cement Paste

The figure 51 represents the behaviour of WN10 cement paste. It is the last cement paste to be analysed whose yield stress increases more than 3 times compared to WN7.5; the average value is around 137Pa and the range of values is around 128Pa to 157Pa, for the type A. The yield stress is 3 times higher than WN7.5, the typical values are around 88Pa to 106Pa whose average value is 94.6Pa, for type B.

Related with the viscosity, the type A increase around 47% compared to WN7.5, The type B, the value of viscosity increase 58%. As consequence, the increment of the plastic viscosity and yield stress diminishes the radius of the cement paste. Doing the comparison of the data between WN7.5 and WN10, the values of the viscosity are between 316mPa.s to 376mPa.s whose average value is 357mPa.s, for type A. Type B, the viscosity values are between 473mPa.s to 616mPa.s whose average value is 519mPa.s. This variation of yield stress and plastic viscosity, is due to the increment of Wallastonite in the cement paste.

Hence, the experimental radius decrease from 110mm (WN7.5) to 60mm (WN10), for the type A. The type B case, the radius diminishes from 101mm (WN7.5) to 75mm (WN10). It means that the increment of yield stress and plastic viscosity influence decreases the experimental radius. Running the numerical code, the values of simulation radius were obtained. The type A, the maximum simulation radius is 129mm (WN7.5) and 117mm for (WN10). Then, the type B, goes from 120mm (WN7.5) to 110mm (WN10). Hence, the increment of yield stress and plastic viscosity diminishes the simulation radius. Furthermore, the average value between radius simulation and experimental results does not provide an adequate representation because the average errors are 93% for type A and 45% for type B.

Hence the curves tend to remain constant after 5s (WN10) instead of 10s (WN7.5), for the case A. The type B is the experimental radius is constant after 7s (WN10) instead of 10s (WN7.5) for the case B. In conclusion, the increment of yield stress diminishes the time where the experimental radius becomes constant. Hence, the radius-time simulation curves do not fit the experimental curves shape. Then, the radius time simulation curves tend to the asymptotic behaviour after 40s.

Related to the type A and B cases, the radius-time simulation curves are not inside the range of the experimental curves after 2s and the shape of the curves does not coincide. Finally, this kind of cement paste, it is not possible to simulate with the Particle Finite Element Code with a 0.0005s delta time computation because the behaviour is not well-represented.

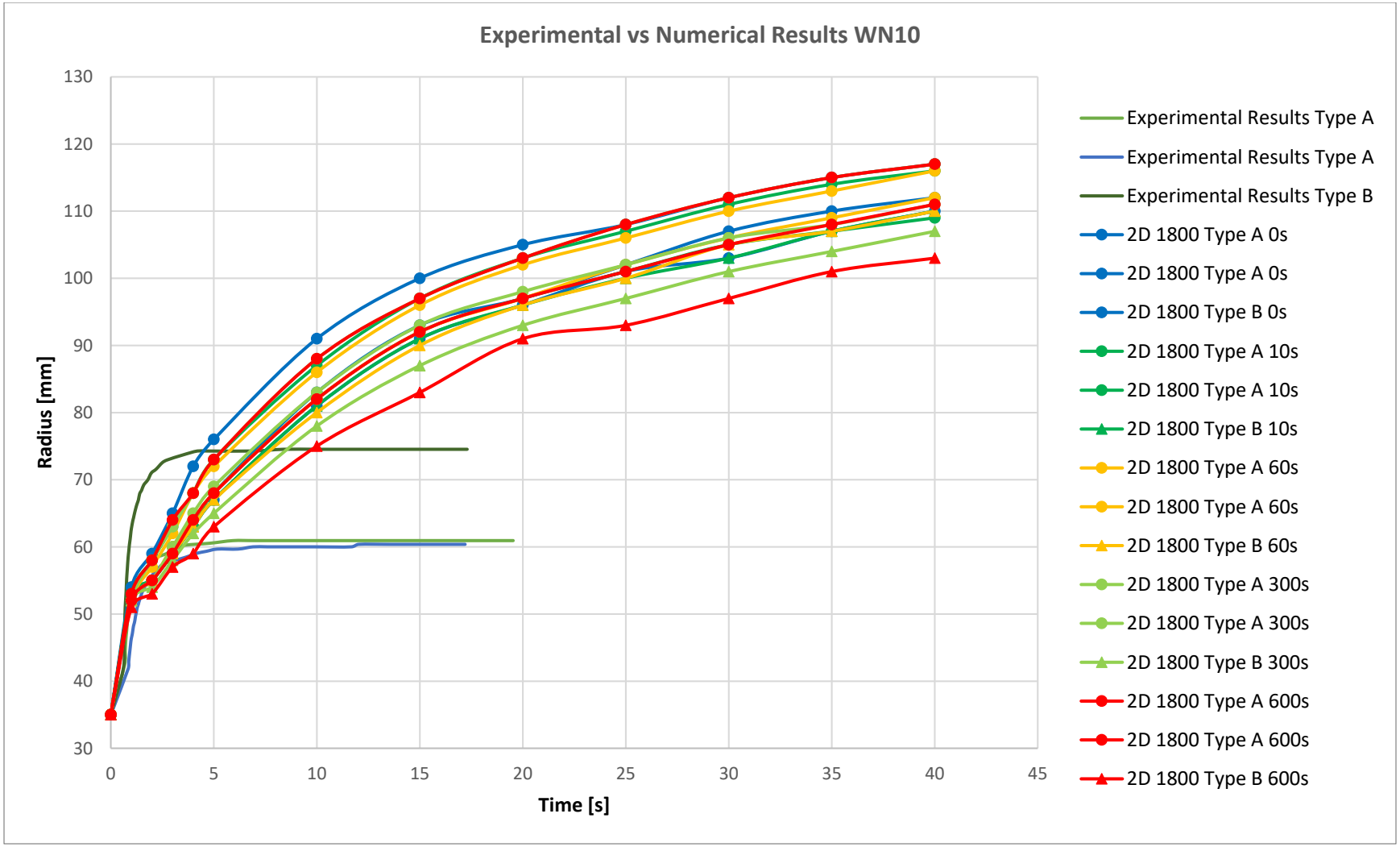

Figure 51. Experimental vs 2D Numerical Results WN10. (Source: Own design)

5

CONCLUSIONS

The tables 8 and 9 provides information about the error between maximum experimental radius and maximum simulation radius, using a 2D Particle Element Code. The type A case provides approximate response in the maximum radius for the following cement pastes, P0, P2.5S, WO10 and WN5, which are the cement pastes that contents lower quantity of polymer/fibres. Then, it is seen that the most accurate response is the type B because the cement pastes P0, W05, WO7.5 and WN5 have lower error values and these pastes have low polymer/fibres content. In conclusion, as more polymers/fibres were added, the code based in the Particle Finite Element with a delta time 0.0005s is not able to simulate appropriately this kind of cement pastes.

A particular case is P2.5S type B; Despite of the viscosity diminishes; the increment of the yield stress is more relevant in the mini-cone slump test than the simulation because the maximum experimental radius decreases and the maximum simulation radius increases. Other reason is possible mistake in the experimental data because the type A (P2.5S) viscosity increases and it is the only paste that its viscosity decreases when the polymer was incorporate in the mix design.

Starting from the reference paste P0, when the SBR, XSBR or wallastonite had been added, the yield stress and plastic viscosity increased for the cases type A, so the experimental radius slumps. The exception is P5.9S, the yield stress diminishes, so the experimental radius increases, but the maximum simulation radius diminishes, so the decrement of yield stress is less influent than the increment of viscosity in the simulation radius. Hence, the code is not able to simulate this behaviour.

In the P2.5X, the maximum experimental radius for type A increases due to the decrement of yield stress. In another hand, the decrement of yield stress with respect to P0, diminishes the simulation radius. As consequence, the increment of viscosity is relevant in the Particle Finite Element Code. The type B case, the maximum experimental radius is 147mm (P0) and, is the same 147mm (P2.5X). It means that, despite of the fact that the values of yield stress and plastic viscosity in the type B increases with respect to P0, the experimental radius are the same. It means that the provided experimental values are approximated.

The P5.9X cement past type A; Despite of the decrement of 24% in yield stress, the experimental radius decreases, so the increment of plastic viscosity influence in the maximum experimental radius. Even though the decrement of type A yield stress, the simulation radius decreases. Hence, the increment of plastic viscosity reduces the maximum simulation radius. In this kind of cement paste, the decrement of the radius happened for experimental and simulation results, despite of the fact that the yield stress diminishes.

A decrement of yield stress occurs in the WO7.5 cement paste. The raise of the viscosity, diminishes the experimental radius in the type A case. The same happens in the simulation radius. The type B case, the increment of plastic viscosity produces a decrement of the experimental radius because the yield stress does not change with respect to WO5. In summary, the decrement of the radius occurs for experimental and simulation results, despite of the fact that the yield stress diminishes or remains constant.

Three-dimensional numerical simulation demands more time-computation in order to obtain accurate results for the cementitious pastes. The exception is WN10, for which the numerical simulation curve is close to the experimental radius-time curves but its slope still keeps increasing.

The most accurate results are provided by the 2D numerical simulation due to the fact that the discretization sample has only 1800 finite elements, a number which is lower than the 9000 finite elements that the 3D model contains. In Figure 12, it is noted that the resulting curves are distant from experimental results. When the number of finite elements increased from 9000 to 20000 with the same delta time, the radius decrease due to the fact that the model is stiffer than the previous one, so the values provided by the code are lower bound with respect to the experimental results. As consequence, at lower delta time the 3D simulation curves tend to the experimental curves, so a high time-computation is required for a 3D simulation. In conclusion the 2D model provides information about cement paste behaviour in an adequate computation time.

Varying the value of the density is irrelevant for the output in the numerical simulation curves (see figure 26), as long as the variation was between 1.5 to 2.25dm^3. The densities in cementitious pastes are usually within this range of values.

6

BIBLIOGRAPHY

1. Ferrara L, Cremonesi M, Tregger N, Frangi A, Shah SP. On the identification of rheological properties of cement suspensions: Rheometry, computational fluid dynamics modeling and field test measurements. Cem Concr Res. 2012;42(8):1134-1146.

2. Ferrara L, Park Y, Shah SP. A method for mix-design of fiber-reinforced self-compacting concrete. Cem Concr Res. 2007;37(6):957-971.

3. Banfil P, Beaupré D, Chapdelaine F, Larrard Fd, Domone P. Comparison of concrete rheometers: International tests at LCPC. National Institute of Standards and Technology (USA) ed. Nantes, France: ; 2000.

4. Roussel N, Coussot P. "Fifty-cent rheometer" for yield stress measurements: For slump tospreding flow. Journal of Rheology. 2005;49:705-718.

5. Tregger N, Gregori A, Ferrara L, Shah S. Correlating dynamic segregation of self-consolidating concrete to the slump-flow test. Constr Build Mater. 2012;28(1):499-505.

6. Roussel N, Gram A, Cremonesi M, et al. Numerical simulations of concrete flow: A benchmark comparison. Cem Concr Res. 2016;79:265-271.

7. Cremonesi M, Frangi A, Perego U. A lagrangian finite element approach for the analysis of fluid–structure interaction problems. Int J Numer Methods Eng. 2010;84(5):610-630.

8. Zhu H, Martys NS, Ferraris C, Kee DD. A numerical study of the flow of Bingham-like fluids in two-dimensional vane and cylinder rheometers using a smoothed particle hydrodynamics (SPH) based method. J Non Newtonian Fluid Mech. 2010;165(7–8):362-375.

9. Roussel N, Geiker MR, Dufour F, Thrane LN, Szabo P. Computational modelling of concrete flow: General overview. Cem Concr Res. 2007;37(9):1298-1307.

10. Cremonesi M, Ferrara L, Frangi A, Perego U. Simulation of the flow of fresh cement suspensions by a lagrangian finite element approach. J Non Newtonian Fluid Mech. 2010;165(23–24):1555-1563.

11. Hirt CW, Nichols BD. Volume of fluid (VOF) method for the dynamics of free boundaries, Jornal of Computational Physics. 1981;39:201-225.

12. Dufour F, Pijaudier-Cabot G. Numerical modeling of concrete flow: Homogeneous approach, International Journal for Numerical and Analytical Methods in Goemechanics. 2005;29:395-416.

13. Vikhansky A. Lattice-Boltzmann method for yield-stress liquids. J Non Newtonian Fluid Mech. 2008;155(3):95-100.

14. Oñate E, Idelsohn SR, Del Pin F, Aubry R. The particle finite element method. an overview. International Journal of Computational Methods. 2004;1:267-307.

15. Idelsohn SR, Oñate E, Pin FD, Calvo N. Fluid–structure interaction using the particle finite element method. Comput Methods Appl Mech Eng. 2006;195(17–18):2100-2123.

16. Oñate E, Idelsohn SR, Celigueta MA, Rossi R. Advances in the particle finite element method for the analysis of fluid–multibody interaction and bed erosion in free surface flows. Comput Methods Appl Mech Eng. 2008;197(19–20):1777-1800.

17. Brezzi F. Mixed and hybrid finite element methods / franco brezzi, michel fortin. New York \etc.!: New York etc.] : Springer, copyr. 1991; 1991.

18. Tezduyar TE. Stabilized finite element formulation for incompressible flow computations. Advances in Applied Mechanics. 1992;28:1-44.

19. Tezduyar TE, Mittal S, Ray SE, Shih R. Incompressible flow computations with stabilized bilinear and linear equal-order-interpolation velocity-pressure elements. Computer Methods in Applied Mechanics and Engineering. 1992;95:221-242.

20. Tezduyar TE, Osawa Y. Finite element stabilization parameters computed from element matrices and vectors. Comput Methods Appl Mech Eng. 2000;190(3–4):411-430.

21. Roussel N, Le Roy R. The marsh cone: A test or a rheological apparatus Cem Concr Res. 2005;35(5):823-830.

22. Holcim Holcim getta nuove fondamenta per la Milano del futuro: Torre Libeskind a Citylife. Retrieved 30 November 2015 from http://www.holcim.it/stampa-e-media/comunicati-stampa-piu-recenti/latest-release/article/holcim-getta-nuove-fondamenta-per-la-milano-del-futuro-torre-libeskind-a-city.

23. WANG R, Effect of Styrene-Butadiene Rubber Latex on Mechanical Properties of Cementitious Materials Highlighted by Means of Nanoindentation.

24. MATHUR A, Influence of Wallastonite on Material Properies of Concrete, 2007, Central Road Research Intitute,1029.

25. STEPHEN Ranimol, Rheological behaviour of nanocomposites of natural rubber and carboxylated styrene butadiene rubber lattices and their blends, J Appl Polym Sci, 2006, 2355-2362.

26. De Campos Fabricio, Effects of Styrene-Butadiene Rubber Latex on the thixotropic behaviour of cement pastes for oil well cementing, Laboratory LabEST- Federal University of Rio de Janeiro, Rio de Janeiro-Brazil, 2016.

27. ACI Committee 238, Concrete Thixotropy, ACI 238.2T-14 Tech note, 2014.

7

ANNEX

2D 1800 Type A 0s Δt 0.0005		2D 1800 Type B 0s Δt 0.0005		2D 1800 Type A 10s Δt 0.0005		2D 1800 Type B 10s Δt 0.0005		2D 1800 Type A 60s Δt 0.0005	
Time, s	Radius, mm	Time, s	Radius, mm	Time,s	Radius, mm	Time,s	Radius, mm	Time,s	Radius, mm
0	35	0	35	0	35	0	35	0	35
1	116	1	118	1	114	1	60	1	114
2	135	2	138	2	135	2	73	2	135
3	147	3	151	3	146	3	82	3	146
4	156	4	161	4	155	4	88	4	155
5	163	5	168	5	161	5	93	5	161
10	184	10	187	10	182	10	111	10	182
15	194	15	201			15	121	15	193
20	203	20	209			20	128	20	202
25	209	25	226			25	133	25	208
30	213	30	231						
35	213								

Table 10. Output Measured Paraview P0. (Source: Own Design)

2D 1800 Type B 60s Δt 0.0005		2D 1800 Type A 300s Δt 0.0005		2D 1800 Type B 300s Δt 0.0005		2D 1800 Type A 600s Δt 0.0005		2D 1800 Type B 600s Δt 0.0005	
Time,s	Radius, mm	Time,s	Radius, mm	Time,s	Radius, mm	Time,s	Radius, mm	Time,s	Radius, mm
0	35	0	35	0	35	0	35	0	35
1	61	1	117	1	60	1	52	1	51
2	74	2	136	2	73	2	56	2	53
3	83	3	149	3	81	3	61	3	55
4	91	4	158	4	88	4	65	4	58
5	95	5	164	5	93	5	70	5	60
10	113	10	186	10	111	10	84	10	71
15	123	15	197	15	121	15	94	15	79
20	130	20	204	20	127	20	99		
25	135	25	210	25	132				
30	139			30	136				

Table 11. Output Measured Paraview P0. (Source: Own Design)

2D 1800 Type A 0s		2D 1800 TYPE B 0s		2D 1800 Type A 10s		2D 1800 TYPE B 10s		2D 1800 Type A 60s	
Time, s	Radius, mm	Time, s	Radius, mm	Time, s	Radius, mm	Time, s	Radius, mm	Time, s	Radius, mm
0	35	0	35	0	35	0	35	0	35
1	87	1	70	1	86	1	71	1	83
2	104	2	85	2	103	2	88	2	101
3	116	3	95	3	115	3	98	3	112
4	124	4	103	4	123	4	106	4	120
5	131	5	108	5	130	5	111	5	127
10	151	10	127	10	150	10	129	10	146
15	163	15	139	15	160	15	139	15	157
20	169	20	145	20	168	20	145	20	164
25	174	25	150	25	173	25	150	25	170
30	179	30	154	30	177	30	154	30	175
35	181	35	158	35	180	35	158	35	178
40	183	40	160	40	183	40	159	40	181

Table 12. Output Measured Paraview P2.5S. (Source: Own Design)

2D 1800 TYPE B 60s		2D 1800 Type A 300s		2D 1800 TYPE B 300s		2D 1800 Type A 600s		2D 1800 TYPE B 600s	
Time, s	**Radius, mm**	**Time, s**	**Radius, mm**	**Time, s**	**Radius, mm**	**Time, s**	**Radius, mm**	**Time, s**	**Radius, mm**
0	35	0	35	0	35	0	35	0	35
1	68	1	87	1	67	1	84	1	67
2	83	2	106	2	82	2	102	2	82
3	92	3	117	3	92	3	113	3	91
4	101	4	126	4	100	4	121	4	98
5	106	5	132	5	106	5	127	5	105
10	125	10	153	10	122	10	146	10	123
15	135	15	163	15	132	15	158	15	134
20	143	20	169	20	139	20	164	20	141
25	148	25	176	25	144	25	169	25	146
30	152	30	180	30	148	30	174	30	150
35	155	35	183	35	151	35	178	35	154
40	158	40	186	40	154	40	181	40	157

Table 13. Output Measured Paraview P2.5S. (Source: Own Design)

2D 1800 Type A 0s		2D 1800 Type B 0s		2D 1800 Type A 10s		2D 1800 Type B 10s		2D 1800 Type A 60s	
Time, s	**Radius, mm**	**Time, s**	**Radius, mm**	**Time, s**	**Radius, mm**	**Time, s**	**Radius, mm**	**Time, s**	**Radius, mm**
0	35	0	35	0	35	0	35	0	35
1	92	1	59	1	78	1	62	1	74
2	110	2	71	2	96	2	74	2	91
3	122	3	78	3	107	3	84	3	102
4	130	4	86	4	115	4	91	4	110
5	136	5	89	5	120	5	96	5	116
10	156	10	107	10	140	10	114	10	135
15	168	15	116	15	150	15	124	15	145
20	174	20	122	20	158	20	130	20	152
25	179	25	127	25	163	25	134	25	157
30	183	30	131	30	167	30	138	30	160
35	187	35	133	35	170	35	141	35	164
40	188	40	136	40	172	40	144	40	167

Table 14. Output Measured Paraview P4.4S. (Source: Own Design)

2D 1800 TYPE B 60s		2D 1800 Type A 300s		2D 1800 TYPE B 300s		2D 1800 Type A 600s		2D 1800 TYPE B 600s	
Time, s	Radius, mm	Time, s	Radius, mm	Time, s	Radius, mm	Time, s	Radius, mm	Time, s	Radius, mm
0	35	0	35	0	35	0	35	0	35
1	60	1	73	1	58	1	76	1	58
2	72	2	88	2	69	2	93	2	68
3	80	3	98	3	78	3	105	3	77
4	87	4	107	4	85	4	112	4	83
5	92	5	112	5	90	5	119	5	88
10	110	10	131	10	106	10	137	10	105
15	119	15	141	15	115	15	147	15	114
20	125	20	148	20	121	20	155	20	120
25	129	25	153	25	125	25	160	25	125
30	132	30	157	30	128	30	164	30	129
35	136	35	160	35	130	35	168	35	131
40	139	40	163	40	133	40	170	40	133

Table 15. Output Measured Paraview P4.4S. (Source: Own Design)

2D 1800 Type A 0s		2D 1800 Type B 0s		2D 1800 Type A 10s		2D 1800 Type B 10s		2D 1800 Type A 60s	
Time, s	Radius, mm	Time, s	Radius, mm	Time, s	Radius, mm	Time, s	Radius, mm	Time, s	Radius, mm
0	35	0	35	0	35	0	35	0	35
1	75	1	58	1	78	1	58	1	78
2	92	2	68	2	95	2	68	2	94
3	102	3	76	3	105	3	77	3	105
4	110	4	83	4	113	4	83	4	113
5	116	5	88	5	119	5	88	5	119
10	133	10	105	10	138	10	105	10	139
15	144	15	113	15	148	15	114	15	148
20	151	20	120	20	155	20	120	20	155

Table 16. Output Measured Paraview P5.9S. (Source: Own Design)

2D 1800 TYPE B 60s		2D 1800 Type A 600s		2D 1800 TYPE B 600s	
Time, s	Radius, mm	Time, s	Radius, mm	Time, s	Radius, mm
0	35	0	35	0	35
1	57	1	78	1	59
2	68	2	95	2	70
3	76	3	105	3	81
4	83	4	112	4	87
5	88	5	118	5	92
10	105	10	138	10	108
15	114	15	148	15	118
20	120	20	154	20	125

Table 17. Output Measured Paraview P5.9S. (Source: Own Design)

2D 1800 Type A 0s		2D 1800 Type B 0s		2D 1800 Type A 10s		2D 1800 Type B 10s		2D 1800 Type A 60s	
Time, s	Radius, mm	Time, s	Radius, mm	Time, s	Radius, mm	Time, s	Radius, mm	Time, s	Radius, mm
0	35	0	35	0	35	0	35	0	35
1	69	1	54	1	69	1	55	1	69
2	84	2	61	2	84	2	64	2	84
3	95	3	68	3	96	3	72	3	95
4	103	4	74	4	103	4	78	4	102
5	109	5	78	5	110	5	83	5	110
10	127	10	93	10	129	10	100	10	127
15	137	15	102	15	139	15	108	15	138
20	145	20	107	20	145	20	113	20	145
25	150	25	111	25	149	25	118	25	150
30	154	30	115	30	153	30	122	30	154
35	158	35	117	35	155	35	125	35	158
40	160	40	120	40	158	40	128	40	160

Table 18. Output Measured Paraview P2.5X. (Source: Own Design)

2D 1800 Type B 60s		2D 1800 Type A 600s		2D 1800 Type B 600s	
Time, s	Radius, mm	Time, s	Radius, mm	Time, s	Radius, mm
0	35	0	35	0	35
1	55	1	71	1	55
2	64	2	86	2	63
3	72	3	96	3	70
4	79	4	104	4	78
5	84	5	111	5	81
10	100	10	128	10	98
15	108	15	139	15	106
20	115	20	146	20	112
25	120	25	152	25	117
30	123	30	156	30	121
35	126	35	159	35	124
40	129	40	163	40	126

Table 19. Output Measured Paraview P2.5X. (Source: Own Design)

2D 1800 Type A 0s		2D 1800 Type B 0s		2D 1800 Type A 10s		2D 1800 Type B 10s		2D 1800 Type A 60s	
Time, s	Radius, mm	Time, s	Radius, mm	Time, s	Radius, mm	Time, s	Radius, mm	Time, s	Radius, mm
0	35	0	35	0	35	0	35	0	35
1	54	1	51	1	55	1	50	1	55
2	60	2	52	2	63	2	51	2	63
3	68	3	53	3	71	3	52	3	71
4	73	4	53	4	77	4	53	4	77
5	78	5	54	5	81	5	54	5	82
10	93	10	60	10	96	10	60	10	96
15	102	15	67	15	105	15	68	15	105
20	108	20	72	20	110	20	73	20	111
25	113	25	77	25	115	25	77	25	115
30	117	30	81	30	119	30	81	30	119
35	120	35	85	35	122	35	85	35	121
40	122	40	87	40	125	40	87	40	124

Table 20. Output Measured Paraview P4.4X (Source: Own Design)

2D 1800 Type B 60s		2D 1800 Type A 600s		2D 1800 Type B 600s	
Time, s	Radius, mm	Time, s	Radius, mm	Time, s	Radius, mm
0	35	0	35	0	35
1	51	1	55	1	51
2	51	2	64	2	52
3	52	3	72	3	53
4	52	4	78	4	54
5	54	5	83	5	55
10	61	10	101	10	64
15	68	15	109	15	70
20	73	20	115	20	77
25	77	25	120	25	81
30	81	30	124	30	86
35	84	35	127	35	88
40	87	40	130	40	90

Table 21. Output Measured Paraview P4.4X (Source: Own Design)

2D 1800 Type A 0s		2D 1800 Type B 0s		2D 1800 Type A 10s		2D 1800 Type B 10s		2D 1800 Type A 60s	
Time, s	Radius, mm	Time, s	Radius, mm	Time, s	Radius, mm	Time, s	Radius, mm	Time, s	Radius, mm
0	35	0	35	0	35	0	35	0	35
1	53	1	51	1	52	1	51	1	52
2	58	2	51	2	59	2	51	2	58
3	64	3	51	3	65	3	51	3	64
4	69	4	51	4	70	4	51	4	69
5	74	5	51	5	75	5	52	5	73
10	88	10	51	10	89	10	52	10	88
15	98	15	51	15	98	15	52	15	98
20	103	20	52	20	105	20	54	20	105
25	108	25	54	25	110	25	55	25	110
30	112	30	55	30	113	30	58	30	114
35	116	35	58	35	116	35	59	35	116
40	117	40	59	40	120	40	61	40	118

Table 22. Output Measured Paraview P5.9X. (Source: Own Design)

2D 1800 Type B 60s		2D 1800 Type A 600s		2D 1800 Type B 600s	
Time, s	Radius, mm	Time, s	Radius, mm	Time, s	Radius, mm
0	35	0	35	0	35
1	50	1	54	1	51
2	50	2	62	2	51
3	50	3	69	3	51
4	50	4	74	4	51
5	50	5	79	5	51
10	52	10	94	10	52
15	54	15	103	15	53
20	55	20	110	20	54
25	58	25	114	25	56
30	60	30	117	30	58
35	63	35	120	35	60
40	65	40	122	40	61

Table 23. Output Measured Paraview P5.9X. (Source: Own Design)

2D 1800 Type A 0s		2D 1800 Type B 0s		2D 1800 Type A 10s		2D 1800 Type B 10s		2D 1800 Type A 60s	
Time, s	Radius, mm	Time, s	Radius, mm	Time, s	Radius, mm	Time, s	Radius, mm	Time, s	Radius, mm
0	35	0	35	0	35	0	35	0	35
1	63	1	54	1	60	1	54	1	62
2	77	2	62	2	73	2	62	2	74
3	86	3	68	3	82	3	68	3	83
4	93	4	74	4	89	4	73	4	91
5	98	5	78	5	95	5	80	5	96
10	117	10	92	10	112	10	93	10	113
15	127	15	101	15	121	15	102	15	124
20	134	20	107	20	128	20	108	20	129
25	138	25	111	25	132	25	113	25	134
30	142	30	115	30	135	30	116	30	138
35	145	35	117	35	139	35	119	35	141
40	148	40	120	40	141	40	121	40	144

Table 24. Output Measured Paraview WO5. (Source: Own Design)

2D 1800 Type B 60s		2D 1800 Type A 600s		2D 1800 Type B 600s	
Time, s	Radius, mm	Time, s	Radius, mm	Time, s	Radius, mm
0	35	0	35	0	35
1	54	1	65	1	54
2	63	2	79	2	60
3	69	3	89	3	67
4	76	4	97	4	72
5	80	5	103	5	77
10	96	10	121	10	91
15	105	15	131	15	100
20	111	20	138	20	105
25	115	25	141	25	110
30	118	30	147	30	113
35	122	35	149	35	116
40	125	40	152	40	119

Table 25. Output Measured Paraview WO5. (Source: Own Design)

2D 1800 Type A 0s		2D 1800 Type B 0s		2D 1800 Type A 10s		2D 1800 Type B 10s		2D 1800 Type A 60s	
Time, s	Radius, mm	Time, s	Radius, mm	Time, s	Radius, mm	Time, s	Radius, mm	Time, s	Radius, mm
0	35	0	35	0	35	0	35	0	35
1	55	1	53	1	55	1	52	1	55
2	62	2	58	2	63	2	59	2	63
3	69	3	64	3	69	3	65	3	70
4	75	4	69	4	77	4	70	4	77
5	80	5	74	5	81	5	75	5	82
10	96	10	88	10	96	10	89	10	96
15	105	15	98	15	103	15	98	15	103
20	111	20	104	20	110	20	103	20	110
25	116	25	108	25	115	25	107	25	114
30	118	30	112	30	118	30	111	30	118
35	122	35	116	35	122	35	113	35	121
40	125	40	117	40	125	40	116	40	124

Table 26. Output Measured Paraview WO7.5. (Source: Own Design)

2D 1800 Type B 60s		2D 1800 Type A 600s		2D 1800 Type B 600s	
Time, s	Radius, mm	Time, s	Radius, mm	Time, s	Radius, mm
0	35	0	35	0	35
1	53	1	55	1	53
2	59	2	64	2	58
3	64	3	70	3	64
4	69	4	78	4	69
5	74	5	82	5	73
10	90	10	98	10	88
15	99	15	107	15	97
20	106	20	113	20	103
25	110	25	118	25	108
30	114	30	122	30	112
35	117	35	125	35	115
40	120	40	128	40	117

Table 27. Output Measured Paraview WO7.5. (Source: Own Design)

2D 1800 Type A 0s		2D 1800 Type B 0s		2D 1800 Type A 10s		2D 1800 Type B 10s		2D 1800 Type A 60s	
Time, s	Radius, mm	Time, s	Radius, mm	Time, s	Radius, mm	Time, s	Radius, mm	Time, s	Radius, mm
0	35	0	35	0	35	0	35	0	35
1	55	1	52	1	55	1	52	1	55
2	63	2	54	2	63	2	54	2	63
3	70	3	59	3	70	3	58	3	71
4	78	4	63	4	78	4	63	4	77
5	82	5	66	5	82	5	65	5	82
10	96	10	80	10	98	10	79	10	98
15	103	15	89	15	106	15	89	15	107
20	111	20	95	20	112	20	94	20	113
25	115	25	99	25	117	25	98	25	117
30	117	30	103	30	121	30	102	30	121
35	121	35	106	35	124	35	106	35	124
40	122	40	108	40	126	40	109	40	126

Table 28. Output Measured Paraview WO10. (Source: Own Design)

2D 1800 Type B 60s		2D 1800 Type A 600s		2D 1800 Type B 600s	
Time, s	Radius, mm	Time, s	Radius, mm	Time, s	Radius, mm
0	35	0	35	0	35
1	51	1	55	1	53
2	54	2	64	2	58
3	58	3	71	3	64
4	62	4	78	4	69
5	65	5	82	5	73
10	79	10	98	10	88
15	88	15	107	15	97
20	94	20	114	20	103
25	98	25	119	25	108
30	102	30	122	30	112
35	106	35	125	35	115
40	109	40	128	40	117

Table 29. Output Measured Paraview WO10. (Source: Own Design)

2D 1800 Type A 0s		2D 1800 Type B 0s		2D 1800 Type A 10s		2D 1800 Type B 10s		2D 1800 Type A 60s	
Time, s	Radius, mm	Time, s	Radius, mm	Time, s	Radius, mm	Time, s	Radius, mm	Time, s	Radius, mm
0	35	0	35	0	35	0	35	0	35
1	58	1	54	1	59	1	53	1	60
2	69	2	60	2	72	2	60	2	72
3	77	3	66	3	81	3	67	3	81
4	83	4	72	4	88	4	72	4	88
5	88	5	77	5	93	5	77	5	93
10	106	10	92	10	111	10	92	10	110
15	115	15	101	15	120	15	101	15	120
20	121	20	107	20	126	20	107	20	126
25	126	25	112	25	131	25	111	25	131
30	129	30	116	30	135	30	115	30	135
35	132	35	119	35	139	35	118	35	138
40	134	40	121	40	142	40	121	40	141

Table 30. Output Measured Paraview WN5. (Source: Own Design)

2D 1800 Type B 60s		2D 1800 Type A 600s		2D 1800 Type B 600s	
Time, s	Radius, mm	Time, s	Radius, mm	Time, s	Radius, mm
0	35	0	35	0	35
1	54	1	62	1	53
2	60	2	74	2	59
3	67	3	83	3	65
4	72	4	91	4	70
5	77	5	96	5	75
10	92	10	113	10	89
15	101	15	124	15	98
20	107	20	130	20	105
25	112	25	135	25	108
30	115	30	139	30	112
35	119	35	143	35	115
40	121	40	145	40	117

Table 31. Output Measured Paraview WN5. (Source: Own Design)

2D 1800 Type A 0s		2D 1800 Type B 0s		2D 1800 Type A 10s		2D 1800 Type B 10s		2D 1800 Type A 60s	
Time, s	Radius, mm	Time, s	Radius, mm	Time, s	Radius, mm	Time, s	Radius, mm	Time, s	Radius, mm
0	35	0	35	0	35	0	35	0	35
1	55	1	54	1	55	1	53	1	55
2	64	2	59	2	63	2	59	2	64
3	73	3	65	3	70	3	65	3	72
4	79	4	70	4	77	4	70	4	78
5	83	5	75	5	82	5	75	5	83
10	100	10	89	10	96	10	90	10	99
15	108	15	100	15	105	15	99	15	108
20	113	20	105	20	111	20	105	20	114
25	117	25	110	25	115	25	110	25	119
30	121	30	114	30	119	30	113	30	122
35	124	35	117	35	121	35	116	35	126
40	126	40	120	40	124	40	119	40	129

Table 32. Output Measured Paraview WN7.5. (Source: Own Design)

2D 1800 Type B 60s		2D 1800 Type A 600s		2D 1800 Type B 600s	
Time, s	Radius, mm	Time, s	Radius, mm	Time, s	Radius, mm
0	35	0	35	0	35
1	54	1	55	1	52
2	59	2	64	2	59
3	65	3	72	3	64
4	71	4	78	4	69
5	76	5	83	5	74
10	89	10	98	10	89
15	98	15	106	15	98
20	103	20	112	20	105
25	107	25	117	25	110
30	111	30	121	30	114
35	114	35	124	35	116
40	116	40	126	40	118

Table 33. Output Measured Paraview WN7.5. (Source: Own Design)

2D 1800 Type A 0s		2D 1800 Type A 0s		2D 1800 Type B 0s		2D 1800 Type A 10s		2D 1800 Type A 10s		2D 1800 Type B 10s	
Time, s	Radius, mm	Time, s	Radius, mm	Time, s	Radius, mm	Time, s	Radius, mm	Time, s	Radius, mm	Time, s	Radius, mm
0	35	0	35	0	35	0	35	0	35	0	35
1	54	1	53	1	52	1	53	1	52	1	53
2	59	2	55	2	55	2	58	2	55	2	55
3	65	3	60	3	59	3	63	3	59	3	59
4	72	4	64	4	63	4	68	4	63	4	63
5	76	5	68	5	67	5	73	5	68	5	67
10	91	10	83	10	81	10	87	10	82	10	81
15	100	15	93	15	91	15	97	15	92	15	91
20	105	20	97	20	96	20	103	20	97	20	96
25	108	25	102	25	101	25	107	25	101	25	100
30	112	30	107	30	103	30	111	30	105	30	103
35	115	35	110	35	107	35	114	35	107	35	107
40	117	40	112	40	110	40	116	40	109	40	110

Table 34. Output Measured Paraview WN10. (Source: Own Design)

2D 1800 Type A 60s		2D 1800 Type A 60s		2D 1800 Type B 60s		2D 1800 Type A 600s		2D 1800 Type A 600s		2D 1800 Type B 600s	
Time, s	**Radius, mm**	**Time, s**	**Radius, mm**	**Time, s**	**Radius, mm**	**Time, s**	**Radius, mm**	**Time, s**	**Radius, mm**	**Time, s**	**Radius, mm**
0	35	0	35	0	35	0	35	0	35	0	35
1	52	1	52	1	52	1	53	1	52	1	51
2	57	2	55	2	55	2	58	2	55	2	53
3	62	3	60	3	59	3	64	3	59	3	57
4	68	4	64	4	63	4	68	4	64	4	59
5	72	5	68	5	67	5	73	5	68	5	63
10	86	10	82	10	80	10	88	10	82	10	75
15	96	15	92	15	90	15	97	15	92	15	83
20	102	20	97	20	96	20	103	20	97	20	91
25	106	25	102	25	100	25	108	25	101	25	93
30	110	30	106	30	105	30	112	30	105	30	97
35	113	35	109	35	107	35	115	35	108	35	101
40	116	40	112	40	110	40	117	40	111	40	103

Table 35. Output Measured Paraview WN10. (Source: Own Design)